ABSTRACT

CARRIER TRANSPORT ENGINEERING IN WIDE BANDGAP SEMICONDUCTORS FOR PHOTONIC AND MEMORY DEVICE APPLICATIONS

by
Ravi Teja Velpula

Wide bandgap (WBG) semiconductors play a crucial role in the current solid-state lighting technology. The AlGaN compound semiconductor is widely used for ultraviolet (UV) light-emitting diodes (LEDs), however, the efficiency of these LEDs is largely in a single-digit percentage range due to several factors. Until recently, AlInN alloy has been relatively unexplored, though it holds potential for light-emitters operating in the visible and UV regions. In this dissertation, the first axial AlInN core-shell nanowire UV LEDs operating in the UV-A and UV-B regions with an internal quantum efficiency (IQE) of 52% are demonstrated. Moreover, the light extraction efficiency of this UV LED can be further improved by 63% by utilizing appropriate hexagonal photonic crystal structures.

The carrier transport characteristics of the LEDs have been carefully engineered to enhance the carrier distributions and reduce the current leakage, leading to a significantly improved IQE of the LEDs. In this regard, the *p*-type AlGaN electron blocking layer (EBL) has been utilized to suppress electron leakage. Although the EBL can suppress the electron leakage to an extent, it also affects the hole injection due to the generation of positive polarization sheet charges at the hetero interface of EBL and the last quantum barrier (QB). Moreover, the Mg acceptor activation energy of the Al-rich AlGaN EBL layer is elevated, affecting the Mg doping efficiency. To mitigate this problem, in this dissertation, EBL-free UV LED designs are proposed where the epilayers are carefully band-engineered to notably improve the device performance by lowering the electron overflows. The proposed EBL-free strip-in-a-barrier UV LED records the maximum IQE of ∼61.5% which is ∼72%

higher, and IQE droop is $\sim$12.4%, which is $\sim$333% less compared to the conventional AlGaN EBL LED structure at 284.5 nm wavelength. Moreover, it is shown that the EBL-free AlGaN deep UV LED structure with linearly graded polarization-controlled QBs instead of conventional QBs in the active region could drastically reduce the electrostatic field in the quantum well (QW) region due to the decreased lattice mismatch between the QW and the QB. The carrier transport in the EBL-free deep UV LEDs is significantly improved, attributed to the increased radiative recombination, quantum efficiency, and output power compared to the conventional EBL LEDs. Overall, the study of EBL-free UV LEDs offers important insights into designing novel, high-performance deep UV LEDs for practical applications.

Further, it is demonstrated that novel WBG materials could be perfectly employed for emerging non-volatile memory (resistive random access memory, RRAM) applications. The resistive switching (RS) capability has been observed in Ga_2O_3 at low power operation. Importantly, for the first time, the multi-bit storage capability of this types of RRAM devices with a reasonably high R_{off}/R_{on} ratio is experimentally demonstrated. In addition, integrating a thin SiN_x layer in the conventional SiO_2 RRAM device could effectively facilitate the formation of a conducting filament. It is reported that the proposed RRAM device exhibits excellent RS characteristics, such as highly uniform current-voltage characteristics with concentrated SET and RESET voltages, excellent stability, and high R_{off}/R_{on} ($> 10^3$) even at ultra-low current (10 nA) operation. The multi-bit RS behavior has been observed in these RRAM devices, which pave the way for low-power and high-density data storage applications.

CARRIER TRANSPORT ENGINEERING IN WIDE BANDGAP SEMICONDUCTORS FOR PHOTONIC AND MEMORY DEVICE APPLICATIONS

by
Ravi Teja Velpula

A Dissertation
Submitted to the Faculty of
New Jersey Institute of Technology – Newark
in Partial Fulfillment of the Requirements for the Degree of
Doctor of Philosophy in Electrical Engineering

Helen and John C. Hartmann
Department of Electrical and Computer Engineering

December 2022

APPROVAL PAGE

CARRIER TRANSPORT ENGINEERING IN WIDE BANDGAP SEMICONDUCTORS FOR PHOTONIC AND MEMORY DEVICE APPLICATIONS

Ravi Teja Velpula

Dr. Hieu Pham Trung Nguyen, Dissertation Advisor Date
Associate Professor of Electrical and Computer Engineering, NJIT

Dr. Leonid Tsybeskov, Committee Member Date
Distinguished Professor of Electrical and Computer Engineering, NJIT

Dr. Dong-Kyun Ko, Committee Member Date
Associate Professor of Electrical and Computer Engineering, NJIT

Dr. Xuan Liu, Committee Member Date
Associate Professor of Electrical and Computer Engineering, NJIT

Dr. Sagnik Basuray, Committee Member Date
Associate Professor of Chemical and Materials Engineering, NJIT

BIOGRAPHICAL SKETCH

Author: Ravi Teja Velpula

Degree: Doctor of Philosophy

Date: December 2022

Undergraduate and Graduate Education:

- Doctor of Philosophy in Electrical Engineering
  New Jersey Institute of Technology, Newark, NJ, 2022
- Master of Technology in Photonics Science and Engineering,
  Indian Institute of Technology Kanpur, Kanpur, UP, India, 2017
- Bachelor of Technology in Electronics and Communication Engineering,
  Jawaharlal Nehru Technological University, Kakinada, AP, India, 2013

Major: Electrical Engineering

Publications:

Journal Articles:

R. T. Velpula, B. Jain, and H. P. T. Nguyen, "Highly uniform ultralow power resistive switching in SiN_x/SiO_2 RRAM Devices," *in preparation.*

D. T. Tuyet, L. T. Quang, T. B. An, P. C. T. Tung, **R. T. Velpula**, M. B. S. Muthu, H. P. T. Nguyen, V. T. H. Quan, P. J. Deren, and H.- D. Nguyen, "Highly stable white light emission from III-nitride nanowire LEDs utilizing nanostructured alumina doped Mn^{4+} and Mg^{2+}," *under review in ACS Omega.*

S. Shrestha, **R. T. Velpula**, B. P. Pandey, M. B. S. Muthu, N. T. A. Nguyen, and H. P. T. Nguyen, "Characteristics of leakage currents in InGaN/AlGaN nanowire based red micro-light-emitting diodes," *under review in Applied Optics.*

R. T. Velpula*, B. Jain*, and H. P. T. Nguyen, "Multilevel switching in Ga_2O_3 based resistive random access memory devices," *in press, Nanotechnology*, (* equal contribution)

R. T. Velpula, B. Jain, M. Patel, F. M. Shakiba, N. Q. Toan, H.-D. Nguyen, and H. P. T. Nguyen, "High-efficiency InGaN blue LEDs with reduced positive sheet polarization," *Applied Optics*, vol. 61, no. 16, pp 4967-4970, 2022.

R. T. Velpula, B. Jain, T. R. Lenka, and H. P. T. Nguyen, "Polarization engineered p-type electron blocking layer free III-nitride deep-ultraviolet light-emitting diodes for enhanced carrier transport," *Journal of Electronic Materials*, vol. 51, no. 2, pp 838-846, 2022.

S. Das, T. R. Lenka, F. A. Talukdar, **R. T. Velpula**, B. Jain, H. P. T. Nguyen, G. Crupi, "Effects of polarized induced doping and graded composition in an advanced multiple quantum well InGaN/GaN UV-LED for enhanced light technology," *Engineering Research Express*, vol. 4, no. 2, pp 015030, 2022.

S. Das, T. R. Lenka, F. A. Talukdar, S. M. Sadaf, R. T. Velpula, and H. P. T. Nguyen, "Impact of a prestrained graded InGaN/GaN interlayer towards enhanced optical characteristics of a multi-quantum well LED based on Silicon substrate," *Applied Optics*, vol. 61, no. 30, pp 8951-8958, 2022.

R. T. Velpula, M. Patel, B. Jain, A. Marangon, and H. P. T. Nguyen, "Enhanced efficiency of AlInN nanowire ultraviolet light-emitting diodes using photonic crystal structures," *ECS Transactions*vol. 109, no. 7, pp 3-9, 2022. (Invited)

B. Jain, **R. T. Velpula**, M. Patel, and H. P. T. Nguyen, "Controlled carrier mean free path for the enhanced efficiency of III-nitride deep-ultraviolet light-emitting diodes," *Applied Optics*, vol. 60, no. 11, pp 3088-3093, 2021.

B. Jain, **R. T. Velpula**, H. Q. T. Bui, M. Patel, S. M. Sadaf, and H. P. T. Nguyen, "Improved performance of electron blocking layer free AlGaN deep-ultraviolet light-emitting diodes using graded staircase barrier," *Micromachines*, vol. 12, no. 3, pp 334, 2021.

R. T. Velpula, B. Jain, T. R. Lenka, and H. P. T. Nguyen, "Controlled electron leakage in electron blocking layer free InGaN/GaN nanowire light-emitting diodes," *Facta Universitatis-Series: Electronics and Energetics*, vol. 34, no. 3, pp 393-400, 2021.

M. Patel, B. Jain, **R. T. Velpula**, and H. P. T. Nguyen, "Effect of HfO2 passivation layer on light extraction efficiency of AlInN nanowire ultraviolet light-emitting diodes," *ECS Transactions*, vol. 102, no. 3, pp 35-42, 2021.

T. H. Q. Vu, T. T. Doan, B. Jain, **R. T. Velpula**, T. C. T. Pham, H. P. T. Nguyen, and H.-D. Nguyen, "Improving color quality of nanowire white light-emitting diodes with Mn4+ doped fluoride nanosheets," *Micromachines*, vol. 12, no. 8, pp 965-973, 2021.

H. Q. T. Bui, D. T. Tuyet, **R. T. Velpula**, B. Jain, H. P. T. Nguyen, and H.- D. Nguyen, "Enhancing efficiency of AlGaN ultraviolet light-emitting diodes with graded p-AlGaN hole injection layer," *Physica Status Solidi A*, vol. 218, no. 15, pp 2100003(1-8), 2021.

R. T. Velpula, B. Jain, S. Velpula, H.- D. Nguyen, and H. P. T. Nguyen, "High-performance electron-blocking-layer-free deep ultraviolet light-emitting diodes implementing a strip-in-a-barrier structure," *Optics Letters*, vol. 45, no. 18, pp 5125-5128, 2020.

R. T. Velpula, B. Jain, M. R. Philip, H.- D. Nguyen, R. Wang and H. P. T. Nguyen, "Epitaxial growth and characterization of AlInN based core-shell nanowire light-emitting diodes operating in the ultraviolet spectrum," *Scientific Reports*, vol. 10, no. 1, pp 2547-2556, 2020.

R. T. Velpula, B. Jain, T. H. Q. Bui, T. T. Pham, V. T. Le, H.-D. Nguyen, T. R. Lenka, and H. P. T. Nguyen, "Numerical investigation on the device performance of electron blocking layer free AlInN nanowire deep ultraviolet light-emit-ting diodes," *Optical Materials Express*, vol. 10, no. 2, pp 472-483, 2020.

R. T. Velpula*, B. Jain*, H. Q. T. Bui, F. M. Shakiba, J. Jude, M. Tumuna, H.-D. Nguyen, T. R. Lenka, and H. P. T. Nguyen, "Improving carrier transport in AlGaN deep-ultraviolet light-emitting diodes using a strip-in-a-barrier structure," *Applied Optics*, vol. 59, no. 17, pp 5276-5281, 2020.

R. T. Velpula, B. Jain, H. Q. T. Bui, and H. P. T. Nguyen, "Full-color III-Nitride nanowire light-emitting diodes," *Journal of Advanced Engineering and Computation*, vol. 3, no. 4, pp 551-588, 2020.

B. Jain*, **R. T. Velpula***, S. Velpula, H.-D. Nguyen, and H. P. T. Nguyen, "Enhanced hole transport in AlGaN deep ultraviolet light-emitting diodes using a double-sided step graded superlattice electron blocking layer," *Journal of the Optical Society of America B*, vol. 37, no. 9, pp 2564-2569, 2020.(* equal contribution)

B. Jain, **R. T. Velpula**, M. Tumuna, H. Q. T. Bui, J. Jude, T. T. Pham, A. V. Hoang, R. Wang, and H. P. T. Nguyen, "Enhancing the light extraction efficiency of AlInN nanowire ultraviolet light-emitting diodes with photonic crystal structures," *Optics Express*, vol. 28, no. 15, pp 22908-22918, 2020.

B. Jain, **R. T. Velpula**, H. Q. T. Bui, H.- D. Nguyen, T. R. Lenka, T. K. Nguyen, and H. P. T. Nguyen, "High performance electron blocking layer free InGaN/GaN nanowire whitelight- emitting diodes," *Optics Express*, vol. 28, no. 1, pp 665-675, 2020.

D. T. Tuyet, V. T. H. Quan, B. Bondzior, P. J. Deren, **R. T. Velpula**, H. P. T. Nguyen, L. A. Tuyen, N. Q. Hung, and H.- D. Nguyen, "Deep red fluoride dots-innanoparticles for high color quality micro white light-emitting diodes," *Optics Express*, vol. 28, no. 18, pp 26189-26199, 2020.

H. Q. T. Bui, **R. T. Velpula**, B. Jain, and H. P. T. Nguyen, "III-nitride based narrow band far-UVC LEDs for airborne and surface disinfection," *ECS Transactions*, vol. 98, no. 6, pp 83-89, 2020.

H. Q. T. Bui, **R. T. Velpula**, B. Jain, M. R. Philip, H. D. Tong, T. R. Lenka, and Hieu Pham Trung Nguyen, "High performance nanowire ultraviolet light-emitting diodes with potassium hydroxide and ammonium sulfide surface passivation," *Applied Optics*, vol. 59, no. 24, pp 7352-7356, 2020.

R. Singh, T. R. Lenka, **R. T. Velpula**, B. Jain, H. Q. T. Bui, and H. P. T. Nguyen, "Investigation of current collapse and recovery time due to deep level defect traps in β - Ga_2O_3 HEMT," *Journal of Semiconductors*, vol. 41, no. 10, pp 102802-102806, 2020.

R. Singh, **R. T. Velpula**, B. Jain, H. Q. T. Bui, H. P. T. Nguyen, and T. R. Lenka, "A novel β - Ga_2O_3 HEMT with fT of 166 GHz and X-band POUT of 2.91 W/mm," *nternational Journal of Numerical Modelling: Electronic Networks, Devices and Fields*, vol. 34, no. 1, pp e2794(1-11), 2020.

R. Singh, D. K. Panda, T. R. Lenka, **R. T. Velpula**, B. Jain, H. Q. T. Bui, and H. P. T. Nguyen, "The dawn of Ga2O3 HEMTs for high power electronics - a review," *Materials Science in Semiconductor Processing*, vol. 119, pp 105216-105231, 2020.

D. K. Panda, R. Singh, T. R. Lenka, **R. T. Velpula**, B. Jain, H. Q. T. Bui, T. T. Pham, S. M. Sadaf, and H. P. T. Nguyen, "Single and double gate based GaN MOS-HEMTs for design of low noise amplifier: a comparative study," *IET Circuits, Devices and Systems*, vol. 14, no. 7, pp 1018-1025, 2020.

H. Q. T. Bui, **R. T. Velpula**, B. Jain, O. H. Aref, H.- D. Nguyen, T. R. Lenka, and H. P. T. Nguyen, "Full-color InGaN/AlGaN nanowire micro light-emitting diodes grown by molecular beam epitaxy: a promising candidate for next generation micro displays," *Micromachines*, vol. 10, no. 8, pp 492-500, 2019.

A. Sreeprasad, **R. T. Velpula**, and R. Gannavarpu, "Defect detection using windowed Fourier spectrum analysis in diffraction phase microscopy," *Journal of Physics Communications*, vol. 3, no. 2, pp 025006(1-12), 2019.

Conference Presentations:

R. T. Velpula, B. Jain, S. Das, T. R. Lenka, and H. P. T. Nguyen, "Advantages of polarization engineered quantum barriers in III-nitride deep ultraviolet light-emitting diodes: an electron blocking layer free approach," *2022 Springer International Conference on Micro/Nanoelectronics Devices, Circuits, and Systems (MNDCS-2022)*, (Invited talk).

S. Das, T. R. Lenka, F. A. Talukdar, **R. T. Velpula**, and H. P. T. Nguyen, "Carrier transport and radiative recombination rate enhancement in GaN/AlGaN multiple quantum well UV-LED using band engineering for light technology," *2022 Springer International Conference on Micro/Nanoelectronics Devices, Circuits, and Systems (MNDCS-2022)*

S. Das, T. R. Lenka, F. A. Talukdar, **R. T. Velpula**, and H. P. T. Nguyen, and G. Crupi, "Influence of prestrained graded InGaN interlayer on the optical characteristics of InGaN/GaN MQW-based LEDs," *International Conference on Numerical Simulation of Optoelectronic Devices (NUSOD)*, pp 91-92, 2022.

R. T. Velpula, B. Jain, T. R. Lenka, and H. P. T. Nguyen, "InGaN/GaN nanowire white color light-emitting diodes without electron blocking layer," *2021 Springer International Conference on Micro/Nanoelectronics Devices, Circuits, and Systems (MNDCS-2021)*, (Invited talk).

B. Jain, **R. T. Velpula**, and H. P. T. Nguyen, "Phosphor-free III-nitride red micro-light emitting diodes for display applications," *Conference on Lasers and Electro-Optics (CLEO), The Optical Society of America*, 2021.

B. Jain, **R. T. Velpula**, M. Patel, and H. P. T. Nguyen, "High performance electron blocking layer free ultraviolet light-emitting diodes," *SPIE Photonics West, Physics and Simulation of Optoelectronic Devices XXIX*, vol. 11680, pp 132-139, 2021.

H. P. T. Nguyen, B. Jain, **R. T. Velpula**, and M. Patel, "Molecular beam epitaxial growth of high efficiency AlInN nanowire ultraviolet light-emitting diodes," *Proc. SPIE 11800, Low-Dimensional Materials and Devices*, vol. 11800, pp 118000, 2021.

S. Das, T. R. Lenka, F. A. Talukdar, **R. T. Velpula**, B. Jain, H. P. T. Nguyen, and G. Crupi, "Effects of spontaneous polarization on luminous power of GaN/AlGaN multiple quantum well UV-LEDs for light technology," *15th IEEE International Conference on Advanced Technologies, Systems and Services in Telecommunications (TELSIKS)*, pp 335-338, 2021.

S. Das, T. R. Lenka, F. A. Talukdar, **R. T. Velpula**, B. Jain, and H. P. T. Nguyen, "Performance enhancement of AlInGaN quantum Well based UV-LED," *IEEE 18th India Council International Conference (INDICON)*, pp 1-5, 2021

R. T. Velpula, B. Jain, H. Q. T. Bui, and H. P. T. Nguyen, "Ultraviolet light-emitting diodes using aluminium indium nitride nanowire structures," *ECS Meeting Abstracts, PRiME 2020 (ECS, ECSJ, and KECS Joint Meeting).*

B. Jain, **R. T. Velpula**, H. Q. T. Bui, M. Patel, and H. P. T. Nguyen, "Electron blocking layer free full-color InGaN/GaN white light-emitting diodes," *ECS Meeting Abstracts, PRiME 2020 (ECS, ECSJ, and KECS Joint Meeting).*

B. Jain, **R. T. Velpula**, H. Q. T. Bui, M. Tumuna, J. Jude, and H. P. T. Nguyen, "Electron blocking layer free AlGaN deep-ultraviolet light emitting diodes," *Conference on Lasers and Electro-Optics (CLEO)*, pp. AF1l. 3, 2020

H. Q. T. Bui, **R. T. Velpula**, B. Jain, and H. P. T. Nguyen, "Full-color microLEDs for display technologies," *Conference on Lasers and Electro-Optics (CLEO)*, pp. ATh3l. 4, 2020.

R. T. Velpula, B. Jain, H. Q. T. Bui, and H. P. T. Nguyen, "High-efficiency ultraviolet emission from AlInN/GaN nanowires grown by molecular beam epitaxy," *Conference on Lasers and Electro-Optics (CLEO)*, pp. STu3P. 4, 2020

R. Singh, T. R. Lenka, **R. T. Velpula**, H. Q. T. Bui, and H. P. T. Nguyen, "Investigation of E-mode beta-gallium oxide MOSFET for emerging nanoelectronics," *IEEE 14th Nanotechnology Materials and Devices Conference (NMDC)*, pp. 1-5, 2019.

Dedicated to my wife.

ACKNOWLEDGMENT

I am highly grateful to my thesis advisor Dr. Hieu Nguyen, for giving me the opportunity to pursue doctoral research in his lab. Also, I would like to convey my heartfelt thanks to Dr. Hieu Nguyen for his unconditional support of my Ph.D. studies and research, as well as his patience, encouragement, passion, and immense expertise. During my time at NJIT, he has influenced me in many aspects with his optimistic attitude and passionate personality. Not only I learn from him how to do the research, but also I learn from him to how to manage a group, and personal life. Definitely, I will miss conversations with Dr. Hieu at Dunkin Donuts. Dr. Hieu Nguyen has provided me with many great opportunities such as research collaborations (including working on device fabrication, structural/optical/electrical characterizations, device modeling) and summer internship. His persistent support has enabled me to attain my present level of success. As a research scholar, mentor, teacher, and role model, he has set a high standard. I also like to thank Prof. Nguyen's family for their help, providing special treats with homemade food, and spending time together.

Next, I would like to thank my dissertation committee members: Professors, Leonid Tsybeskov, Dong-Kyun Ko, Xuan Liu, and Sagnik Basuray, for providing me valuable suggestions and advice on my Ph.D. research work.

I also acknowledge the Teaching Assistantship funding from the Department of Electrical and Computer Engineering. I am grateful to the National Science Foundation (ECCS-1944312) for supporting my research. I am grateful to Dr. Trupti Rajan Lenka for his close collaboration on several projects and enjoyed working with his team. I sincerely thank Dr. Durga Misra for allowing me to use semiconductor characterization facility.

I am grateful to my colleagues at Nano-Optoelectronic Materials and Devices Lab lab-mates: Dr. Barsha Jain, Moulik Patel, Mano Bala Sankar Muthu, Dr. Victor

Bui, Moustafa yousef, Omar Hamed Aref, Moses Tumuna, Jeffrey Jude, and Dr. Moab Rajan Philip for their valuable discussions and contribution of some of the work in this dissertation.

I also take this opportunity to thank staff administrators in my department, especially Ms. Joan Mahon and Teri Bass.

I am grateful to my managers and mentors at Micron Technology: Andrew Kurtz, Chase Mecham, Sandeep Kumar, Preeti Kumari, Amir Hassani, and Norman, for their support and guidance on my intern projects.

I would like to thank Ms. Clarisa Gonzalez-Lenahan and Dr. Sotirios Ziavras from the Office of Graduate Studies, for the dissertation document review process and for helping me with the degree completion paperwork.

I am grateful to all Maplewood Bible Chapel (MBC) members (specially to James John and Stephen Paul family) in NJ, who treated like their own family members and helped us in many aspects.

Importantly, I would like to express my deepest love to my wife, parents, parents-in-law and siblings. They all kept me going and this dissertation would not have been possible without their constant support. I had a very unique opportunity to share most of my research work, sleepless nights in the cleanroom for device fabrication and publications with my wife, who is the main pillar in my supporting system and we are extremely grateful Dr. Hieu Nguyen for the opportunity.

TABLE OF CONTENTS

TABLE OF CONTENTS
(Continued)

TABLE OF CONTENTS
(Continued)

Chapter **Page**

TABLE OF CONTENTS
(Continued)

LIST OF TABLES

LIST OF FIGURES

LIST OF FIGURES
(Continued)

LIST OF FIGURES
(Continued)

LIST OF FIGURES
(Continued)

LIST OF FIGURES
(Continued)

LIST OF FIGURES
(Continued)

CHAPTER 1

INTRODUCTION

1.1 Wide Bandgap Semiconductors

The crystal structure and energy bandgap are the fundamental properties of any semiconductor. Wide bandgap (WBG) semiconductors are typically those with an energy bandgap (E_g) higher than 2 eV and named after their relative wide energy bandgap in comparison to silicon [2]. WBG semiconductors, such as group III-nitrides, and group III-oxides materials, are gaining popularity due to their remarkable physical and chemical properties, which make them useful in a variety of applications ranging from photonics to electronics [3–5].

In recent years, III-nitride semiconductors including GaN, InN, AlN, and their alloys have gained tremendous attention for their direct and wide bandgap properties. These compound semiconductors have distinct electrical and optical properties, including strong electron mobility, high saturation velocity, a high breakdown electric field, great chemical stability, and good thermal conductivity [6–9]. Three crystallographic structures are possible for III-nitride semiconductor materials: cubic zinc-blende, hexagonal wurtzite, and rocksalt. Comparatively to other structures, the hexagonal wurtzite structure is the most stable crystalline structure for III-nitride semiconductors at ambient temperatures. Comparatively to cubic zinc-blende and rock-salt structures, the hexagonal wurtzite structure is the most stable crystalline structure for III-nitride semiconductors at ambient temperatures. GaN hexagonal wurtzite crystal structured unit cell is shown in Figure 1.1. Also, the formation of rock-salt structures is possible only under high pressure [10, 11].

As shown in Figure 1.2, this material system has the energy bandgap tuning capability from ultraviolet (UV), AlN (6.2 eV) to infrared (IR), InN (0.7 eV) [13].

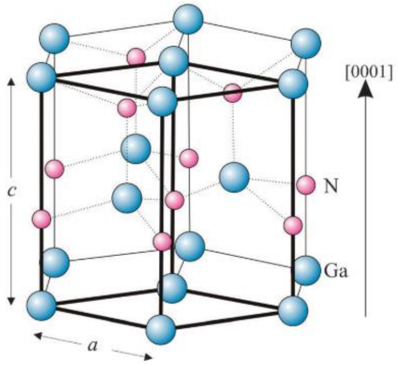

Figure 1.1 III-nitride hexagonal wurtzite crystal structured unit cell. *Source:* [12].

As a result, III-nitride materials are well widely used for photonic devices such as light-emitting diodes (LEDs) [14–16], LASER diodes (LDs) [17, 18], solar cells [19, 20], and photo-detectors [21, 22]. Moreover, GaN exhibits high breakdown field (3.3 MV/cm), wide bandgap (3.4 eV), and high electron saturation velocities (2.5×10^7 cm/s), which are essential for high-power and high-frequency applications [4, 13, 23, 24]. Recently, AlN has been studied for Resistive Random-Access Memory (RRAM) device applications [25, 26] because of its large energy bandgap (6.2 eV), high electrical resistivity ($\sim10^{14}$ Ωcm), dielectric constant is 12.4, material stability [27, 28]. However, conventional III-nitride thin-film heterostructures are grown on lattice-mismatched materials such as sapphire, carbide, or silicon due to the lack of a native substrate. This results in a poor-quality crystal, a high density of dislocations, threading defects, and polarization, all of which significantly limit the performance and applications of the devices.

Among the WBG semiconductors, Ga_2O_3 is currently one of the emerging WBG materials grabbed the attention of worldwide researchers due to its suitable material properties especially for high power electronics and photonics. The β-phase is the stable one, well-explored, has WBG of 4.4–4.9 eV [3–5], making it suitable

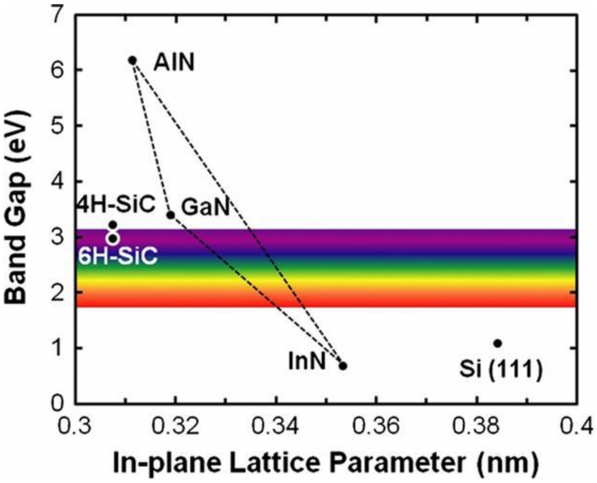

Figure 1.2 The energy bandgap vs. lattice parameter of III-nitride materials. *Source:* [29].

for applications as deep UV regime [30]. The structure of β-Ga_2O_3 has a center of symmetry but no specific features such as polarity, piezoelectricity, ferroelectricity [2]. Existing semiconductor materials such as SiC and GaN are dominating in high power electronics applications. It is known that higher breakdown electric field is critical need for high power electronic devices. Because of larger energy bandgap and greater breakdown electric field (8 MV/cm) of β-Ga_2O_3 appears to be a promising candidate for high-power and high-frequency applications. Although the performance of β-Ga_2O_3 devices seems to be improving, numerous challenges remain, including growing maturity, thermal control, and material reliability. Nonetheless, β-Ga_2O_3 is predicted to supplement more mature WBG semiconductors such as SiC and GaN in power device technologies [117]. Further, β-Ga_2O_3 also allows for a high intrinsic resistance state due to the limited carrier mobility caused by the effective mass of 0.342 $m_\circ$ (where $m_\circ$ is free electron mass) [31]. Importantly, Ga_2O_3 has strong thermal and chemical stability [32], which can help to reduce performance deterioration in different resistance states of RRAM devices.

1.2 Key Challenges in III-nitride Materials/Devices

The primary challenges involved with III-nitride materials and devices can be listed below:

1.2.1 Crystal Defects and Dislocations

Conventional III-nitride heterostructures are grown on lattice-mismatched materials such as sapphire, SiC, or Si due to the lack of a native substrate. This results in a poor crystal quality, a large density of dislocations, threading defects, unwanted foreign atoms, and native defects, all of which significantly limit the device's performance and applications [6, 33]. All of these defects have distinct energy levels than the semiconductor atoms. Such defects are rather common in forming additional one or more energy levels within the semiconductor's forbidden gap, and thus are good sources of non-radiative recombination. The non-radiative recombination that results at these defect energy levels is known as Shockley-Read-Hall (SRH) non-radiative recombination, and it can dramatically reduce device efficiency. In this regard, III-nitride nanowire structures have emerged as an alternative candidate to thin-film structures because of nearly dislocation-free density due to effective lateral stress relaxation [34–36].

1.2.2 Polarization

Because of the large electronegativity and tiny size of N atoms in contrast to metal atoms, the bonds formed between Ga/Al/In and N display polar (high ionicity) properties along with the [0001] orientation in III-nitride WBG semiconductors. As shown in Figure 1.1, each GaN unit cell has a hexagonal base length (a), a hexagonal prism height (c), and an internal parameter (u) as the anion-cation bond length along the (0001) axis in c units. A charge dipole is present in each GaN unit cell as a result of the spatial separation of positive and negative charge (electron cloud) (the nuclei).

An electron cloud and positively charged nuclei's minute movements provide a surface polarization charge as high as $\sim 1.8 \times 10^{13}/\text{cm}^2$ and $\sim 5 \times 10^{13}/\text{cm}^2$ was estimated for GaN and AlN, respectively. Given that semiconductors have a sheet charge density of $\sim 1 \times 10^{15}/\text{cm}^2$, it may be assumed that one in every 100 atoms contributes to the polarization charge. These polarization sheet charges are accompanied by an electric field of ~1-10 MV/cm [37]. In the bulk material, these polar dipoles cancel one another; but, at the surfaces, they create negative/positive sheet charges.

The non-centrosymmetric character of the ions causes spontaneous polarization in Wurtzite hexagonal close-packed crystal structures. On the other hand, in symmetric zinc-blende crystal structures, spontaneous polarization is seldom noticeable. A negative sheet charge forms on the Ga atom terminated surface (Ga-polar), whereas a positive sheet charge forms on the N atom terminated surface (N-polar) at the interface. In addition to the spontaneous polarization, the strained AlGaN/GaN or InGaN/GaN heterointerfaces exhibit piezoelectric polarization that results in a net charge (positive or negative).

Anion to cation displacement results from piezoelectric polarization at heterointerfaces caused by high strain. In III-nitride LEDs and lasers, the piezoelectric polarization field is greater than the spontaneous polarization field, and such a strong field is crucial to the functionality of the device. This piezoelectric polarization becomes more troublesome in III-nitride LEDs because it greatly encourages electron escape from the active area to the *p*-side region. The efficiency droop issue is further exacerbated by this electron leakage. Additionally, the quantum confined stark effect (QCSE), which reduces the overlap potential (spatial separation) of the electron and hole (band bending in the opposite direction) wave functions in the LED active region [38, 39], is brought on by the presence of the polarization field in multi quantum wells (QWs) active region. This QCSE impact lowers the likelihood

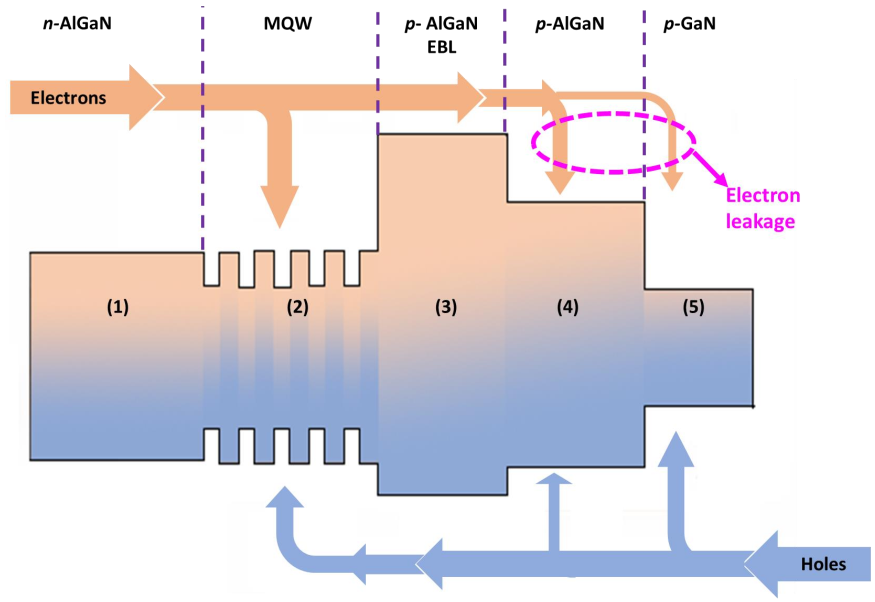

Figure 1.3 Schematic energy-band diagram of a conventional AlGaN UV LED presenting the electron leakage from the active region (polarization fields are not considered in the structure).

of radiative recombination, causes a rise in carrier loss, and worsens the LED's overall performance [39].

1.2.3 Electron Leakage

The electron leakage/overflow from the active region is one of the major reasons behind the efficiency droop in III-nitride light-emitters. Electron leakage refers to the leakage or flow of electrons from the active region without being captured or radiatively/non-radiatively recombined in the active region and it can be seen from Figure 1.3. One of the primary reasons for electron overflow is the higher mobility of electrons than holes. Another critical reason is reducing the energy barrier due to the built-in polarization field [40]. The polarization field causes the band energy to tilt, which results in the separation of electrons and holes. Because of this, carrier recombination also reduces. The overflowed electrons can recombine with holes in the p-GaN region before the holes can reach the active region, resulting in the degradation of radiative recombination in the active region [41]. In this context, a large bandgap material. i.e., AlGaN electron blocking layer (EBL), is often incorporated between the last quantum well and the *p*-GaN region to reduce the electron leakage [42]. However, a high Al content-based EBL may form a high barrier, resulting in the further reduction of hole injection in the LED active region. Also, at relatively high carrier injection, EBL usually cannot completely block the electron overflow in GaN LEDs and as a result, causes the internal quantum efficiency (IQE) droop in the devices. In dot-in-a-wire quantum dots (QDs) structures, it was proposed that the optimum quantum efficiency is limited by electron leakage rather than Auger recombination. By incorporating a *p*-doped large bandgap AlGaN (low Al%) EBL, Nguyen et al. achieved significantly improved efficiency droop [42].

1.2.4 Poor Hole Transport and Injection

Because of the large effective mass and low mobility, hole injection and transportation are very inefficient in III-nitride LED [43]. As a result, injected holes are predominantly localized around the QWs towards the *p*-side, and hole concentration decreases significantly toward the *n*-GaN side. Hence, acceptable photon emission is only given from quantum wells near to the *p*-side. Electrons, on the other hand, have a smaller effective mass and higher electron mobility, therefore electron distribution should be more uniform over the quantum well [43]. The usual electron mobility in AlGaN-based optoelectronic devices is 200 cm^2/V-sec or more, and large electron carrier concentrations are easily achieved due to high ionization efficiency and low ionization energy. Due to the high *p*-type dopant (Mg) ionization energy, hole mobility is only 10 cm^2/V-sec. The Mg activation energy of $\mathrm{Al}_x\mathrm{Ga}_{1-x}\mathrm{N}$ for $0<x<1$ is set to scale linearly [44] from 170 meV to 510 meV which is much higher than Si activation energy for *n*-type layers. Further, hole injection into the multi QW active region is limited due to the generation of positive sheet polarization charges at the interface of last quantum barrier (QB) and EBL [45,46].Because of the non-uniform flow, electrons overflow and Auger recombination occur, which lowers radiative recombination.

1.2.5 Low Light Extraction Efficiency

Light extraction efficiency (LEE) represents the amount of light entering into the free space from LED active region and contributes to the external quantum efficiency (EQE), which is product of IQE and LEE. In the case of III-nitride planar LEDs, the LEE is severely limited by the total internal reflection, due to the refractive index contrast between the semiconductor material and the air and the absorption of shorter wavelength light in the p-GaN contact layer [47]. Furthermore, specially for deep UV LEDs, unique optical polarization properties of high Al composition AlGaN quantum wells results in dominant transverse-magnetic (TM) [E $\parallel$ c-axis] polarized output in the UV regime [48, 49]. As the (TM) (E $\perp$ c-axis) polarized light propagates horizontally, LEE of light emitting from the top surface is severely limited. With a high surface-to-volume ratio, the nanowire structure provides more room for photons to escape, resulting in a reduction in total internal reflection. The LEE can be improved by directing photons toward the nanowire surface. However, EQE in deep UV LEDs remains substantially lower than in visible LEDs. The LEE is boosted by carefully designing the nanowires and its arrangement, considering numerous design factors such as nanowire diameter, spacing, and surface passivation layer thickness [50, 51].

1.3 III-nitride UV LEDs and Current Status

Based on the specific wavelength, UV radiation is often split into three spectral bands: UVA (400 nm–320 nm), UVB (320 nm–280 nm), and UVC (280 nm-100 nm). As the demand for UV light increases, the previously used traditional UV sources such as Mercury, Xenon, Argon, Deuterium, and excimer lamps are found to be unsatisfactory due to energy inefficiency, bulky, fragile, expensive, limited life span, the ability of UV light emission at only a few specific wavelengths, and toxic in nature. Henceforth, it has become greater importance to investigate novel technologies to generate UV light for the corresponding applications [52]. As a solid-state light source, III-nitride based UV LEDs offer several advantages over the traditional UV sources in terms of compactness, nontoxic material composition, low power consumption, quick response time, tunable emission across the entire UV-region, and long lifetime.

The noticeable factors that drive the growth of the UV LED market include the utilization of deep UV LEDs (207 nm to 222 nm) for surface disinfection applications, including killing the deadly SARS-COV-2 virus and many others. Additionally, high-power UVC LEDs are suitable for water disinfection applications. Besides being used to disrupt the DNA or RNA molecules of microorganisms in disinfection applications, UV light can also be employed to trigger chemical reactions, such as polymerization processes during UV curing. Previously, low- and medium-pressure mercury lamps have been utilized for most of these UV curing applications. However, due to the above-mentioned problems in the lamps, III-nitride based UV LEDs are being employed for a wide range of UV curing applications, such as coatings, inks, adhesives, composites, and stereolithography. UV light can also be employed to solicit photochemical reactions in living organisms. Phototherapy is another application of UV LEDs in which UVA light interacts with the living cells of human skin tissue. In this application, UV radiation is used to treat several skin diseases, including psoriasis, vitiligo, and cutaneous T-cell lymphoma. 1.4(a) summarizes several essential applications of UV LEDs.

The current deep UV LEDs still exhibit poor external quantum efficiency (EQE) and lower output power due to lack of bulk substrate, high dislocation density, high resistive *p*-AlGaN due to inefficient *p*-type doping with high Al composition, Electron leakage from the active region, limited LEE due to dominant TM polarization fields

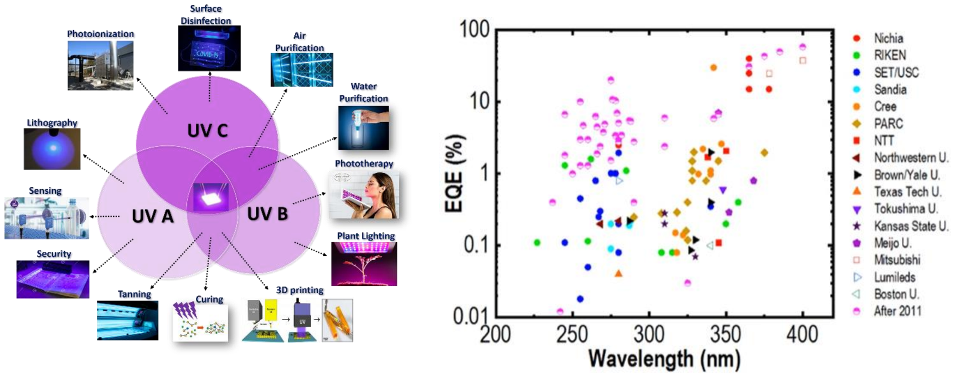

Figure 1.4 (a) Applications of LEDs in UV wavelength spectrum, and (b) Current state of UV LEDs.

[53]. From Figure 1.4(b), it is seen that the EQE of UV LEDs below 300 nm emission wavelength drops drastically [52]. To improve the EQE and optical power of deep UV LEDs, it is necessary to improve the material/epitaxial growth quality and engineer the epitaxial layers. In this context, the motivation of this dissertation is to improve the performance of these UV LEDs by overcoming the challenges mentioned above with exploration other potential III-nitride materials and band engineering with novel device designs so that can have utilized them in practical applications directly.

1.4 Organization of Dissertation

This dissertation presents the demonstration of the first axial AlInN core-shell nanowire UV LED both numerically and experimentally. A large part of the research has been focused on improving the performance of wide bandgap material-based LEDs in the visible and UV regions by band engineering of various epilayers and conducting a comprehensive study of optical and electrical characteristics. Additionally, a thorough investigation of wide bandgap material-based RRAM is conducted to understand the switching capability of these materials.

Chapter 1 provides an overview of wide bandgap semiconductor materials where the need of III-nitride LEDs along with the challenges in the III-nitride materials and devices. Additionally, the current status of the UV LEDs is presented. A theoretical investigation of QW-based AlInN nanowire UV LEDs is provided in Chapter 2 and compared the results with AlGaN UV LEDs for demonstrating the improvement in the device performance of AlInN nanowire UV LEDs. In Chapter 3, the growth mechanism of AlInN core-shell nanowires is discussed along with the procedure for the fabrication of these nanowire UV LEDs operating in UV-A and UV-B regions. Further, various structural, electrical, and optical characteristics of the grown and fabricated nanowire structures are presented. Additionally, an improved LEE for these LEDs is demonstrated using different photonic crystal structures.

In Chapters 4, 5, and 6, various numerical studies are presented in which one of the primary reasons for efficiency droop in deep-UV LEDs i.e., electron leakage, is addressed by band-engineering several epilayers of the LED structures and introducing several EBL-free structures. In Chapter 4, the electron leakage problem is addressed by introducing an optimized thin undoped AlGaN strip layer in the middle of last QB thereby conduction band barrier height is increased, and electron leakage is effectively reduced. As a result, internal quantum efficiency and output power are significantly improved. In Chapter 5, a high-performance EBL-free AlGaN deep UV LEDs is demonstrated using a strip-in-a-barrier structure at 284.5 nm wavelength emission. In the proposed structure, the EBL was successfully eliminated by integrating the engineered thin intrinsic AlGaN strip into the middle of QBs without affecting the carrier injection and transportation. In Chapter 6, the electron leakage and hole injection problems are addressed by controlling the formation of polarization charges with the integration of graded QBs instead of regular QBs in AlGaN deep UV LED without the requirement of any *p*-AlGaN EBL. The elimination of the growing p-heavily doped high Al composition AlGaN layers such as EBLs for deep

UV LEDs, which reduces the device resistance, is an additional key advantage of EBL-free structures from an epitaxial growth standpoint.

In Chapter 7, a study on a novel visible LED structure with an AlGaN last QB, which is lattice-matched to the EBL is presented instead of the conventional GaN last QB. Due to the lattice match at the last QB/EBL interface, the proposed LED stops positive sheet charges from being formed there and improves the device performance.

In Chapter 8, a brief introduction including requirements and the working principle of the RRAM device is presented. In Chapters 9 and 10, the design, fabrication, and characterization of various wide band gap material-based RRAM devices are presented. The multi-bit storage capability of these RRAM devices with a reasonably high R_{off}/R_{on} ratio is experimentally demonstrated at a lower/ultralow opeating currents. These devices have potential applications for low-power and high-density data storage applications.

Finally, Chapter 11 presents the summary, future work, and outlook of this dissertation.

CHAPTER 2

THEORETICAL INVESTIGATION OF ALINN NANOWIRE ULTRAVIOLET LIGHT-EMITTING DIODES

This chapter presents the theoretical investigation of relatively unexplored and novel AlInN material system based nanowire ultraviolet (UV) light-emitting diodes (LEDs).

2.1 UV LED Applications

As a solid-state light source, UV LEDs offer several advantages over traditional UV sources in terms of compactness, nontoxic material composition, low power consumption, tunable emission across the UV region, and long lifetime. Current UV-C LEDs with the output power level in the range of 100-mWs are suitable for water disinfection applications [54, 55]. Besides being used to destroy chemical bonds, UV light can be employed to trigger chemical reactions, such as polymerization processes during UV curing [56]. These processes take place at lower photon energies, typically in the UV-A and UV-B spectral bands. UV light can also be employed to solicit photo chemical reactions in living organisms [57]. Illumination of plants with UV-B light provides a new way to naturally enhance the concentration of secondary plant metabolites, creating healthier and more flavorful fruits and vegetables. Phototherapy is another application of UV light sources in which UV light interacts with the living cells of human skin tissue [58]. This application uses UV radiation to treat several skin diseases, including psoriasis, vitiligo, and cutaneous T-cell lymphoma. UV light has many other potential applications, including medical diagnostics, disinfection of various surfaces, gas sensing, remote detection of biological and chemical compounds, cancer detection, and many more [59–61]. Previously, for most of these applications, low- and medium-pressure mercury lamps have been utilized, however, the mercury lamps are found to be unsatisfactory as they are toxic, bulky and fragile, expensive,

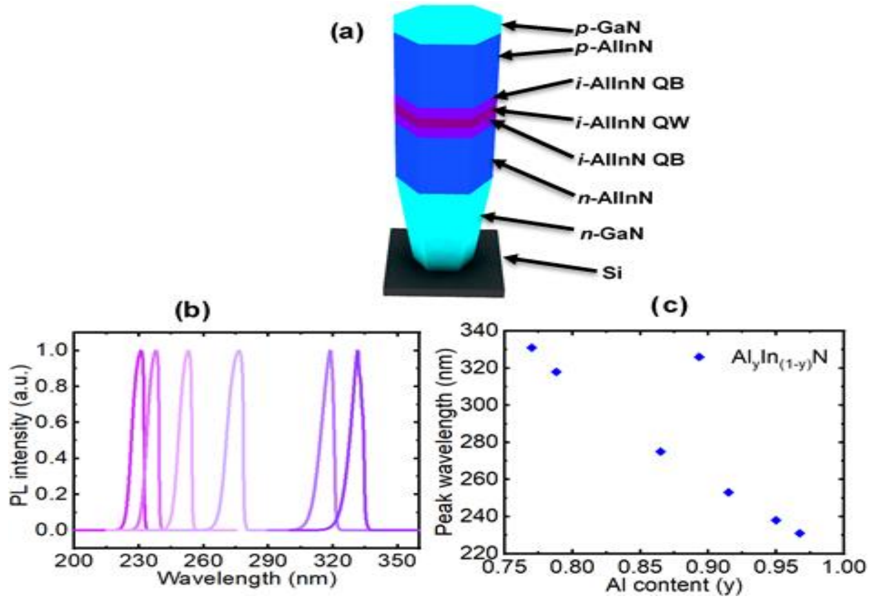

Figure 2.1 (a) Schematic diagram of the AlInN UV LED. (b) Multiple peak emissions varied from 230 nm to 331 nm wavelengths. (c) Emission peak wavelength vs Al content in AlInN active region.

have a short life span, and emit only at a few specific wavelengths. Due to these problems in the lamps, group III-nitride based UV LEDs are being employed for a wide range of applications. Currently, the main customers of UV Light Emitting Diodes are users of UV light in the wavelength range from 280 nm to 400 nm, accounting for more than 90% of the total UV light source market [62].

2.2 Challenges in Current UV LEDs

The performance characteristics of UV LEDs strongly depend on their emission wavelength. Usually, near-UV range (400-365 nm) photonic devices utilize InGaN-based materials which take advantage of the same device technologies as the blue LEDs, hence the performance level of near-UV emitters is close to those of blue LEDs with EQEs ranging from 46-76% [53]. However, the current UV emitters below 365 nm mainly use AlGaN-based UV LEDs. Nevertheless, the performance of thin-film AlGaN-based deep UV LEDs remains very poor with efficiencies largely in the single-digit percentage range, which has been affected by several factors that may include the high density of dislocations, electron leakage, inefficient epitaxial growth and the poor *p*-type doping, resulting in low output power [52, 53, 63, 64]. Another important challenge is the device's light extraction efficiency (LEE) in 290 – 355 nm wavelength region. In this wavelength region as the Al-composition is high and due to the geometry of the nanowires, the polarization of UV light changes from transverse electric (TE) to transverse magnetic (TM) [E $\parallel$ c-axis]. As the TM polarized light propagates horizontally, it reduces the LEE of the related UV LEDs from the top surface [65–67]. Because of these limitations, AlGaN deep UV LEDs have been suffering from EQE and very low output optical power.

Importantly, it is also observed that the EQE is dramatically decreased when devices are operating at sub-250 nm wavelength [68–70]. For instance, the EQE of the planar/nanowire AlGaN LEDs operating at 326 nm, 287 nm, 242 nm is recorded as 2.65% [71], 2.8% [72], and 0.012% [70] respectively. Also, the reported output optical power of the 240 nm emission wavelength UV LED is only around 100 nW [73], which is practically inadequate to utilize in real-world applications. Another factor, the band tilting, which results in the spatial separation of electrons and holes (quantum confined stark effect, or QCSE) can deteriorate the carrier radiative recombination due to locally generated piezoelectric fields in the multiple quantum wells (QWs) of AlGaN UV LEDs. As a result, the LEDs' internal quantum efficiency (IQE) may be severely limited [74, 75]. The IQE is improved to an extent by using nanowire [76, 77] and nanopillar [78] AlGaN LED structures, but QCSE is not suppressed completely. In addition, piezoelectric polarization, high mobility of the electrons, and low hole mobility in the LEDs lead to electron leakage into the *p*-type region which enhances the droop in IQE [79]. However, electron has been mitigated with the integration of an electron blocking layer (EBL) [63, 80–82]. On the other hand, if it is not well-designed, the EBL causes poor hole injection into the active region [83, 84]. The recorded maximum IQE of AlN nanowire deep UV LEDs at 210 nm is around 80% [85]

but LEDs are suffering with severe efficiency droop. Another significant challenge in deep UV LEDs is the ineffective p-doping in high Al content AlGaN or AlInN layers due to the high activation energy of Mg acceptors. The activation energy of Mg acceptors in InN, GaN, and AlN are 60 meV [86], 170 meV [87], 510 meV [44, 87], respectively.

2.3 Advantages of AlInN Light-Emitters

It is vital to identify and develop possible alternative UV materials in order to make additional progress in the development of deep UV emitters. Until recently, the idea of using additional group III-nitride UV materials for light emitters, such as AlInN, was relatively unexplored, though it has great potential for application in UV and visible LEDs. For example, if AlInN with a In composition of ∼17–18% is grown on GaN, lattice matching can be achieved [88,89] and the large refractive index difference with GaN makes these a highly promising candidate for UV light emitters. Recent studies have shown that AlInN offers a large optical gain for deep-UV LEDs [90]. In m-plan GaN/AlInN core-shell nanowire UV emitters, defect-free and QCSEs have been achieved [91]. Using the $k{\cdot}p$ perturbation theory, AlInN compounds are reported to be grown on both GaN and AlN templates, whereas AlGaN is detrimental to growth on GaN templates [18]. Compared to AlGaN, AlInN offers a larger range of alloy compositions that are optimum for UV emission, particularly for deep-UV emission [92]. AlInN offers several advantages and is of great interest for replacing AlGaN or InGaN in several photonic and electronic devices. For example, lattice-matched GaN/AlInN superlattices have been utilized for intersubband transitions [93], high-reflectance distributed Bragg reflectors [94], high-quality microcavities for vertical-cavity surface-emitting laser structures [95], and high-performance, high-electron-mobility transistors [96].

Table 2.1 Parameters of 238 nm Wavelength AlInN and AlGaN Nanowire LEDs

Layer	**Thickness (nm)**	**Al content in AlInN LED**	**Al content in AlGaN LED**
n-GaN	200	-	-
n-Al$_x$In$_{1-x}$N	100	0.975	0.91
i-Al$_x$In$_{1-x}$N	3	0.975	0.91
i-Al$_y$In$_{1-y}$N	3	0.95	0.84
i-Al$_x$In$_{1-x}$N	3	0.975	0.91
p-Al$_x$In$_{1-x}$N	100	0.975	0.91
p-GaN	10	-	-

However, to date, no studies are available on AlInN nanowire LEDs emitting at sub-250 nm wavelength. In this context, a novel EBL-free AlInN nanowire structure with droop-free IQE for the deep UV LEDs operating at sub-250 nm wavelengths have been explored and thier performance is thoroughly evaluated theoretically. The device structure consists of a 200 nm thick n-GaN nanowire template, a 100 nm thick n-Al$_x$In$_{1-x}$N, i-Al$_x$In$_{1-x}$N/ i-Al$_y$In$_{1-y}$N/ i-Al$_x$In$_{1-x}$N (3 nm quantum barrier (QB)/ 3 nm QW/ 3 nm QB), a 100 nm thick p-Al$_x$In$_{1-x}$N and a 10 nm thick p-GaN. The values of x and y are presented in the Table 2.1 and the diameter of nanowire is considered as 100 nm.

2.4 Device Model and Parameters

In this work, each nanowire was considered as one LED. All the LEDs are modeled and the performance is evaluated in this dissertation using the Crosslight APSYS toool. The electrostatic potential (ϕ) is computed using the Poisson's equation (Equation 2.1) which is the fundamental equation used to describe semiconductor device behavior.

$$\nabla \cdot (\varepsilon \nabla \phi) = -q \left(p - n + N_D^+ - N_A^- + \sigma_p - \sigma_n\right) \tag{2.1}$$

where q is the electronic charge, ε is the permittivity of the semiconductor, n and p are the electron and hole densities, N_A^- and N_D^+ are the ionized acceptor and donor concentrations respectively. σ_p and σ_n are the fixed charge from traps.

The carrier distributions including carrier (electron and hole) densities are estimated by solving the current continuity equations (Equations 2.2 and 2.3)

$$\nabla \cdot J_n = q\Big(\frac{\partial n}{\partial t} - \frac{\partial N_D^+}{\partial t} + \frac{\partial \sigma_n}{\partial \mathrm{t}} + R\Big) \tag{2.2}$$

$$\nabla \cdot J_p = q\Big(\frac{\partial N_A^-}{\partial t} - \frac{\partial p}{\partial t} - \frac{\partial \sigma_p}{\partial t} - R\Big) \tag{2.3}$$

where R is the electron-hole recombination (both radiative and non-radiative) rate, J_n and J_p are the electron and hole current density, respectively.

The position and momentum in space that are associated with the wavefunctions in multiple QW active region are calculated using the Schrodinger Equation solver. Further, the band structures are calculated using 6×6 k.p model [97]. The bandgap energies of InN, GaN, and AlN are input into the model as 0.7 eV, 3.4 eV, and 6.2 eV, respectively [13]. The bowing parameters of AlInN and AlGaN are taken as 3.4 eV and 0.7 eV [13]. Importantly, the built-in polarization created due to both the spontaneous and piezoelectric polarization is considered and enabled it as 10% of the theoretical value [42, 98]. The background loss is assumed to be as 2000 m^{-1}. The band offset ratio for all simulations considered as 50/50 [41]. Further, non-radiative recombination mechanisms such as the Shockley-Read-Hall (SRH) recombination lifetime, and the Auger recombination coefficient are set to be 5 ns, and $1 \times 10^{-34}\ \mathrm{cm}^6/\mathrm{s}$, respectively [98]. All simulations are performed at 300 K temperature.

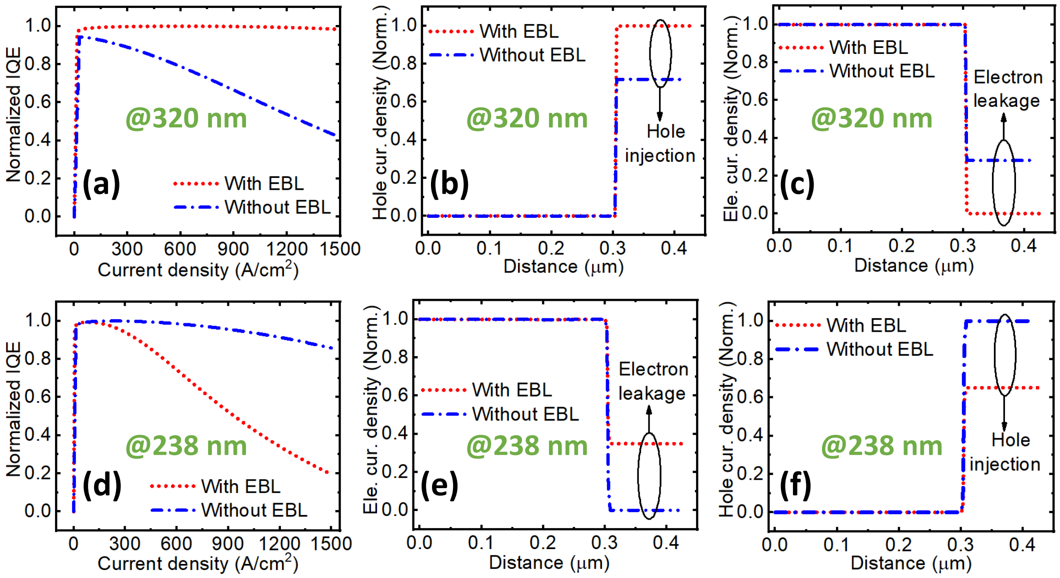

Figure 2.2 Simulated, normalized (a, d) Internal quantum efficiency (IQE), (b, e) Electron current density, (c, f) Hole current density of with/without EBL single QW AlGaN nanowire UV LEDs at 320 nm and 238 nm emission wavelength.

2.5 Results and Discussion

2.5.1 Role of EBL in AlGaN UV LEDs with 320 nm and 238 nm Emission Wavelengths

Figure 2.1(a) depicts the schematic diagram of the proposed AlInN nanowire LED structure. The simulated emission spectra of AlInN nanowire UV LEDs at room temperature is shown in Figure 2.1(b). It is evident that these devices can emit light in the UV A, B, and C regions. Figure 2.1(c) presents the emitted peak wavelength vs Al content (y) in the QW, which is consistent with the theoretical calculations. Further, the performance of both AlInN and AlGaN based nanowire deep UV LEDs are investigated and compared their simulated results. As part of this investigation, it is vital to understand the role of EBL integration in deep UV LEDs. In this regard, two types of deep UV LEDs that include EBL and EBL-free single QW AlGaN nanowire LED structures were considered and the performance has been analyzed. In these simulations, 10 nm thick *p*-doped $Al_{0.57}Ga_{0.43}N$ and $Al_{0.98}Ga_{0.02}N$ layers were considered as EBLs in the 320 nm and 238 nm LEDs.

The normalized IQE of the AlGaN UV LEDs with 320 nm emission wavelength is shown in Figure 2.2(a). It is important to note that the integration of the EBL improves the IQE which enhances the performance of this LED. In this context, the integration of the optimized EBL can mitigate the electron overflow from the active region as illustrated in Figure 2.2(b). The presence of EBL reduces hole consumption in the *p*-doping region due to electron blocking from the active region, which enhances hole injection, as presented in Figure 2.2(c). Figure 2.2(d) shows the normalized IQE of the 238 nm wavelength LEDs and at this wavelength, both LEDs which are with and without EBL have a significant amount of droop in IQE. Moreover, the integration of the EBL worsens the IQE compared to the other case, which deteriorates the performance of the LED. In the deep UV wavelengths, utilization of the EBL is responsible for poor hole injection into the active region and is shown in Figure 2.2(f). As a result, the electron overflow increases from the active region and it can be understood from Figure 2.2(e), which is similar to recent reported studies [79]. Hence, EBL-free LEDs are desirable for the development of high efficiency deep UV LEDs. In this regard, we demonstrated that AlInN nanowire structures offer a perfect approach to overcome such a problem. More details on role of EBL in UV LEDs will be discussed in Chapter 4.

2.5.2 EBL-free AlInN vs. AlGaN LEDs at 238 nm Emission Wavelength

Next, the EBL-free AlInN and AlGaN nanowire deep UV LEDs were modeled to emit light at 238 nm emission wavelength. AlGaN LEDs with 1 QW, 3QWs, and 5QWs in their active regions, as well as AlInN LEDs with 1 QW, were included for this analysis, as shown in Figure 2.3. The normalized IQE of those LEDs is shown in Figure 2.3(a). The performance of AlGaN nanowire LEDs improves with the number of QWs in the active area, but the devices still exhibit IQE droop. The IQE droop increases with the injected current in the AlGaN nanowire deep UV LEDs, as seen in Figure 2.3(a).

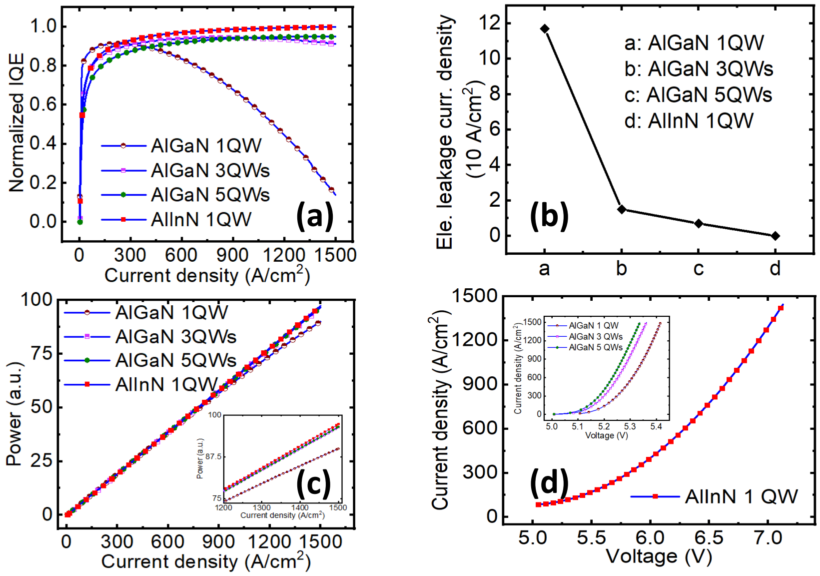

Figure 2.3 Simulated (a) Normalized IQE, (b) Electron leakage current density, (c) L-I characteristics, (d) I-V characteristics of AlGaN and AlInN LEDs at 238 nm emission wavelength.

However, AlInN nanowire LEDs with 1 QW exhibit negligible efficiency droop due to improved device performance, but AlGaN 1 QW nanowire LEDs exhibit considerable IQE droop. The electron leakage from the active region is the primary cause of IQE droop, and the electron leakage current density decreases as the number of QWs in the active region of AlGaN nanowire LEDs increases. However, considerable electron leakage is found even in AlGaN nanowire LEDs with 3 and 5 QWs.

In contrast, electron leakage from the active region is essentially negligible in AlInN nanowire LEDs with 1 QW, as illustrated in Figure 2.3(b). The droop-free IQE of AlInN LEDs is responsible for the high radiative recombination, which results in higher output optical power as compared to other devices, as shown in Figure 2.3(c). The current-voltage (I-V) characteristics of AlInN LEDs are presented in Figure 2.3(d), and the I-V characteristics of AlGaN LEDs are shown in the inset figure. The AlInN UV LED has a greater turn-on voltage than other AlGaN-based UV LEDs because of the large bandgap energy of the QB, which allows for significant band offset between the QW and QB in the AlInN UV LED. Furthermore, the sharp interface

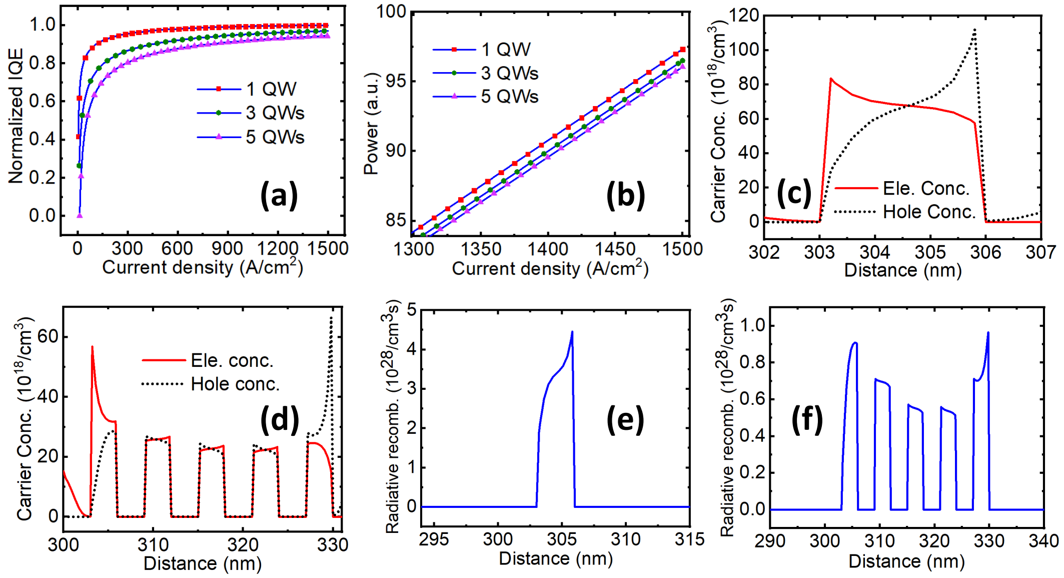

Figure 2.4 Simulated (a) Normalized IQE, (b) L-I characteristics for AlInN LEDs with 1 QW, 3 QWs and 5 QWs. Carrier concentration of AlInN (c) SQW LED. (d) 5 QWs LED. Radiative recombination of AlInN (e) SQW LED. (f) 5 QWs LED at 238 nm emission wavelength.

between the *n*-GaN template and the *n*-AlInN segment can greatly contribute to the increased device resistance and high turn-on voltage of the AlInN UV LED on GaN template.

2.5.3 AlInN Nanowire UV LED with 1 QW vs. 3 QWs, 5 QWs

The performance of AlInN nanowire deep UV LEDs with 1 QW, 3 QWs and 5 QWs in the active region was evaluated at 238 nm emission wavelength. The normalized IQE of the AlInN nanowire LEDs is shown in Figure 2.4(a). Because of the inhomogeneity of carrier distribution in the multi QW active region, 1 QW LED devices exhibit higher IQE than multi QW LED devices [99]. Furthermore, it has a greater output power than multi QW LEDs, as shown in Figure 2.4(b). The carrier concentrations of the 1 QW and 5 QWs AlInN nanowire LEDs are shown in Figures 2.4(c) and (d). The non-uniform carrier dispersion is depicted in Figure 2.4(d). The radiation recombination phenomena of 1 QW and 5 QWs AlInN nanowire LEDs are presented

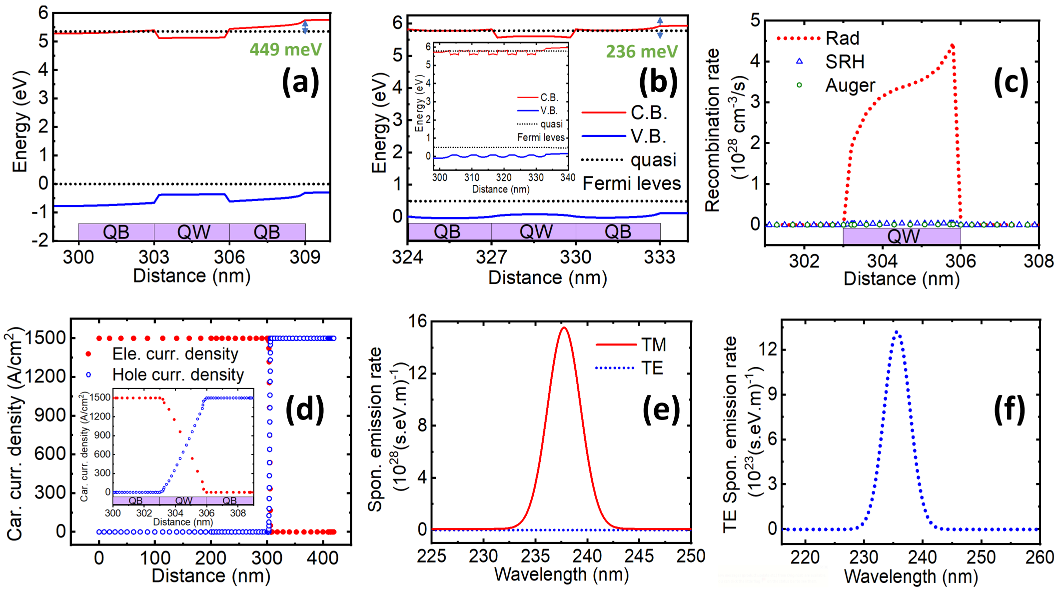

Figure 2.5 Simulated (a) E-B diagram of active region of AlInN 1 QW LED. (b) E-B diagram of the last QW in active region of 5 QWs AlGaN LED (5 QWs are shown in inset figure.) (c) Recombination rate (d) Carrier current density. (e) Spontaneous emission rate (TE/TM). (f) TE spontaneous emission rate of AlInN 1 QW LED at 238 nm emission wavelength.

in Figure 2.4(e) and (f). In the case of multi QW LEDs, the radiative recombination rates become quite non-uniform, with dominating radiative recombination reported in the QW near the *p*-region [100, 101]. This is caused by insufficient carrier transit from one QW to another. 1 QW LED has an estimated total radiative recombination rate of $9.25 \times 10^{28}/\text{cm}^3\text{s}$, which is greater than 5 QWs LED. 5 QWs LEDs have a total radiative recombination of $9.18 \times 10^{28}/\text{cm}^3\text{s}$.

2.5.4 1 QW AlInN Nanowire UV LED

The energy band (E-B) diagram is explored to better understand the process of improvement in 1 QW AlInN nanowire LED at 238 nm emission wavelength. The E-B diagram of the active region of 1 QW AlInN nanowire LED is shown in Figure 2.5(a). The last QW in the active region of a 5 QWs AlGaN LED is depicted in Figure 2.5(b), and the entire active region is shown in the inset image. It is well established that the polarization effect causes an energy band bending at the interface of the last QB and the *p*-type area, which may increase electron leakage from the active zone into the *p*-type region. The effective potential height for electrons in the CB for AlInN LED and AlGaN LED is 449 meV and 236 meV, respectively, as seen in Figure 2.5(a) and (b). As a result, AlGaN LED has fewer electrons in the QW and notable electron leakage into the *p*-type region, where it consumes holes in the *p*-type region. Therefore, AlGaN LEDs have reduced radiative recombination due to the decreased carrier density in the active area. AlInN LED, on the other hand, has a high effective potential height at the interface of the QB and the *p*-type region, which reduces electron leakage and improves carrier recombination in the active region.

Figure 2.5(c) depicts the carrier recombination of AlInN LEDs. It is discovered that radiative recombination is the dominant process, with a 2-order more than SRH and Auger recombination. AlInN LEDs exhibit extremely minimal carrier current density outside of the active region due to their excellent E-B structure and dominating radiative recombination, as seen in Figure 2.5(d). As a result, the proposed structure has a self EBL, with no electron leakage into the *p*-type region. Here, most electrons are getting blocked in the active region without using the EBL, which enhances the hole injection efficiency in the active region [83]. Furthermore, AlInN LEDs exhibit practically minimal hole current density prior to the QW, indicating that the majority of the injected carriers are radiatively recombining. As a result, AlInN LEDs have a high IQE while exhibiting no droop.

Finally, the polarization properties of the emission from AlInN UV nanowire LEDs at room temperature were also analyzed. TM and TE polarized emissions are defined as the electric fields parallel (E$\|$c) and perpendicular (E$\perp$C) to c-axis, respectively. θ is the angle between the c-axis and light detection direction. At any direction, the emitted light is not sole TE and TM polarized components and can be written as [49, 102]

$$\perp \text{ component} = \text{TE spontaneous emission rate}$$

$$\| \text{ component} = \Big[\text{TE spontaneous emission rate} \times (\cos^2\theta)\Big] + \Big[\text{TM spontaneous emission rate} \times (\sin^2\theta)\Big]$$

In this work, considered $\theta = 90$ °, i.e., $\perp$ component (E$\perp$C) is TE spontaneous emission rate and $\|$ component (E$\|$c) is TM spontaneous emission rate. The computation was carried out with an injection current of 1500 A/cm^2. UV light emission is largely TM polarized, as seen in Figures 2.5(e) and (f), which is approximately 5 orders greater than TE polarized emission. The similar trend has recently been experimentally reported for AlInN nanowire UV LEDs with a peak wavelength of 295nm and will be discussed in Chapter 3.

2.6 Conclusion

In conclusion, the role of EBL in 320 nm and 238 nm emission wavelength LEDs has been investigated. Importantly, this chapter reported the successful implementation of design and simulation of EBL-free AlInN nanowire LEDs operating in the deep UV region. It is found that the AlInN deep UV LEDs with 1 QW have better performance in terms of IQE and output optical power compared to AlInN multi QW and AlGaN based deep UV LEDs. Also, the electron and hole overflows were not observed with these 1 QW AlInN deep UV emitters and exhibited strong TM polarized emission. Furthermore, the reported 1 QW AlInN device structure is relatively easy to epitaxially grow compared to multi QW structures thereby greatly reduce the dislocation density and homogeneity of In distribution in the AlInN epilayers.

CHAPTER 3

EPITAXIAL GROWTH AND CHARACTERIZATION OF HIGH-PERFORMANCE ALINN NANOWIRE ULTRAVIOLET LIGHT-EMITTING DIODES

This chapter introduces the epitaxial growth using molecular beam epitaxy (MBE) of high-quality and performance AlInN nanowire structures by overcoming the challenges involved and utilizing them in efficient ultraviolet (UV) light-emitting diodes (LEDs). Further, it reports the first AlInN axial nanowire UV LEDs with a relatively high internal quantum efficiency (IQE) of ∼52% and light-extraction efficiency (LEE) of ∼63% at room temperature.

3.1 Challenges of AlInN Epitaxial Growth

Despite many benefits as discussed in Chapter 2, research on AlInN semiconductors is severely constrained because of the immature epitaxial growth of high-quality AlInN. Group-III nitrides grown by MBE under metal-rich circumstances often have smooth surface morphologies at low growth temperatures. However, nitrogen-rich growth produces rough surfaces at low temperatures [103]. Composition inhomogeneity, which is frequently seen in the AlInN layer, is the primary problem with growing AlInN by MBE [104, 105]. Due to the extremely large differences between the ideal growth temperatures for InN (∼450 °C) and AlN (∼800 °C), epitaxial growth of AlInN has been challenging [106]. Furthermore, inefficient *p*-type doping in AlInN has a significant impact on the electrical characteristics of the associated devices. Low crystalline quality and poor device performance are the results of such issues. The ability to make high-quality AlInN nanowires with no dislocations gives an alternate method for creating new varieties of high-performance UV light emitters. Numerous real-world uses can directly make use of these UV emitters.

According to Speck et al. [107,108], MBE growth under nitrogen-rich environments presents an efficient method of eliminating the composition inhomogeneity in the AlInN. Homogenous AlInN layers with high In contents can be achieved by reducing the Al flux and promoting AlInN development in a N-rich environment [107,108]. The best choice, which provides uniform AlInN structures almost devoid of dislocations at high In concentrations, appears to be nitrogen-rich generated nanowires. Although nanowire structures have various benefits, to the best of our knowledge, axial nanowire-based AlInN semiconductors generated by MBE have not been explored. One of the notable characteristics of nanowire architectures is greatly improved light output power because of significantly reduced dislocations and polarization fields [109, 110]. High-performance group III-nitride nanowire LEDs have been successfully achieved on Si substrates [42, 110, 111]. Furthermore, the lowered formation energy of the substitutional doping on the near-surface region might improve the surface doping and electrical conductivity of nanowire LEDs [112].

3.2 Demonstration of AlInN Nanowire UV LED

In this study, an in-depth investigation of the epitaxial growth of $\mathrm{Al}_x\mathrm{In}_{1-x}\mathrm{N}$/GaN nanowires on Si (111) substrate using plasma-assisted MBE along with the structural and optical characteristics is conducted. Additionally, the first axial AlInN core-shell nanowire UV LED heterostructures are demonstrated that operate in the UV-A and UV-B bands. The development of the AlInN epilayer results in the spontaneous formation of an AlInN shell, which dramatically reduces non-radiative recombination on the nanowire surfaces. By adjusting the aluminum content in the AlInN active area, the peak wavelength can be varied from 290 to 355 nm. With an emission wavelength of 295 nm, the AlInN UV nanowires have a comparatively high IQE of about 52%. Moreover, the UV LED device exhibits strong UV light emission with highly stable peak emission at 295 nm. The polarized optical properties of

AlInN nanowire LEDs were also studied. It is demonstrated that the UV light emitted by AlInN nanowire LEDs is mainly transverse magnetic (TM) polarized and is about four times more intense than transverse electric (TE) light. For practical applications, it is required to extract the TM-polarized photons from the top surface. However, to the best of our knowledge, there has been relatively less research on the polarization-dependent LEE for AlInN-based nanowire UV LEDs, despite the fact that this research is crucial.

Recent research has demonstrated that the luminescence emission intensity and stability can be significantly increased by using nanowire photonic crystals for GaN-based nanowires and by controlling the nanowire radius, spacing between the nanowires, and morphology of nanowires through selective area epitaxy [113–115]. Keeping this in mind, a simulation study on the light extraction properties of AlInN nanowire LEDs for different photonic crystal structure arrangements such as hexagon and square lattice of nanowires is conducted, and the results are compared with the random arrangement. Though the light is TM polarized, the results demonstrate that the primary light emission direction is from the top surface of the nanowires. By controlling the nanowire radius and spacing between the nanowires, photonic crystal designs can enhance the LEE significantly more than random configurations. The principal cause of the reduced efficiency in the case of random nanowire architecture is related to the multipath light scattering between neighboring nanowires, which may localize the light inside the nanowires, or increase the length of the light escaping path [116].

3.3 AlInN Nanowire Growth

AlInN core-shell nanowire LEDs and vertically aligned self-organized AlInN/GaN heterostructures were grown on n-Si(111) substrates using radio-frequency plasma-assisted molecular beam epitaxy. The RIBER RF-nitrogen plasma cell was supplied

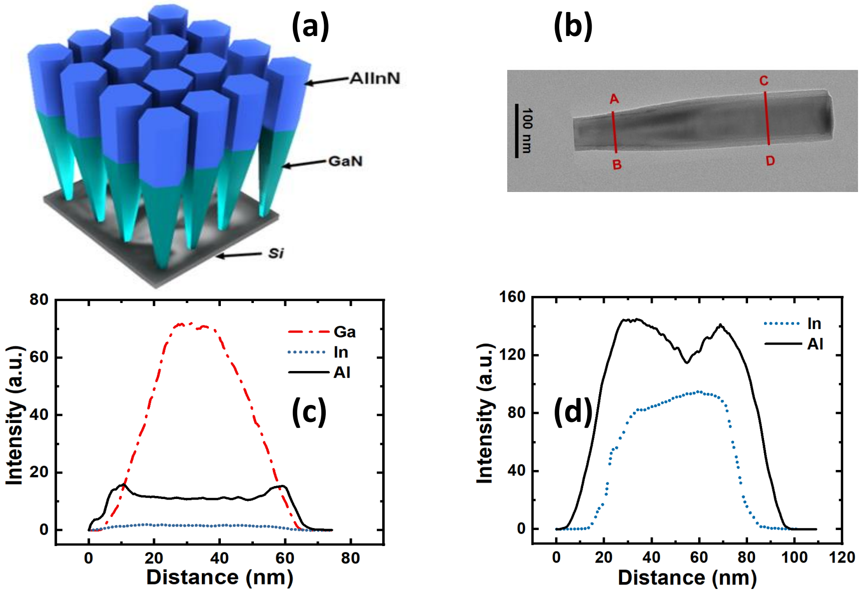

Figure 3.1 (a) Schematic structure of the AlInN nanowire on the GaN template. (b) A TEM image of the AlInN/GaN nanowire shows that it has a clear core-shell structure. EDXS line scan profile showing the quantitative variation in Ga, In and Al signals along lines A–B. (c) and variation in the In and Al signal along lines C–D.

with ultrahigh-quality nitrogen gas using an extraordinarily high-purity nitrogen production technology. This system consists of a Delux nitrogen purifying system, a valve control for bypass, a purifier, and heating control, as well as a bypass assembly life status indicator. The oxide on the substrate surface was desorbed in situ at 780 °C. As illustrated in Figure 3.1(a), under nitrogen-rich circumstances and without the aid of any external catalyst, first GaN nanowire templates were grown. The GaN nanowires were grown under the following conditions: 770 °C growth temperature, 1.0 sccm nitrogen flow rate, 400 W of forward plasma power, and Ga beam equivalent pressure of 6×10^{-8} Torr. Self-organized AlInN segments were then grown on top of the GaN nanowires to achieve UV light emission. The In and Al beam flux and/or substrate temperature can be changed to alter the In composition in the active zone. To improve the In incorporation, the growth temperature of the AlInN active areas was adjusted between 670 °C and 720 °C. Both the nitrogen flow rate and plasma

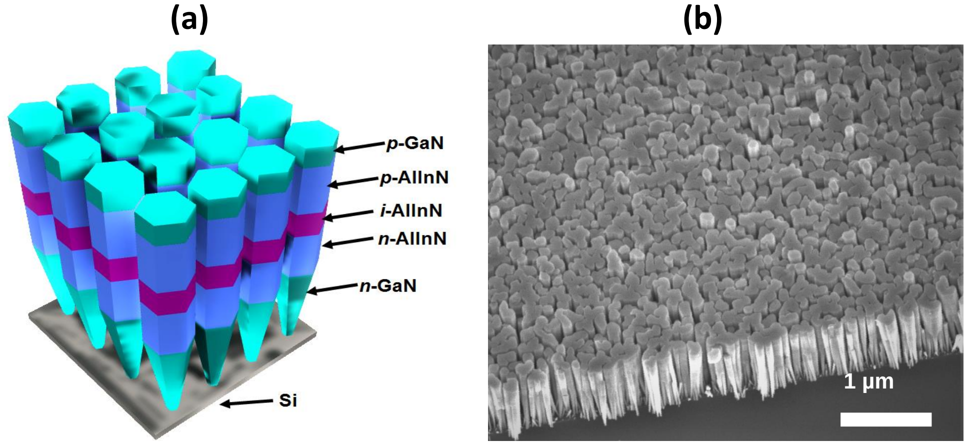

Figure 3.2 (a) Schematic diagram of the AlInN nanowire LED structure on Si. (b) 45° tilted scanning electron microscopy image of a typical AlInN nanowire LED sample showing uniform nanowires on Si.

power were held constant at 2.5 sccm and 400 W, respectively, during the epitaxial development of AlInN segments.

3.4 Structural Characterization

The structural characteristics of AlInN nanowires were examined using scanning transmission electron microscopy (STEM). As shown in Figure 3.1(b), the presence of GaN and AlInN segments is confirmed. Like other published articles by our group on InGaN and AlGaN nanowires [42, 76, 117], the wire diameter rose from the GaN segment to the AlInN part and remained constant at the top of the nanowire. Additionally, it was postulated that a core-shell AlInN/GaN structure may have also evolved on its own during the epitaxial growth of the AlInN layer. Energy dispersive X-ray spectroscopy (EDXS) analysis was carried out in the GaN and AlInN areas, denoted as lines A-B and C-D in Figure 3.1(b), respectively, to describe the compositional distribution in the nanowire. As corresponds to line scans A-B, the highest intensity of Ga signal is found in the center of the nanowire and decreased along the sidewalls of the nanowire, which is demonstrated in Figure 3.1(c). The Al signal, however, reached its peaks at the sidewalls and decreased towards the center of the nanowire. Even though the observed In signal was much weaker than Ga and Al signals, the existence of In was still determined by the detected In signals. As a result, it was suggested that a special GaN/AlInN radial core-shell heterostructure was grown. The EDXS line scan as shown in Figure 3.1(d) also revealed an AlInN shell surrounding the AlInN core at the top of the nanowire, which corresponds to line scans C–D. The In signal was confined within the nanowire. The Al signal was once again highest at the sidewalls and greatly reduced in the core region of the nanowire. The shell layer was calculated to have a thickness of around 13.6 nm at the top of the nanowire, which gradually reduced to a thickness of 8.4 nm at the bottom of the nanowire. These core-shell nanowire structures are formed similarly to the core-shell nanowires of AlGaN/GaN and AlGaN/AlInN that were previously reported [98, 118]. Additionally, the presence of the shell layer may greatly improve the optical characteristics of the underlying GaN nanowire templates and the AlInN core.

Using the ideal growth conditions for AlInN nanowires on GaN templates, AlInN/GaN UV nanowire LEDs were developed on Si substrates. Figure 3.2(a) shows a schematic diagram of the device, which consists of a 200 nm GaN:Si segment, a 100 nm $Al_xIn_{1-x}N$:Si /40 nm i-$Al_yIn_{1-y}N$ /100 nm $Al_xIn_{1-x}N$:Mg quantum wells and 10 nm GaN:Mg. To modify the emission wavelengths of these AlInN UV nanowire LEDs, the Al and In compositions in the active area may be adjusted by varying the Al/In flux ratios and/or the growth temperatures. As presented in Figure 3.2(b), the nanowires are organized perpendicularly on the substrate and have rather uniform heights, with top-of-wire diameters in the range of 90 nm. Such nanowire characteristics are appropriate for device fabrication.

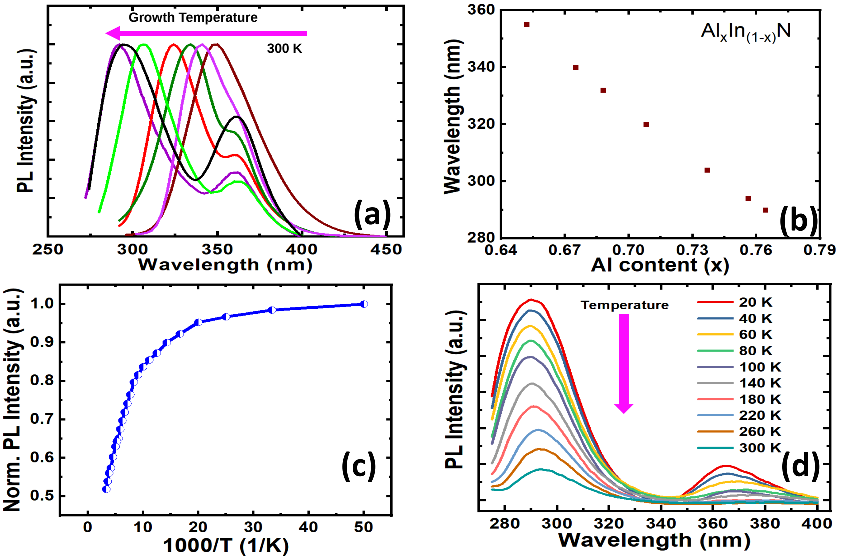

Figure 3.3 (a) PL spectra of AlInN/GaN nanowires. The peak emission varied from 290 nm to 355 nm. (b) PL peak wavelength versus estimated Al composition. (c) Temperature-dependent PL intensity of AlInN/GaN nanowires measured from 20 K to 300 K. (d) PL spectra of AlInN/GaN nanowires measured from 20 K to 300 K under an excitation power of 10 mW.

3.5 Optical Characterization

A 266 nm laser was used to analyze the photoluminescence (PL) spectra of AlInN nanowires on GaN templates. The PL spectra of several AlInN/GaN nanowire structures that were grown under various growth conditions are shown in Figure 3.3(a). As shown in the figure, by adjusting the Al content in the AlInN layers, the range of the peak emissions varied from 290 nm to 355 nm. In this investigation, the substrate temperature was raised from 670 °C to 720 °C while the Al/In beam equivalent pressure (BEP) ratio remained unchanged. The nitrogen flow rate of 2.5 sccm was maintained. The increased In adatom desorption at higher growth temperatures usually leads to a lower In composition in the AlInN, as a result, the peak emission shifted to shorter wavelengths as the substrate temperature increased. The peak wavelength at around 368 nm, as shown in Figure 3.3(a), is related to the emission from GaN nanowire templates. Using the following equation, the Al content in the AlInN layer is estimated,

$$E_{\text{Peak}}(x) \approx E_g(x) = xE_g(\text{AlN}) + (1\text{-}x)E_g(\text{InN}) - bx(1 - x),$$

where E_{Peak} is the PL peak energy at room temperature, x is the Al composition, and E_g is the bandgap energy. For the calculations, E_g(AlN) was considered to be 6.2 eV [9] and E_g(InN) was considered to be 0.64 eV [9], and the bowing parameter, b was taken as 3.4 eV [13]. As illustrated in Figure 3.3(b), the Al concentration was determined to be between 65.1% and 76.4%, which corresponds to an emission wavelength between 290 nm and 355 nm. AlInN nanowires with an emission wavelength of 295 nm with a strong emission intensity and a spectral linewidth of around 28 nm were seen at a growth temperature of 710 °C. The optical characteristics of these AlInN/GaN nanowires were subsequently studied using liquid helium with an excitation power of 10 mW to determine their IQEs at various temperatures ranging from 20 K to 300 K. Using the assumption that the IQE at 20 K is close to unity [85], the integrated PL intensities of emission from the AlInN layer at room temperature and at 20 K were compared to calculate the IQE.

As shown in Figure 3.3(c), the AlInN/GaN nanowire exhibits a relatively high IQE of around 52% at room temperature due to the strong carrier confinement offered by the AlInN shell and almost intrinsic AlInN core of the AlInN/GaN nanowire. The temperature-dependent PL spectra of AlInN/GaN nanowires, recorded from 20 K to 300 K, are shown in Figure 3.3(d). At 20 K, strong emissions at 290 nm was recorded from AlInN and at 364 nm was recorded from GaN segments. For the peak position of emission from the AlInN segment, S-shaped behavior was not seen. At room temperature, the AlGaN segment produced the peak emission at 295 nm, whereas the GaN layer produced the peak emission at $\sim$ 368 nm. Redshifts were observed for the peak wavelength emission from AlGaN and GaN, respectively with the increase of temperature from 20 K to 300 K. The cause of redshifts may be due to the bandgap shrinkages of AlGaN and GaN with the increase of temperature [119].

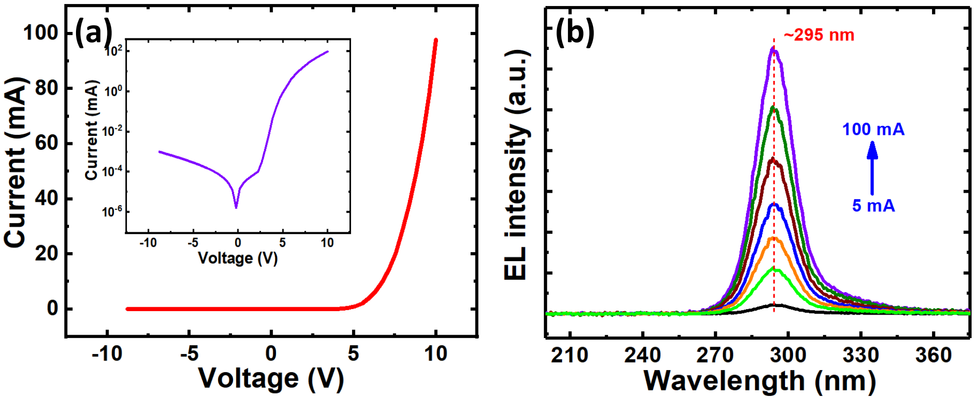

Figure 3.4 (a) I-V characteristics of the AlInN UV nanowire LED. The inset shows the I-V characteristics of the AlInN UV LED device on a semi-log scale. (b) EL spectra of the AlInN UV nanowire LEDs under an injection range of 5-100 mA.

3.6 Fabrication Process

The MBE-grown nanowire LED samples were then fabricated using the conventional lithography process as follows. To remove native oxides from the nanowire surface and the oxide layer from the backside of the Si substrates, the nanowire LED samples were first cleaned with HCl and subsequently with HF. Then, for *n*-contact, metal layers of Ti (20 nm) and Au (120 nm) were deposited on the backside of Si wafers. E-beam evaporation was used to deposit the *p*-metal contact of Ni (10 nm)/Au (10 nm) on top of the nanowire samples. The top sections of the nanowires must be connected together in order to improve the efficient current spreading of this *p*-contact layer, which may be accomplished by tilting the substrate holder at a specific angle during deposition. Layers of thick Ni (20 nm) /Au (120 nm) was then deposited on top of the device to act as a metal pad. The fabricated devices with contacts made of Ti/Au and Ni/Au were annealed at 550 °C for 1 minute. Unlike visible color InGaN/(Al)GaN nanowire LED fabrication, filling materials and indium tin oxide (ITO) were not employed in this process to avoid any light absorption in this UV wavelength region. Fabricated LEDs with chip areas of $\sim 500 \times 500\,\mu\text{m}^2$ were chosen for characterization.

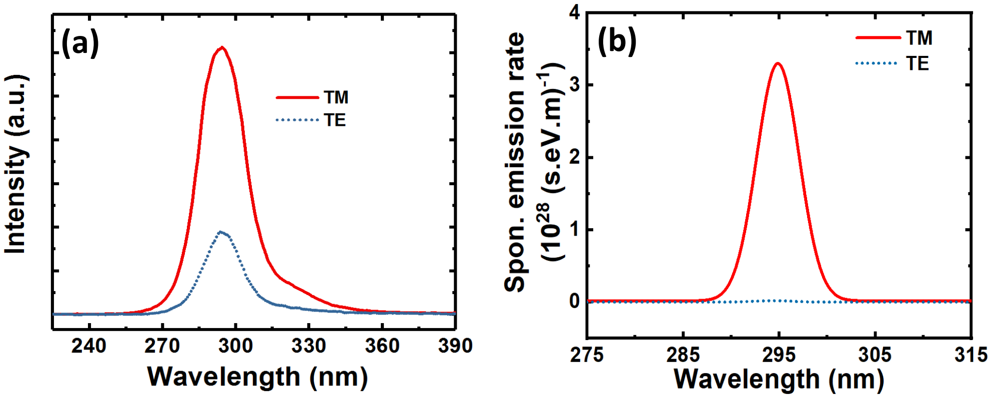

Figure 3.5 (a) TM and TE polarized spectra of the AlInN UV nanowire LED with an emission wavelength of 295 nm measured at 10 A/cm^2. (b) The simulation results of TM- and TE-polarized emission from AlInN nanowire LEDs at 295 nm.

As illustrated in Figure 3.4(a), AlInN LEDs exhibit very good current-voltage characteristics and low resistance at room temperature. It was determined that the leakage current was very low, with a value of around 1 μA at -8 V. The turn-on voltage of these UV nanowire LEDs was ~5 V, which is much lower than that of the existing thin-film AlGaN LEDs in the same wavelength range [120, 121] and is also better than/comparable to that of the recently reported AlGaN UV nanowire LEDs [85, 122, 123]. Electroluminescence (EL) spectra of the AlInN nanowire LEDs subjected to 5 mA to 100 mA injection currents is shown in Figure 3.4(b). Due to the low quantum-confined Stark effect (QCSE) in the LED devices, there was no visible change in the peak wavelength, confirming the superb crystalline quality of these AlInN nanowire heterostructures.

At room temperature, the light emission polarization features of AlInN UV nanowire LEDs were also investigated. Transverse-magnetic (TM) is defined as the electric field parallel to the c-axis (E$\|$c) and transverse-electric (TE) is defined as the electric field is perpendicular to it (E$\perp$c). The injection current during the

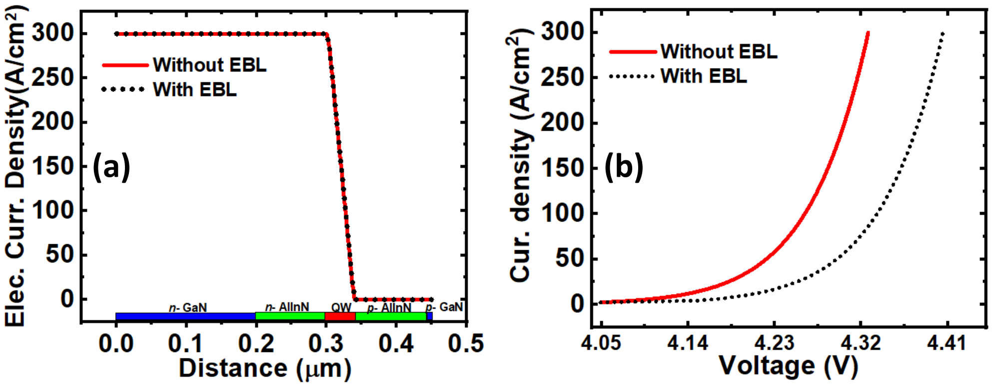

Figure 3.6 (a) The simulated electron density of the AlInN nanowire LEDs with and without EBL showing a similar trend of electron current distribution. (b) The simulated I-V characteristics of AlInN nanowire LEDs with and without EBL.

measurement was 10 A/cm2. As shown in Figure 3.5(a), the UV light emission was predominately TM polarized, which is around 4 times stronger than TE polarized emission. Figure 3.5(b) depicts that the TM-polarized emission was around two orders of magnitude brighter than the TE-polarized light, which is consistent with the observation in Figure 3.5(a). Others have shown a similar polarization trend for AlGaN LEDs in the same UV wavelength domain [48, 122]. This conclusion is crucial for the design of surface-emitting UV LEDs that use AlInN compounds to attain high light extraction efficiencies.

3.7 Carrier Transport in AlInN Nanowire LEDs

In addition to examining the performance of AlInN UV nanowire LEDs, an extensive simulation study is conducted to study the carrier transportation and compare the properties of AlInN nanowire LEDs with and without the incorporation of an electron blocking layer. As illustrated in Figure 3.6(a), it is evident that electron leakage does not occur or is low in both LED device topologies with a comparable electron current density distribution. Nevertheless, EBL has a significant effect on hole injection efficiency. The LED without EBL offers superior hole injection efficiency compared

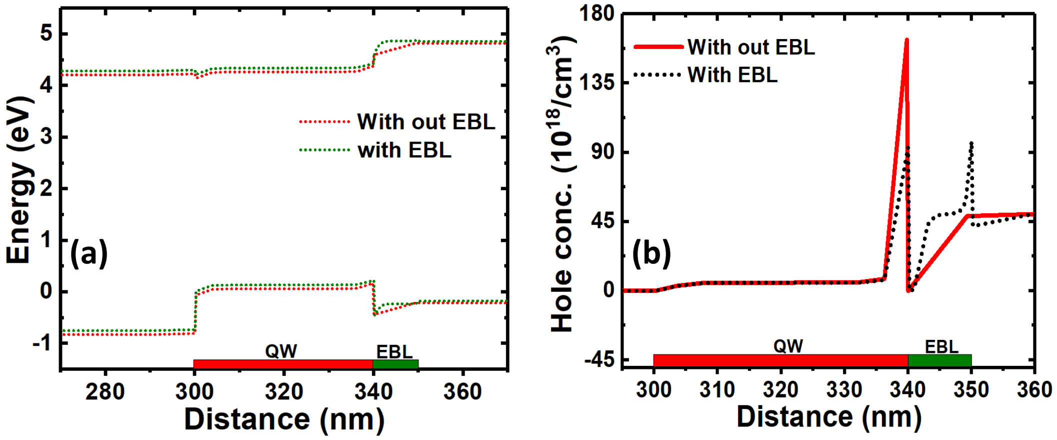

Figure 3.7 (a) Band diagrams of LEDs with and without EBL. (b) Hole concentration in LED with and without EBL.

to other LEDs. The band diagram of the LED with EBL reveals band bending in the valence band at the heterointerface of the EBL and quantum well, as shown in Figure 3.7(a), leads to hole accumulation at the beginning of the EBL can be seen from Figure 3.7(b).

As illustrated in Figure 3.6(b), this reduces the hole injection efficiency in the quantum well and results in a greater turn-on voltage for AlInN UV nanowire LEDs with EBL. The advantages of AlInN nanowire structures include the incorporation of nanowire UV LED architectures on GaN templates and the usage of a basic structure without an EBL for improved device performance. The EBL-free LED structure is crucial for the development of deep UV LEDs, since the Al composition is nearly at its maximum for deep-UV emission (below 240 nm). Therefore, the ideal EBL structure is constrained, necessitating a larger bandgap energy to avoid electron overflow efficiently. In addition, the usage of EBL will impact hole transport, resulting in decreased hole injection efficiency into the active portion of the device.

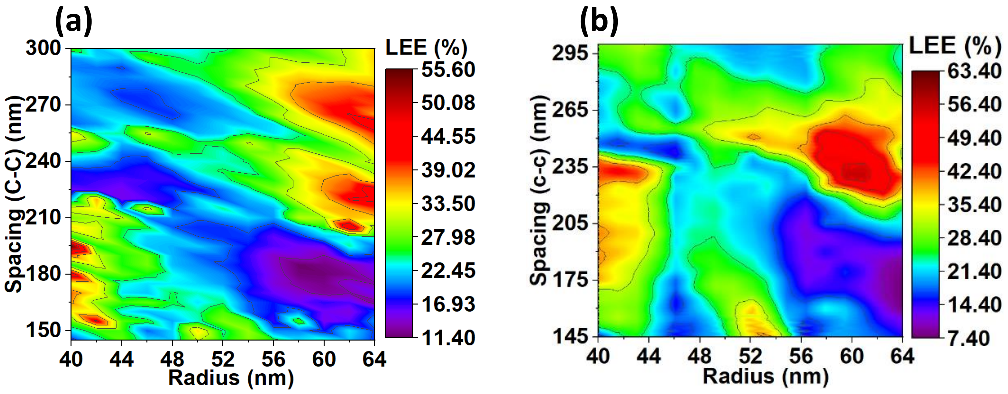

Figure 3.8 Contour plot of the LEE vs. nanowire radius and spacing for (a) square array, (b) hexagonal array of AlInN nanowire UV LEDs.

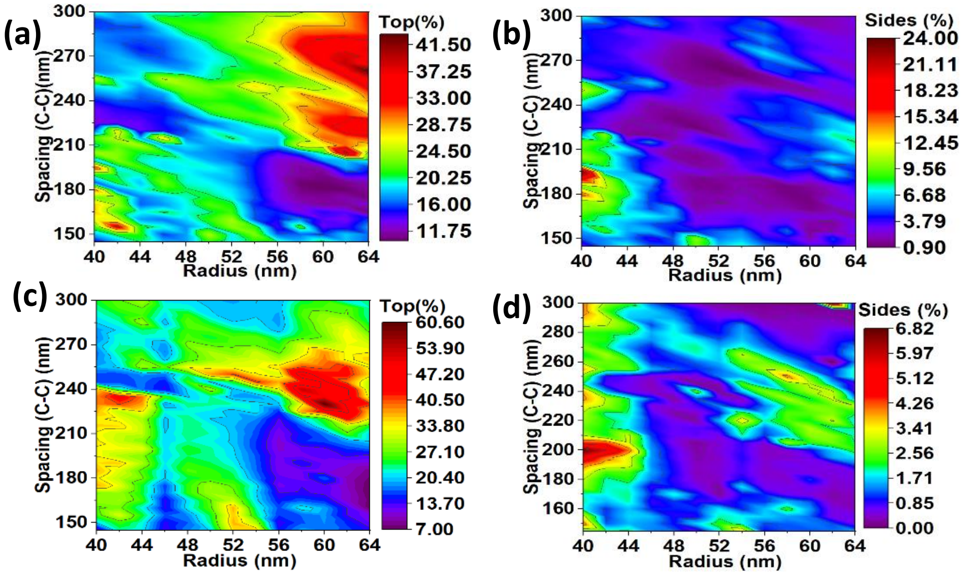

Figure 3.9 Contour plot of the LEE from top and sides vs. nanowire radius and spacing for square (a, b) and hexagonal (c, d) array structures of AlInN nanowire UV LEDs.

3.8 Boosting LEE using Photonic Crystal Structures

The LEE of AlInN nanowire UV LEDs is estimated using finite difference time domain (FDTD) simulation, which has been widely used in optical property analysis of III-nitride light-emitters [124,125]. In this study, LEE was estimated for randmoly grown and photonic crystal structure arrangements such as hexagon and square lattice of AlInN nanowire UV LEDs and thier performance is compared. For the fair comparision, number of nanowires in random and photonic crystal structures were considered same. The nanowire radius ranges of 40-64 nm and nanowire center-center spacing ranges of 145-300 nm were considered in the simulation. A single TM-polarized dipole source was positioned in the center of the active region for all the simulations, which is appropriate for estimating LEE for a large area LED device [126]. The all other material, structural parameters utilized in this study can be found elsewhere [50].

The average LEE found for nanowire arrays with random distribution was between 20% and 33%. For each independent investigation, LEE from the top surface and from the sides is measured, and it is determined that around 75% of the total LEE of 100% is emitted from the top surface, while approximately 25% is released from the side walls of the nanowire. This indicates that, despite the light being TM-polarized, the predominate direction of light emission is from the nanowire's top surface due to the substantial light scattering effect [66]. However, LEE for the random array of nanowires is quite low.

Contour plots of LEE vs nanowire radius and spacing for both hexagonal and square nanowire array topologies are shown in Figure 3.8 in order to understand of the dependence of LEE on nanowires geometry. As illustrated in Figure 3.8(a), a maximum LEE of 56% was estimated for a square array with a spacing of 195 nm and a radius of 40 nm. For a hexagonal nanowire array, a maximum LEE of 63% was computed for a spacing of 230 nm and a radius of 60 nm, as shown in Figure

3.8(b). It can be understood from Fig. 4 that the nanowires geometry plays an important role in directing the generated photons from the active region to the free space. The maximum LEE of hexagonal arrays of nanowire LED is also found to be greater than that of square arrays. This may be because the symmetry of the hexagonal array is greater than that of the square array, allowing guided modes in more directions to be turned into radiation modes [115, 127]. Therefore, optimizing the nanowire radius, spacing between nanowires, and nanowire arrangement might assist to overcome total internal reflection at the semiconductor-air interface, improve the chance of light escape, and subsequently raise the LEE. In the case of random nanowire UV LED design, however, spatially random and high contrast refractive index nanowires generate numerous scattering of light within the nanowires, which may localize the light within the nanowires and reduce LEE. The periodic array of nanowire LEDs is therefore extremely desirable for light propagation through the structure and into the surrounding air.

Further, the percentage of LEE for both the topologies from top and sides of the nanowire are estimated and provided in Figure 3.9. The obtained results in both cases support the vertical emission of the LEE, although the nanowire structure favors highly TM-polarized emission. For example, for a square array with a maximum LEE of 56%, 41% of light can be extracted from the top surface, as shown in Figure 3.9(a), and 15% can be extracted from the side walls of the nanowires, as shown in Figure 3.9(b). Also, for a maximum LEE of 63% in a hexagonal array, 60% of light can be extracted from the top surface, as shown in Figure 3.9(c), while only 3% of light can be extracted from the side walls of the nanowires, as shown in Figure 3.9(d).

3.9 Conclusion

In conclusion, the first AlInN axial nanowire UV LEDs with a relatively high IQE of 52% at room temperature is successfully demonstrated. There was no evidence of electron overflow in these nanowire UV emitters. The devices exhibited stable and strong TM-polarized light emission. Also, it is understood that the LEE can boosted using the photonic crystal arrangement of nanowires in AlInN nanowire UV LED. The obtained results revealed that the LEE of the square array and hexagonal array arrangement can reach upto 56% and 63%, respectively, with a dominant vertical light emission. Overall, This study provides an alternative approach for the fabrication of new types of high-performance ultraviolet light emitters.

CHAPTER 4

DESIGN OF ELECTRON BLOCKING LAYER-FREE ALGAN DEEP ULTRAVIOLET LIGHT-EMITTING DIODES

This chapter briefly discusses the problems involved with the integration of electron blocking layer (EBL) in AlGaN deep Ultraviolet (UV) light-emitting diodes (LEDs) and offers the design guidance to the EBL-free AlGaN deep UV LEDs to achieve improved carrier transportation and radiative recombination.

4.1 The Role of EBL

The typical schematic energy-band diagram of AlGaN deep UV LED with main functional regions are identified and represented in Figure 4.1. We do not consider the polarization effects and band bending in this figure for simplicity of understanding. The electrons come from the *n*-AlGaN current injection layer, which is (1); a part of electrons recombine radiatively and non-radiatively with captured holes in the active region (2); Al-rich *p*-AlGaN EBL (3) for effective electron blocking but blocks incoming holes as well; the *p*-AlGaN hole injection layer (4) to improve hole transport; and (5) the *p*-GaN contact layer for efficient hole injection. However, the lower effective mass of electrons leads to higher mobility and drift velocity attributed to the enormous difference in the transportation of electron and hole behavior in AlGaN UV LEDs. Besides, default strong induced polarization fields, and quantum-confined Stark effect (QCSE) in the active region contribute significantly to the separation of electron and hole wave functions, leading to reduced carrier confinement [128]. Altogether, electrons can easily escape from the active region without being captured with holes, leak into the *p*-region, and causes significant efficiency droop. The electron leakage and efficiency droop proportionately increase with higher current injections, leading to relatively impoverished radiative recombination and low output power in

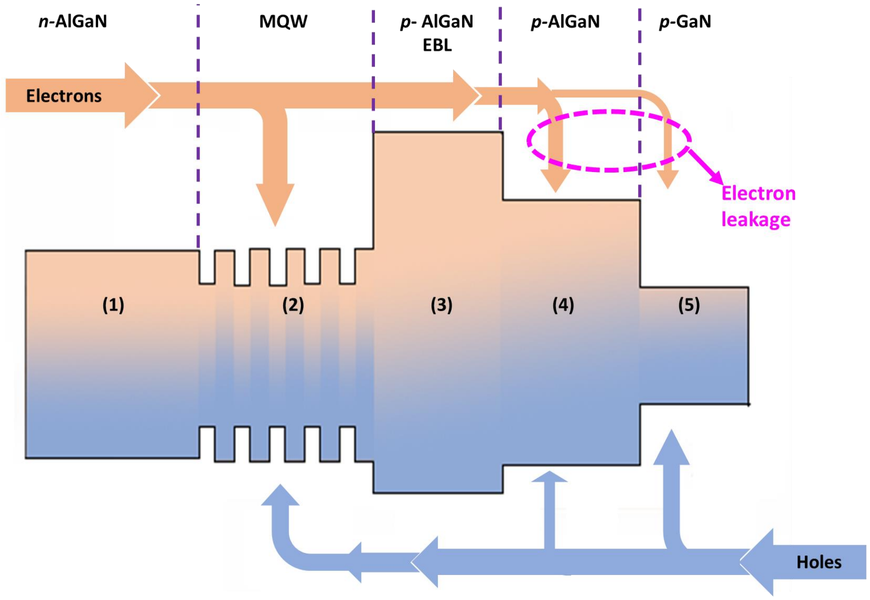

Figure 4.1 Schematic energy-band diagram of a conventional AlGaN UV LED.

AlGaN UV LEDs [128], [41]. This problem has been addressed by integrating Al-rich (higher energy-band gap) p-AlGaN layer between the active region and p-region [129] which is called EBL. The EBL increases the conduction band barrier height (CBBH) and electrons require higher energy to overcome the EBL.

Here, it is important to understand that the integration EBL in LED can prevent electron leakage from the active region but this is to an extent and not completely. Simultaneously, EBL can also introduce the following problems, such as (1) hindering of hole injection due to the generation of positive sheet polarization charges at the interface of LQB and EBL [45], as shown in Figure 4.2. This has a detrimental effect on carrier injection efficiency, as the electrostatic accumulation of positively charged holes on the EBL promotes the escape of negatively charged electrons from the active region through the EBL; (2) inefficient p-doping in high Al-content AlGaN EBL for deep UV LEDs ($<$ 300 nm wavelength emission) due to the activation energy of the Mg acceptor increasing rapidly with the increased Al composition [87]. In this context, many special type band-engineered EBLs have been proposed to mitigate

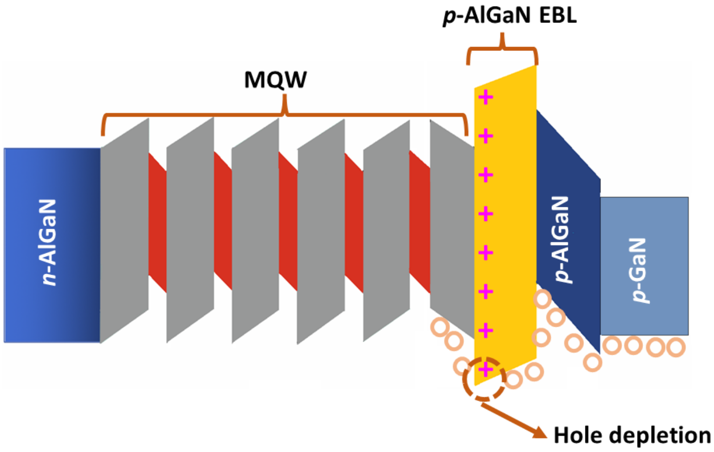

Figure 4.2 Schematic energy-band diagram of a conventional AlGaN UV LED including polarization effect and band bending.

above mentioned challenges and improve the carrier transportation in these light-emitters.

4.2 Band-Engineering of EBL

Firstly, it is straightforward to tune the band structure of a device by incorporating a functional layer to influence the carrier transport behavior. Different types of EBLs have been proposed, as shown in Figure 4.3, to overcome the challenges of the conventional EBL. For instance, in the *p*-type EBL region, Zhang et al. proposed the incorporation of a very thin AlGaN layer in a traditional *p*-EBL structure to form a *p*-AlGaN/ AlGaN/*p*-AlGaN EBL heterostructure, aiming to improve the hole transport capability due to intraband tunneling process for holes [130]. Alternatively, *p*-EBL with the Al profile in a linearly graded up [131], triangular shape (grading up and down symmetrically) [132, 133] along the growth direction has been designed and analyzed, which provides a considerable electron blocking ability, controlled polarization and such a device was found to have a relatively smaller forward bias as well.

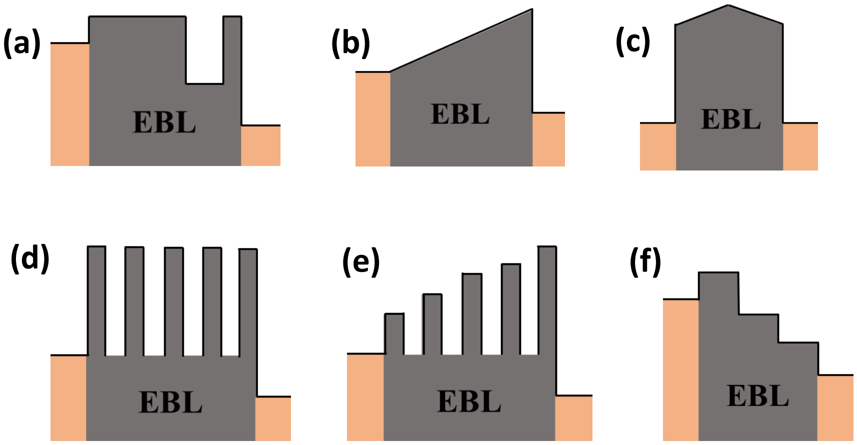

Figure 4.3 Engineered EBLs with different designs (a) $Al_xGa_{1-x}N/Al_yGa_{1-y}N/Al_xGa_{1-x}N$ type EBL (b) EBL with linearly graded (upwards) Al composition (c) EBL with triangular shape graded (up grading then down grading) (d) Superlattice based EBL (e) Graded superlattice EBL (f) Gradient EBL.

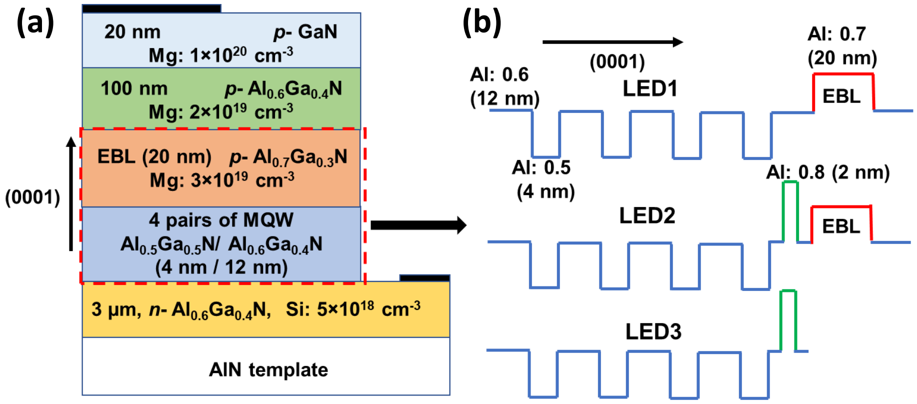

Figure 4.4 (a) Schematic representation of LED1. (b) Conduction band diagrams of LED1, LED2 and LED3.

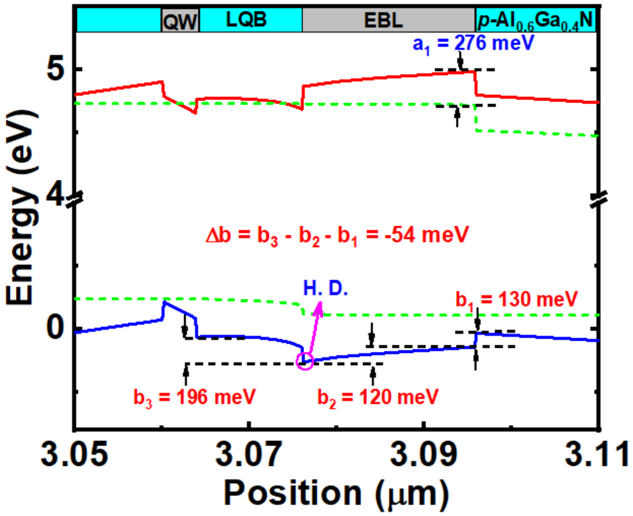

Figure 4.5 Estimated energy-band diagram of LED1 at 150 A/cm^2 current density.

Further, *p*-EBLs with the incorporation of a superlattice (SL) structures also demonstrate the ability to create high-performance DUV LEDs by improving the hole injection capability and transportation due to reduced Mg activation energy [134,135]. Inspired by these studies, a graded SL EBL was designed for further carrier injection [136]. In another work, a novel double-sided step graded SL EBL has been proposed to improve hole activation and hole injection [137]. All these strategies are intended to partially improve the capability of controlling electron leakage and improve hole injection, only to an extent, but not completely. Some of these structures, positive sheet polarization charges at the interface of LQB and EBL—have been controlled or reduced to some extent but not eliminated completely. Importantly, most of the engineered EBLs are still highly *p*-type doped materials, therefore, inefficient *p*-doping due to higher Mg activation energy still exists.

4.3 EBL Free AlGaN Deep UV LED Design

To overcome the above discussed challenges in AlGaN deep UV LEDs, efficient EBL free LED designs can be a good choice. With this motivation, an EBL free AlGaN UV

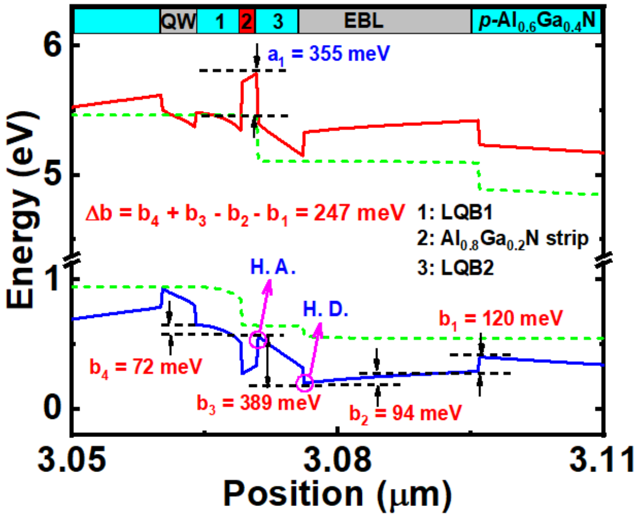

Figure 4.6 Calculated energy-band diagram of LED2 at 150 A/cm^2 current density. H.D. and H.A. are holes depletion and accumulation interfaces.

LED operating at 270 nm wavelength is designed, and it's performance is compared with that of conventional EBL based LEDs. Instead of integrating a p-type EBL between the last QB and the hole-supplying layer in the p-region, it is proposed here to insert an optimized, thin, undoped $Al_{0.8}Ga_{0.2}N$ strip in the middle of the last QB. This $Al_{0.8}Ga_{0.2}N$ strip raises the effective conduction band barrier height, preventing electron leakage into the p-type region [138]. Furthermore, it promotes the development of negative polarization sheet charges, resulting in the buildup of holes at the $Al_{0.8}Ga_{0.2}N$ strip/last QB interface and efficient hole transportation into multi quantum wells (QWs) through the intraband tunneling action [45]. The improved carrier injection into multi QWs improves the proposed EBL free LED's internal quantum efficiency (IQE) and output power.

Three LEDs are investigated to estimate the efficacy of the proposed EBL free deep UV LED, as shown in Figure 4.4. LED1 is a reference structure for an AlGaN-based LED with conventional EBL grown on a c-plane AlN template. LED1 contains 3 μm thick Si-doped $Al_{0.6}Ga_{0.4}N$ layer (5×10^{18} cm^{-3}), the active region consists of four pairs of 3 nm undoped $Al_{0.5}Ga_{0.5}N$ QW and 12 nm $Al_{0.6}Ga_{0.4}N$ QB layers followed by a 20 nm Mg-doped $Al_{0.7}Ga_{0.3}N$ EBL (3×10^{19} cm^{-3}), then a 100 nm Mg-doped $Al_{0.6}Ga_{0.4}N$ layer ($2 \times 10^{19}\,cm^{-3}$) and a 20 nm Mg-doped GaN contact layer (1×10^{20} cm^{-3}). The device area is $300\mu m \times 300\mu$m, and the emission wavelength is planned to be 270 nm. LED2 has a similar construction to LED1, with the exception of a 2 nm undoped $Al_{0.8}Ga_{0.2}N$ strip integrated in the centre of the LQB. LED3 is the structure we suggest by deleting EBL from LED2.

4.4 LED Device Modeling and Parameters

Device simulations are performed using Crosslight APSYS tool. The electrical and optical properties of LED structures are carefully analyzed in this study (see more details in Chapter 2, section 2.4). The energy band diagrams of the LED structures are estimated by using 6×6 k·p model [31]. The band gap of GaN and AlN are considered as 3.42 eV, 6.2 eV respectively [32]. The bowing parameter and band offset of AlGaN are set to be 0.94 eV, and 0.67/0.33 [33]. The radiative recombination coefficient, Auger recombination coefficient and Shockley-Read-Hall (SRH) recombination lifetime are considered as 2.13×10^{-11} cm^3/s, 2.88×10^{-30} cm^6/s, and 15 ns respectively [34]. The background loss is set as 2000 m^{-1} and simulations are performed at room temperature.

Furthermore, the activation energy of Si-doped n-$Al_{0.6}Ga_{0.4}N$ is set as 15 meV [35], whereas the activation energy of Mg-doped p-$Al_{0.7}Ga_{0.3}N$, p-$Al_{0.6}Ga_{0.4}N$ and p-GaN is considered as 408 meV, 374 meV and 170 meV, respectively [87,87]. Moreover, tunneling models are taken into account in LED2 and LED3. The built-in polarization charges resulting from spontaneous and piezoelectric polarization are considered and assumed to be 50% of the theoretical value. The methods described by Fiorentini et al. are used to determine spontaneous and piezoelectric polarization in these simulations [139].

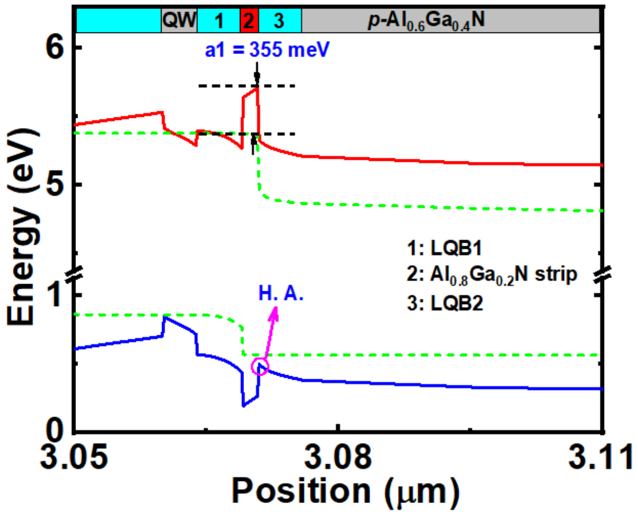

Figure 4.7 Estimated energy-band diagram of LED3 at 150 A/cm^2 current density.

4.5 Results and Discussion

The energy band diagrams for LED1, LED2, and LED3 are calculated to evaluate the performance of the proposed EBL free structure, which are shown in Figures 4.5, 4.6, and 4.7. The effective conduction band barrier height (a1) for a conventional LED structure with a *p*-AlGaN EBL, LED1, is 276 meV, as illustrated in Figure 4.5. In addition, the holes are subjected to the barrier height (b1) at the interface of EBL/hole supplying layer *p*-Al$_{0.6}$Ga$_{0.4}$N, and b1 is 130 meV. The transportation of holes is carried out as a result of the thermionic emission process. Meanwhile, holes must gain an extra 120 meV of energy (b2) to reach the LQB/EBL interface. Furthermore, the formation of positive polarization sheet charges at this interface lowers the hole concentration due to the hole depletion effect, as seen in Figure 4.8(a). As a result, another valence band barrier with an effective barrier height (b3) of 196 meV is formed. The holes are transferred here by thermionic emission and then injected into multi QWs. The energy gained by the holes during this operation is Δb = b3 - b2 - b1 = -54 meV.

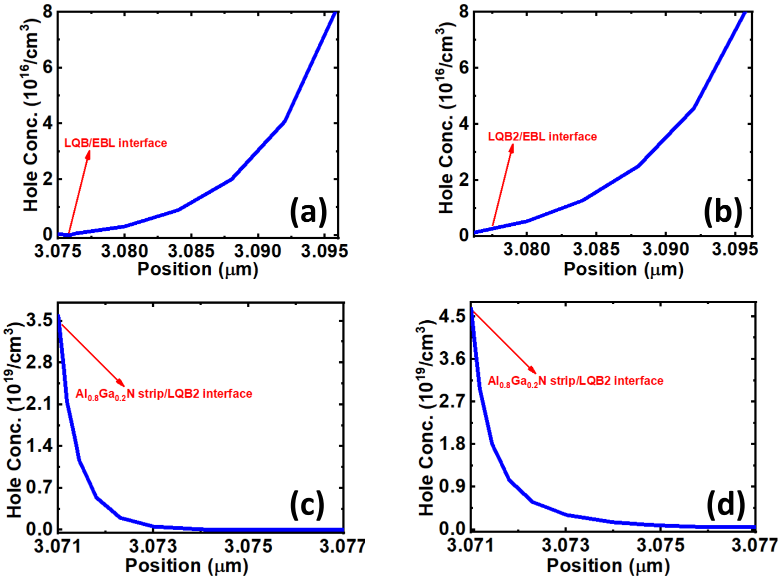

Figure 4.8 Hole concentration at (a) LQB/EBL interface in LED1 i.e., holes depletion interface, (b) LQB2/EBL interface in LED2 i.e., holes depletion interface, (c) $Al_{0.8}Ga_{0.2}N$ strip/LQB2 interface in LED2 i.e., holes accumulation interface, (d) $Al_{0.8}Ga_{0.2}N$ strip/LQB2 interface in LED3 i.e., holes accumulation interface.

Figure 4.6 shows E-B diagram of LED2. In this case, a 2 nm undoped $Al_{0.8}Ga_{0.2}N$ strip is inserted in the middle of last QB (LQB). LQB1 is first half of LQB before the insertion of strip and LQB2 is second half of LQB after the integration of the strip. The effective conduction band barrier height (a1) is 355 meV at the integration of strip in the LQB. The holes experience the barrier height (b1) of 120 meV at the heterointerface of EBL and hole supplying layer p-$Al_{0.6}Ga_{0.4}N$, require an energy (b2) of 94 meV to reach LQB2/EBL interface. The hole transport is supported by the thermionic emission process. Moreover, generation of positive polarization sheet charges can be observed at LQB2/EBL interface and it is similar to LED1. As a result, there exits hole depletion region and is presented in Figure 4.8(b). From this figure, it is understood that hole concentration is decreasing from EBL/hole supplying layer p-$Al_{0.6}Ga_{0.4}N$ interface to LQB2/EBL interface.

Next, the holes are injected into multi QWs by crossing the AlGaN strip via intraband tunneling and thermionic emission process. The formation of negative

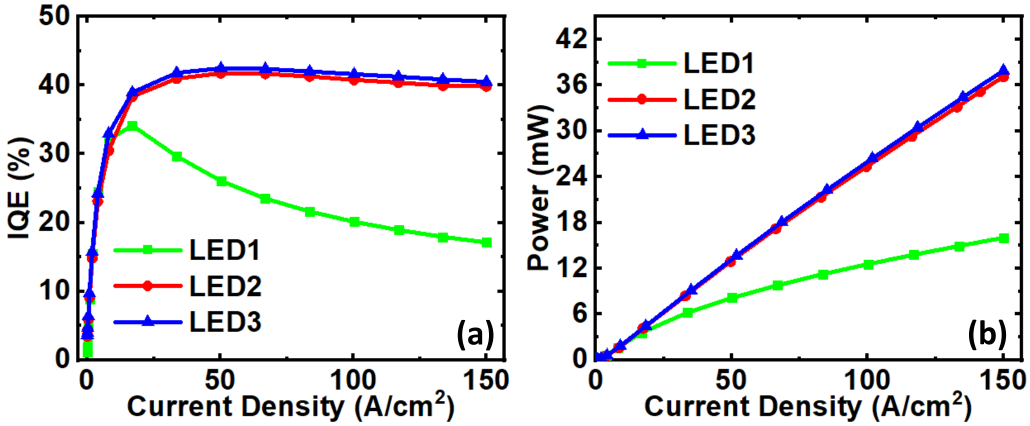

Figure 4.9 Estimated (a) IQE, (b) output power of LED1, LED2 and LED3.

polarization sheet charges at $Al_{0.8}Ga_{0.2}N$ strip/LQB2 interface can be observed and it reduces the hole depletion effect and improves the holes concentration by accumulating there. This phenomenon can be seen from Figure 4.8(c). During this process, holes obtain energy of 389 meV at b3 and 72 meV at b4. The net energy gained by holes is b4+b3-b2-b1 = 247 meV and can be seen clearly from 4.6. Due to higher effective conduction band height of LED2 which prevents the electron leakage into *p*-region and insertion of 2 nm thick $Al_{0.8}Ga_{0.2}N$ strip in LQB is responsible for intraband tunneling of holes into multi QWs which improves the hole injection efficiency. As a result, LED2 shows improved performance in terms of IQE and output optical power compared to LED1 and this can be seen from Figure 4.9.

LED2 performance can be increased further by avoiding the creation of positive polarization sheet charges at the LQB2/EBL interface, which enhances hole injection, which is feasible with the removal of EBL. This is possible with the proposed structure, LED3. LED3 has the same construction as LED2 but without the EBL. The energy-band diagram of proposed EBL free LED3 is shown in Figure 4.7 and calculated effective conduction barrier height (a1) is 355 meV, which is same as in LED2. The hole transportation is carried out via intraband tunneling and thermionic

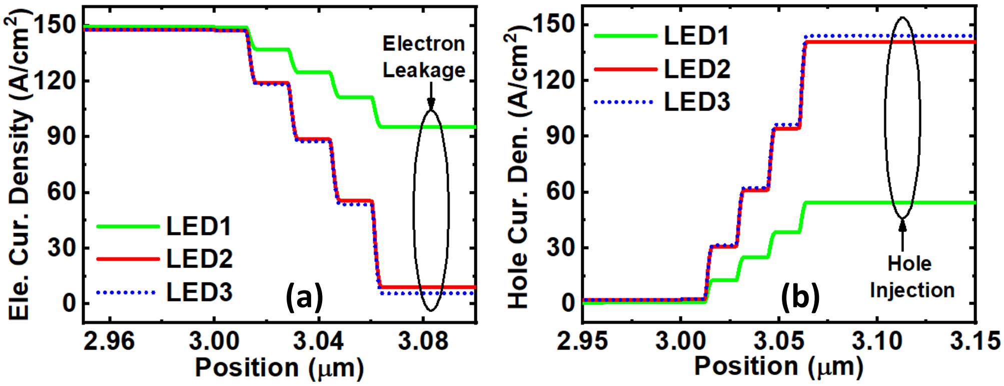

Figure 4.10 (a) Electron current density, (b) Hole current density of LED1, LED2 and LED3.

emission process at $Al_{0.8}Ga_{0.2}N$ strip. In addition, negative polarization sheet charges formed at $Al_{0.8}Ga_{0.2}N$ strip/LQB2 interface and hole depletion effect is not observed in LED3 which enhances the hole injection into multi QWs. The hole concentration at Al0.8Ga0.2N strip/LQB2 interface is presented in Figure 4.8(d). Therefore, the increase in hole concentration can be seen clearly in this Figure, and it is more than at LED2 at this interface. Overall, LED3 outperforms LED2 by preventing the creation of positive polarization sheet charges at the LQB2/EBL interface like in LED2, and by maintaining the requisite effective conduction band barrier height. As a result, LED3 must have superior carrier injection, which is responsible for the high IQE and output power displayed in Figures 4.9(a) and (b).

To further understand the performance of the proposed structure, we have calculated electron and hole current densities of LED1, LED2 and LED3 and are shown in Figure 4.10. It is clearly understood from Figure 4.10(a) that LED3 has negligible and less electron leakage after the active region than LED1 and LED2. This is due to the high effective conduction band barrier height as shown in Figure 4.7. In addition, as shown in Figure 4.10(b), it has a higher hole injection efficiency than others. This resulted from the incorporation of an optimum AlGaN strip into the

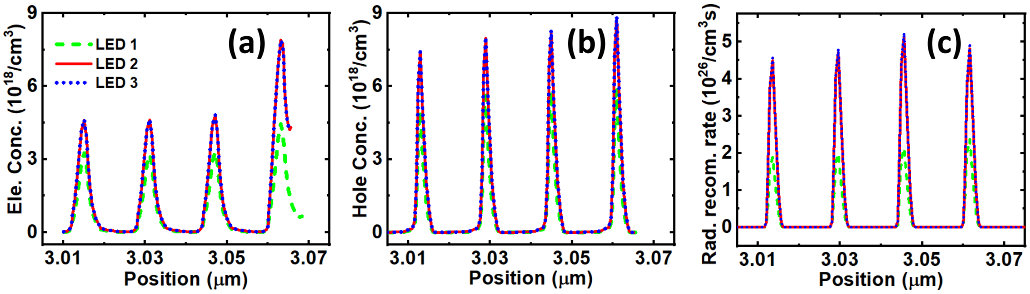

Figure 4.11 (a) Electron concentration, (b) Hole concentration, (c) Radiative recombination rate of LED1, LED2 and LED3.

LQB, which enabled intraband tunneling of holes and hence enhanced hole injection. Higher IQE and output optical power are due to low electron leakage into the *p*-region and increased hole injection into the active area of LED3. However, because to LED1's inadequate electron blocking capabilities, most electrons escape into the *p*-region and consume incoming holes, resulting in non-radiative recombination. This reduces hole injection into the active area, which causes IQE droop and decreased output optical power. As shown in Figure 4.9(a), the predicted IQE droop in LED1 is about 50%, but the suggested LED3 has just 2% IQE droop. In Figure 4.11, the carrier concentration and radiative recombination in the multi QWs of LED1, LED2, and LED3 are computed. As predicted, the electron, hole, and radiative recombination concentrations improve from LED1 to LED2, with LED3 having greater values than others.

To get the optimal AlGaN strip composition, LED2 is simulated with Al compositions of 0.7, 0.75, 0.8, 0.85, 0.9, and 0.95 in 2 nm undoped AlGaN strips. Effective conduction band barrier heights are determined to be 241 meV, 285 meV, 355 meV, 329 meV, 316 meV, and 294 meV, respectively. Because the energy band gap of $Al_xGa_{1-x}N$ grows with Al concentration, $Al_{0.95}Ga_{0.05}N$ is expected to have a greater conduction band barrier height. In our investigation, the effective conduction barrier height grew until the Al concentration of the strip reached 0.8, at which

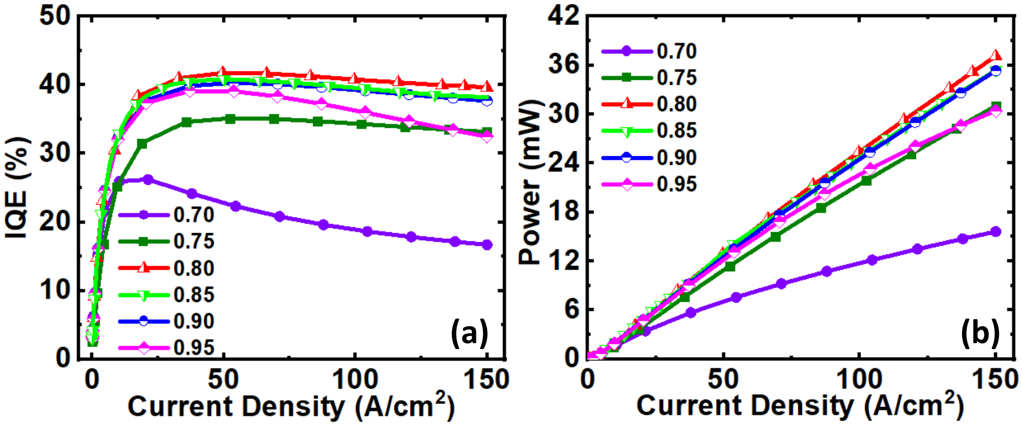

Figure 4.12 Estimated (a) IQE, (b) Output power of LED2 with different Al content of $Al_xGa_{1-x}N$ strips.

point it declined. This is owing to extreme band banding at the LQB1/AlGaN strip contact, which can be caused by a greater lattice mismatch. As a result, $Al_{0.8}Ga_{0.2}N$ has the largest conduction band barrier height, which prevents electron leaking into the *p*-region. Therefore, LEDs using an $Al_{0.8}Ga_{0.2}N$strip are projected to have higher IQE and output power than previous examples. Figure 4.12(a) depicts the estimated IQE, whereas Figure 4.12(b) depicts the computed output power. From these figures, it is observed that LED with $Al_{0.8}Ga_{0.2}N$ strip has better IQE and output power.

Finally, in order to get the optimal structure, the thickness of the $Al_{0.8}Ga_{0.2}N$ strip in LED3 was investigated. The IQE and output optical power of LED3 in this work are engineered by altering the thickness of the AlGaN strip at various values, including 1 nm, 2 nm, 3 nm, 4 nm, and 5 nm. The greater thickness of the $Al_{0.8}Ga_{0.2}N$ strip, on the other hand, may impede intraband tunneling for holes, resulting in reduced hole injection [45]. As a result, as seen in Figure 4.13(a), the IQE worsens with thicker AlGaN strips. As seen in Figure 4.13(b), this results in decreasing output power as the strip thickness increases. As a result, a 1 nm thick $Al_{0.8}Ga_{0.2}N$ strip is the best option for our suggested structure LED3.

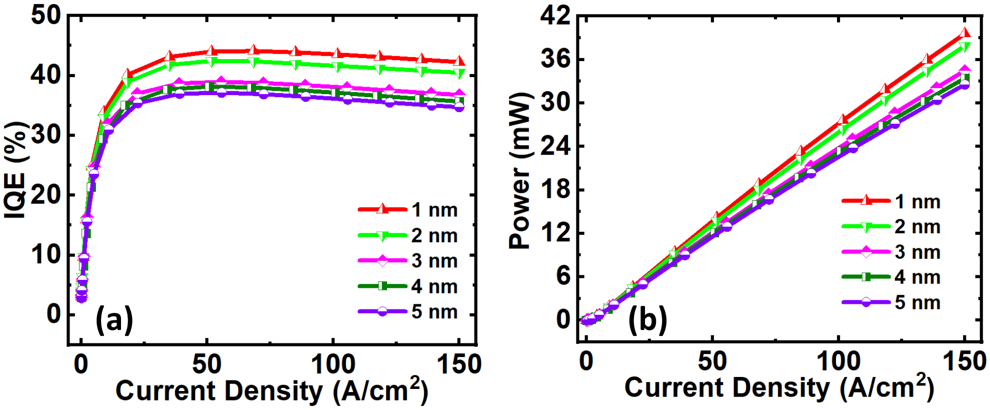

Figure 4.13 Calculated (a) IQE, (b) Output power of LED3 with different thickness of $Al_{0.8}Ga_{0.2}N$ strip.

4.6 Conclusion

In this chapter, the role of EBL in AlGaN deep UV LEDs and importance of EBL free LED designs are explained. Further, this work presented highly efficient EBL free AlGaN UV LED emitting at 270 nm wavelength with alomost negligible IQE droop. After rigours analysis, it is understood that the proposed 1 nm $Al_{0.8}Ga_{0.2}N$ strip-in-a-barrier structure improved the carrier injection into multi QWs, IQE and output power compared to conventional LED structure. Therefore, the proposed structure has great potential to produce efficient UV light emitters for practical applications.

CHAPTER 5

IMPLEMENTATION OF ELECTRON BLOCKING LAYER-FREE ALGAN DEEP ULTRAVIOLET LIGHT-EMITTING DIODES USING A STRIP-IN-A-BARRIER STRUCTURE

Though research on AlGaN-based ultraviolet (UV) light-emitting diodes (LEDs) is performed extensively but it has remained difficult to achieve high efficiency at shorter wavelengths in the deep UV regime due to several challenges [52]. One of the critical issues is the internal quantum efficiency (IQE) and efficiency droop at high injection current, due to electron overflow [128] and increased non-radiative recombination [140]. To mitigate the electron overflow, an electron blocking layer (EBL) has been introduced in between the active region and the *p*-region [129]. As described in Chapter 3, Although, EBL can suppress the electron overflow, the hole injection efficiency is also strongly affected, due to the formation of positive polarization sheet charges at the heterointerface of the last quantum barrier (QB) and EBL [45, 46]. Moreover, efficient *p*-doping in high Al content EBL is difficult due to the high Mg activation energy in such a high Al content layer.

In this context, high-performance EBL-free AlGaN deep UV LEDs using a strip-in-a-barrier structure at 284.5 nm wavelength emission have been reported which overcome the aforementioned problems related to the EBL. In the proposed structure, the EBL was successfully eliminated by integrating the engineered thin intrinsic $Al_xGa_{1-x}N$ strip into the middle of QBs without affecting the carrier injection and transportation. The resulting strip-in-a-barrier structure shows notably mitigated electron leakage and boosted hole injection into the active region, therefore generating higher carrier radiative recombination and quantum efficiency. Moreover, the elimination of EBL avoids the formation of positive polarization sheet charges at the last QB/EBL interface could improve the hole injection into the active region.

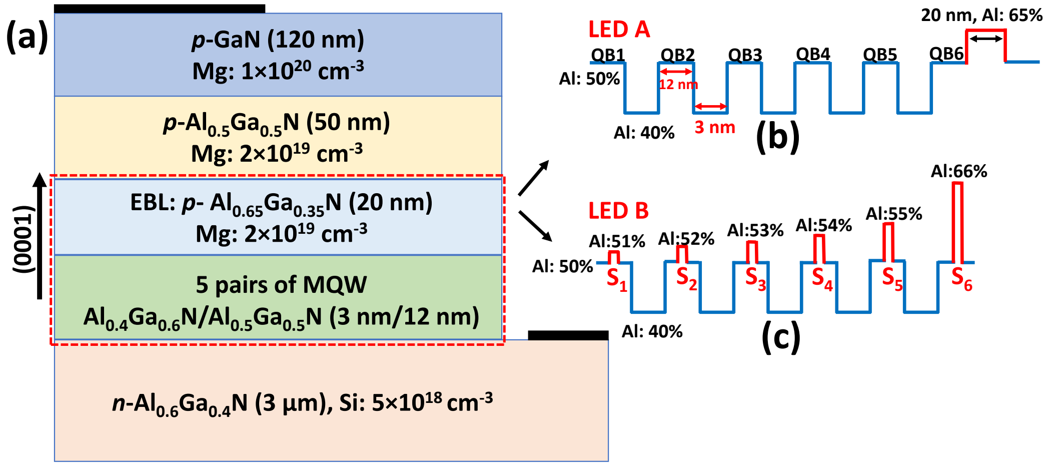

Figure 5.1 (a) Schematic diagram of the reference deep UV LED i.e. LED A, conduction band of (b) LED A, and (c) proposed strip-in-a-barrier deep UV LED i.e., LED B.

5.1 Device Structure

As shown in Figure 5.1, the conventional structure, LED A, considered as a reference consists of a 3 μm n-Al$_{0.6}$Ga$_{0.4}$N layer (Si: 5 $\times 10^{18}$ cm^{-3}), 5 periods of 3 nm Al$_{0.4}$Ga$_{0.6}$N quantum wells are sandwiched between 12 nm Al$_{0.5}$Ga$_{0.5}$N QBs, a 20 nm p-Al$_{0.65}$Ga$_{0.35}$N (Mg: 2 $\times 10^{19}$ cm^{-3}) EBL, a 50 nm p-Al$_{0.5}$Ga$_{0.5}$N (Mg: 2 $\times 10^{19}$ cm^{-3}) cladding layer, and a 120 nm p-GaN (Mg: 1 $\times 10^{20}$ cm^{-3}) contact layer. The device area is 400 × 400 μm^2. The conduction band schematic of the active region and EBL of LED A is presented in Figure 5.1(b). The proposed strip-in-a-barrier structure, LED B, presented in Figure 5.1(c), attained by integrating 2 nm intrinsic Al$_x$Ga$_{1-x}$N strip in the middle of each QB and removing EBL from LED A. The optimized Al composition (x) in Al$_x$Ga$_{1-x}$N strips (S$_1$ – S$_6$) are 0.51, 0.52, 0.53, 0.54, 0.55, and 0.66 respectively.

5.2 Device Parameters

The following parameters provided in Table 5.1 are considered while building the device model for this study. The energy band diagrams of the LED structures are estimated by using a 6×6 k.p model [97]. The bowing parameter and band offset

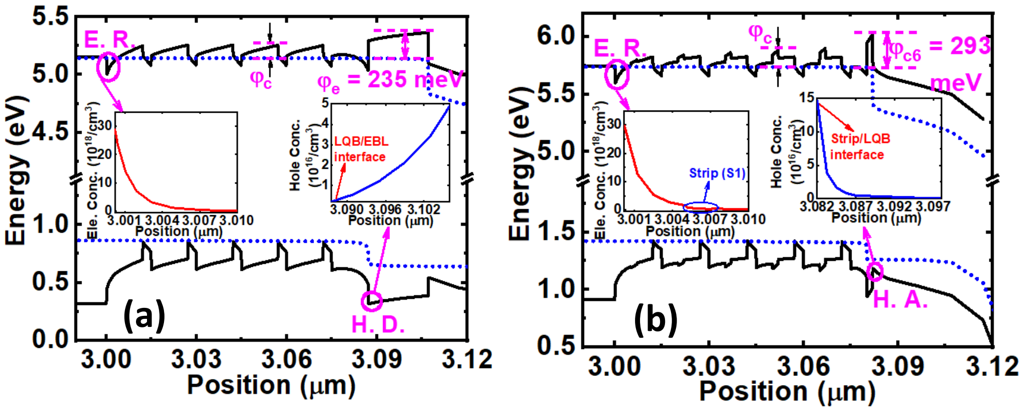

Figure 5.2 Energy band diagram of (a) LED A, (b) LED B at 60 mA current injection. E.R. is the electron reservoir region, H.D. is the hole depletion region, and H.A. is the hole accumulation region.

of AlGaN are set to be 0.94 eV, and 0.67/0.33 [141]. The Mg activation energy of $Al_xGa_{1-x}N$ for 0<x<1 is set to scale linearly [44] from 170 meV to 510 meV. The SRH recombination lifetime, radiative, Auger recombination coefficient and light extraction efficiency are set as 15 ns, 2.13×10^{-11}cm^3/s and 2.88×10^{-30}cm^6/s and 15% respectively [142]. The energy bandgap of GaN and AlN are estimated using Varshni formula [143]. Where Eg(T) and Eg(0) are the energy bandgap at temperatures T and 0 K respectively. a and b are material constants. The values of a, b, and Eg(0) for GaN are 0.909 meV/K, 830 K, and 3.507 eV. The corresponding values for AlN are 1.799 meV/K, 1462 K, and 6.23 eV, respectively. The carrier mobility is estimated using the Cauchy-Thomas approximation [144]. The polarization charge due to both spontaneous and piezoelectric polarization effect is estimated using the method proposed by Fiorentini et al. [139] and only 50% of the estimated value is considered in our model and other parameters can be found elsewhere [6].

5.3 Energy Band Diagram

The estimated energy band diagrams for LED A and LED B at 60 mA current injection are shown in Figure 5.2. φ_{cn} and φ_{e} are the effective conduction band barrier height at the corresponding barrier (n) and EBL respectively. As seen in Figure 5.2(a), the φ_{c} for all QBs except last QB i.e., φ_{c1} - φ_{c5} is 127 meV, φ_{c6} value at last QB is 37 meV due to severe band bending, and φ_{e} is 235 meV for LED A. The φ_{c} value due to integrated strips for all six barriers in the proposed EBL free LED B i.e., φ_{c1} - φ_{c6} is 80 meV, 122 meV, 136 meV, 157 meV, 178 meV, 293 meV, respectively. The higher and progressively increased φ_{c} values in LED B can constructively confine the electrons in the multi quantum wells (QWs) and effectively resist the electron overflow from the active region, leading to the significantly reduced non-radiative recombination in the *p*-region and enhance hole injection into the active region. However, the formation of the hole depletion region due to the positive polarization sheet charges at the last QB/EBL interface lessens the hole injection efficiency in LED A [45,46] and is shown in the right side inset figure of Figure 5.2(a). This problem can be overcome by removing the EBL from LED A. Illustrated in Figure 5.2(b), the integration of 2 nm intrinsic $\mathrm{Al_{0.66}Ga_{0.34}N}$ strip ($\mathrm{S_6}$) in the middle of last QB of LED B that supports the formation of hole accumulation region due to negative polarization sheet charges at $\mathrm{S_6}$/last QB interface which also enhances the hole injection into the active region. At this interface, the holes move forward due to the intraband tunneling and thermionic emission then injected into the active region [45]. Therefore, an efficient electron blocking capability with a higher hole injection capacity of the proposed EBL-free LED B is expected to exhibit better carrier confinement in the active region and leads to superior performance.

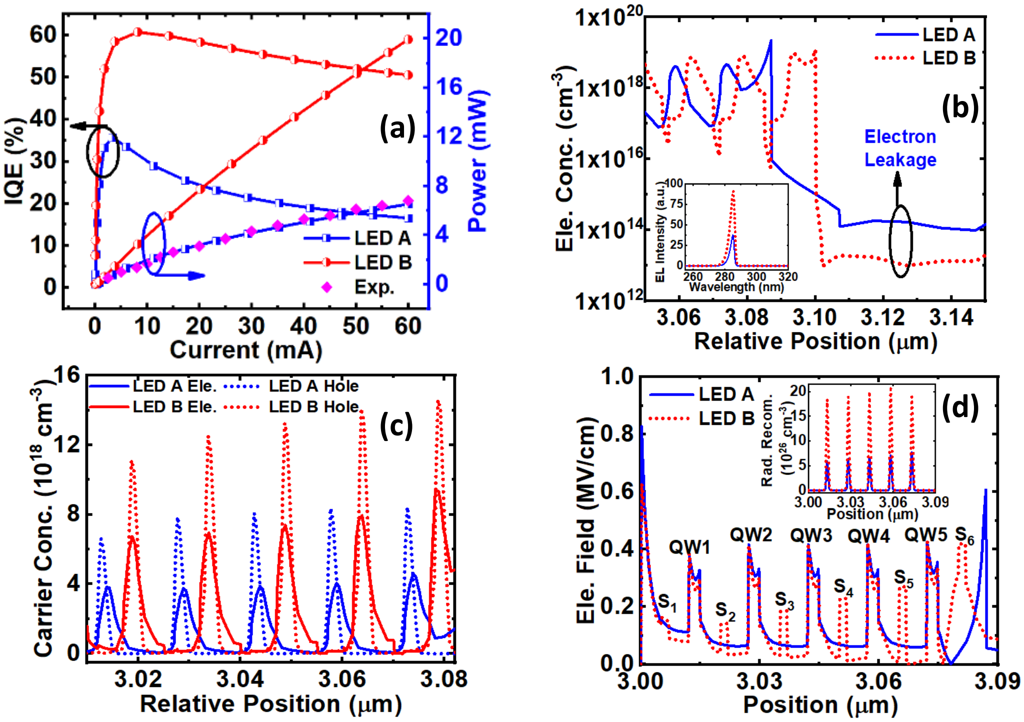

Figure 5.3 Calculated (a) IQE-output power as a function of current injection, measured power of LED A (magenta diamond curve) [1], (b) Electron concentration in the last two QWs and *p*-region, EL intensity (inset figure), (c) Carrier concentration in multiple QWs, and (d) Magnitude of electrostatic field and radiative recombination rate (inset figure) in multiple QWs of LED A and B.

5.4 Results and Discussion

The output characteristics such as IQE and output power as a function of current injection for LED A and LED B are shown in Figure 5.3(a). The calculated maximum IQEs for LED A and LED B are 35.69% and 60.71%, respectively. Moreover, the IQE droop of LED B was significantly reduced to 16.8% from 53.7% (LED A). Also, at 60 mA current injection, the output power of LED B was remarkably increased by $\sim$ 203% to 19.93 mW from 6.56 mW (LED A). As shown in Figure 5.3(a), the calculated output power of LED A closely matches with reference experimental reports (magenta diamond curve) [1], which could validate our device model and parameters used in this study. Further, the electron leakage profile into the *p*-region was calculated to understand the reason behind this tremendous performance improvement in LED B. Figure 5.3(b) shows the electron concentration profile in the last two QWs and *p*-region for LED A and B. The electron leakage in LED B was notably mitigated which is $\sim$ 10.5 times lower than LED A. This prevents the undesired recombination of electrons with incoming holes in the *p*-region, increasing hole injection into the active region.

As a result, in comparison with LED A, as presented in Figure 5.3(c), LED B has boosted electron and hole concentration throughout the active region. It is important to mention that carrier concentrations in LED A and LED B are different from the doping concentrations due to the dependency on the activation energy. The electron concentration in n-Al$_{0.6}$Ga$_{0.4}$N layer is 2.1×10^{18} cm^{-3} for both LEDs. The hole concentration in EBL, cladding, and contact layers for LED A is 2.01×10^{16} cm^{-3}, 7.84×10^{17} cm^{-3}, and 3.77×10^{18} cm^{-3}. The corresponding hole concentration for LED B is 5.46×10^{16} cm^{-3} and 4.1×10^{18} cm^{-3}. Also, the electrostatic fields in multiple QWs of both LEDs are provided in Figure 5.3(d) and these values are lower in LED B compared to LED A supporting the spatial overlap of electron-hole wavefunctions which improves the radiative recombination process [145]. Due to this, the radiative

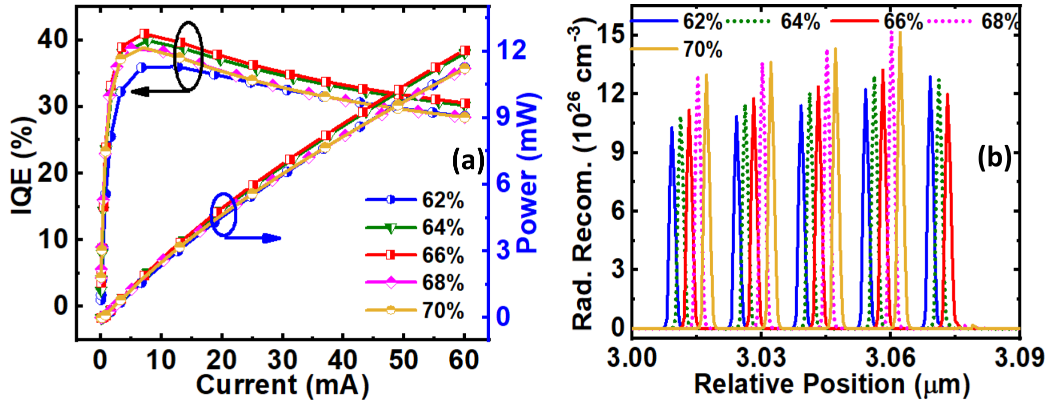

Figure 5.4 Calculated (a) IQE-output power as a function of current injection, and (b) Radiative recombination rate in multiple QWs of LED A without EBL, with different Al compositions of the strip in the last QB (S_6).

recombination rate of LED B is increased by $\sim 200\%$ compared to LED A, as shown in the inset figure of Figure 5.3(d). Therefore, LED B reports higher EL intensity at $\sim$ 284.5 nm under 60 mA current injection and is presented in the inset Figure 5.3(b).

Next, the complete design approach of our proposed strip-in-a-barrier device i.e., LED B is explained. As an initial step, the S_6 composition was engineered as S_6 has a critical role in preventing electron overflow and enhancing the hole injection into the active region by forming the hole accumulation region at S_6/last QB interface. To optimize the S6 composition, we have considered LED A by removing EBL and integrated 2 nm undoped $Al_xGa_{1-x}N$ strip in the middle of the last QB then analyzed the performance of the strip by varying Al profile (X) from 0.61 to 0.70 with 0.01 increment. For a better view, data is shown for x = 0.62, 0.64, 0.66, 0.68, and 0.70. It is worthwhile to mention that increasing Al composition in the strip increases the effective conduction band barrier height (φ_c) that effectively blocks the electrons and mitigates the overflow into the *p*-region. However, a higher Al composition strip may also be responsible for severe band bending due to the generation of a

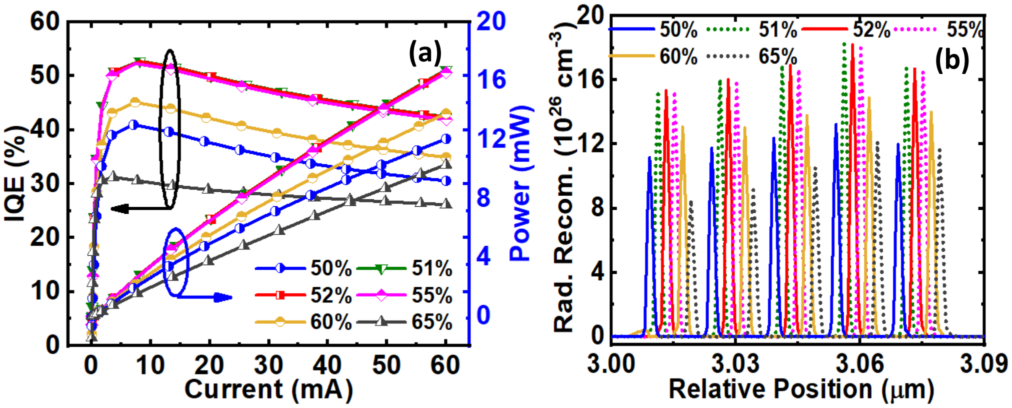

Figure 5.5 Calculated (a) IQE-output power as a function of current injection, and (b) Radiative recombination rate in multiple QWs of LED A without EBL, with optimized S_6, with different Al compositions of strip in the QB1 (S_1).

stronger local electric field and higher lattice mismatch over there. This leads to separate electron and hole wave functions in the corresponding QW and minimizes the radiative recombination there.

Figure 5.4(a) provides the information of IQE-output power as a function of current injection for x=0.62, 0.64, 0.66, 0.68, and 0.70 in S_6. The IQE and power are increased for LEDs with the Al contents varying from x = 0.62 to 0.66, recorded maximum at 0.66 and reduces with further increment in x. Obviously, $Al_{0.66}Ga_{0.34}N$ is a good fit for S_6 which can well tradeoff between electron overflow and band bending. Contrarily, S_6 with x=0.68 and 0.70, can block electrons effectively, but severe band bending at S_6 causes almost negligible radiative recombination in the last QW as shown in Figure 5.4(b). Overall, compared to any other LED with different AlGaN strip in the last QB, LED with $Al_{0.66}Ga_{0.34}N$ strip has higher IQE-output power with uniform radiative recombination in all QWs. Therefore, we consider $Al_{0.66}Ga_{0.34}N$ is the optimal strip composition for S_6.

Without compromising hole injection into the active region and minimizing the electron overflow from the active region, a 2 nm undoped $Al_yGa_{1-y}N$ strip (S_1) was proposed to insert in the middle of the QB_1 which is before first QW. The S_1 is expected to help cool down hot electrons before injecting them into multiple QWs and controls overall electron transportation into active regions, therefore, minimizing the electron overflow, similar to our earlier report [146]. The formation of an E.R. at n-$Al_{0.6}Ga_{0.4}N$/first QB interface in LED A could slow down the electrons which can be seen from the left inset figure of Figure 5.2(a). The integration of S_1 (y=0.51) in the first QB enhances the electron blocking capability further in E.R. which is desirable and can be seen from the left inset figure of Figure 5.2(b). Besides, higher Al profile (y) strips can generate a strong local electrical field at the interface that adversely affects the entire active region. As a result, radiative recombination in each QW is reduced which leads to lower IQE and output power. To decide the best y value for S_1, LED A was considered but without EBL and integrated 2 nm undoped $Al_{0.66}Ga_{0.34}N$ strip (S_6) and analyzed the device performance by varying y from 0.5 to 0.65 with 0.01 increment in S_1.

The IQE-output power as a function of current injection for y = 0.50, 0.51, 0.52, 0.55, 0.60, and 0.65 in S_1 (For a better view, data is shown for only y = 0.50, 0.51, 0.52, 0.55, 0.60, and 0.65.) are shown Figure 5.5(a). As depicted in Figure 5.5(a), the maximum IQE was increased to 52.77% (y=0.51) from 40.97% (y=0.50, i.e., no strip case) which is a 28.8% increment. Moreover, IQE droop was reduced to 19.55% from 25.38% and the output power was boosted to 16.76 mW from 12.06 mW which is a 38.97% improvement. The performance of LED is almost similar and slightly less up to y=0.55 of S_1. For higher y values i.e., 0.6 and 0.65, the related performance started decreasing due to the generation of stronger electric fields. This leads to separate electron and hole wavefunctions in QWs, lessens the radiative recombination as shown in Figure 5.5(b) and is responsible for lower IQE-output power as presented in Figure 5.5(a). Altogether, $Al_{0.51}Ga_{0.49}N$ strip is the optimal design for S1 which significantly improved the LED performance.

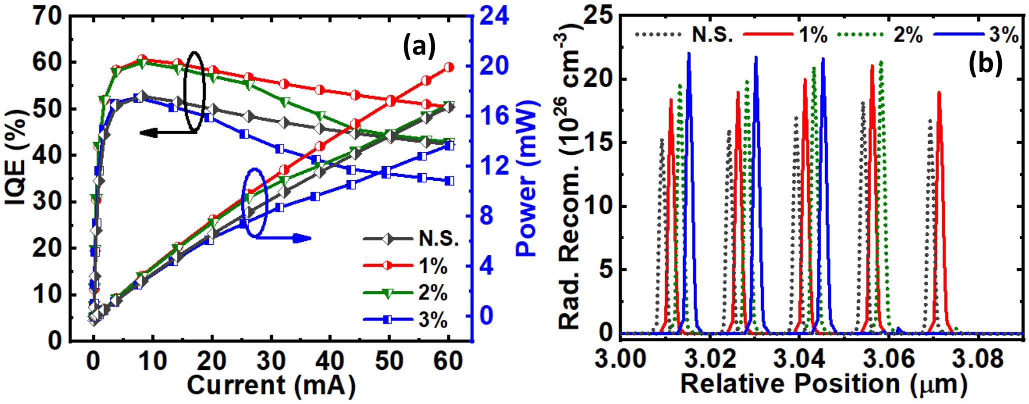

Figure 5.6 Calculated (a) IQE-output power as a function of current injection, and (b) Radiative recombination rate in multiple QWs of LED A without EBL, with optimized S_1 and S_6, with different Al incremental in S_2-S_5.

To achieve the maximum device performance, the remaining strips i.e., S_2-S_5 in the proposed LED were also studied carefully. For this analysis, LED A was considered without EBL, with optimized S_1 and S_6 (best structure from Figure 5.5) and inserted 2 nm undoped Al incremental $Al_zGa_{1-z}N$ strips ($S_2 - S_5$) in $QB_2 - QB_5$. These $S_2 - S_5$ strips help not only to progressively block the electrons in the active region along with S_1 and S_6 but also enhance carrier injection into the active region. Illustrated in Figure 5.6(a), LED with 1% Al incremental strips from S_1 (i.e., S_2-S_5: 0.52, 0.53, 0.54, 0.55; S_1: 0.51 and S_6: 0.66) which is LED B exhibits the best IQE and highest output power. The maximum IQE was reached to 60.71% (1% Al incremental strips) from 52.77% (N.S. i.e., no $S_2 - S_5$ which is the best case from Figure 5.5); IQE droop was reduced to 16.8% from 19.55% and output power was amplified to 19.93 mW from 16.76 mW.

In contrast, IQE and output power of these types of LEDs worsen with increasing Al incremental strips i.e., 2% Al incremental strips and 3% Al incremental strips which is due to almost negligible radiative recombination in the last QW for 2% Al incremental strips LED and absence of radiative recombination in the last

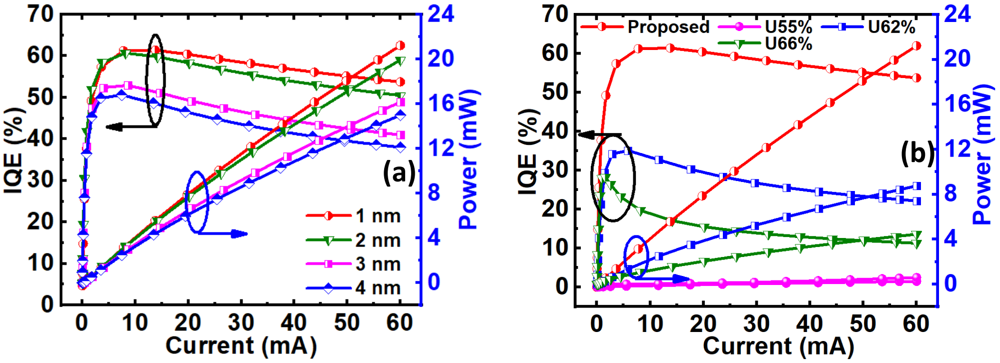

Figure 5.7 Calculated IQE-output power as a function as of current injection for (a) LED B with different strip thickness, and (b) LED A without EBL, with 1 nm uniform strips and proposed LED (LED B with 1 nm strips).

two QWs for 3% Al incremental strips LED, can be seen from Figure 5.6(b). As shown in Figure 5.6(b), the enhanced carrier injection into the active region for 1% Al incremental strips LED improved the radiative recombination proportionately compared to no S_2-S_5 LED (i.e., the best case from Figure 5.5) and is the evidence for high IQE-output power. Therefore, removing the EBL from LED A and integrating 2 nm undoped $Al_xGa_{1-x}N$ strips (S_1-S_6) with x = 0.51, 0.52, 0.53, 0.54, 0.55, and 0.66 (considered as LED B), would be the best candidate to achieve higher performance.

Next, the dependency of the strips' thickness on LED B performance is investigated. Illustrated in Figure 5.7(a), the IQE and output power of LED B were boosted with decreasing strip thickness to 1 nm due to enhancement in the intraband tunneling for holes [45]. Therefore, the hole injection is increased, leading to enhanced IQE and output power. On the other hand, increasing strip thickness to 2 nm, 3 nm, and 4 nm may worsen the hole injection due to the inefficient intraband tunneling for holes which limits IQE and power.

Finally, the performance of the proposed LED is compared to uniform strip-based LEDs. As given in Figure 5.7(b), LEDs with uniform 1 nm strips (example: U55% LED has all $Al_{0.55}Ga_{0.45}N$ strips) were analyzed, and results were compared with the proposed LED. The lowest performance was recorded in U55% LED due to severe electron leakage problems caused by low Al composition strips, whereas U66% LED exhibited low performance due to severe band bending caused by strong local electric fields due to high Al composition strips. However, the better performance among the uniform strip LEDs was reported in U62% LED but the performance is not comparable to the proposed LED. Therefore, LED B with 1 nm thickness strips is the optimal choice which exhibits 61.5% maximum IQE ($\sim$ 70% higher than LED A), 12.4% IQE droop ($\sim$ 333% lower than LED A), 21.23 mW power ($\sim$ 225% more than LED A), lower electron leakage ($\sim$ 11% times less than LED A), and higher radiative recombination ($\sim$ 220% more than LED A) under 60 mA current injection.

5.5 Conclusion

In this chapter, the impact of conventional *p*-EBL on AlGaN deep UV LEDs was explored. Furthermore, the *p*-EBL free strip-in-a-barrier LED structure was successfully demonstrated and suggested by systematically band engineering the strips in all QBs, which can effectively suppress electron overflow and support enhanced hole injection into the LED active region compared to conventional LED. There was a considerable improvement in radiative recombination, IQE, and output power over traditional LED. The proposed EBL-free AlGaN strip-in-a-barrier LED offers a lot of potential for making high-power UV light emitters for practical applications.

Table 5.1 Effect of Lattice Non-ideality on the Magnitude of Spontaneous Polarization in III-nitrides

Paramater	**Symbol (unit)**	**GaN**	**AlN**
Lattice constant at 300 K	a_0 (A^0)	3.189	3.112
Lattice constant at 300 K	c_0 (A^0)	5.185	4.982
Crystal-filed split energy	Δ_{cr} (meV)	10	-169
Spin-orbit split energy	Δ_{so} (meV)	17	19
Electron effective mass (c-axis)	$\mathrm{m}_e^c/\mathrm{m}_o$	0.2	0.32
Electron effective mass (transverse)	$\mathrm{m}_e^t/\mathrm{m}_o$	0.2	0.28
Hole effective mass	A_1	-7.21	-3.86
	A_2	-0.44	-0.25
	A_3	6.68	3.58
	A_4	-3.46	-1.32
	A_5	-3.4	-1.47
	A_6	-4.49	-3.4
Elastic stiffness constant	c_{11} (Gpa)	390	396
	c_{12} (Gpa)	145	137
	c_{13} (Gpa)	106	108
	c_{33} (Gpa)	398	373
	c_{44} (Gpa)	105	116
Shear deformation potential	D_1 (eV)	-3.7	-17.1
	D_2 (eV)	4.5	7.9
	D_3 (eV)	8.2	8.8
	D_4 (eV)	-4.1	-3.9
	D_5 (eV)	-4	-3.4
	D_6 (eV)	-5.5	-3.4
Mg-activation energy	(meV)	170	510
Piezo-electric constants	e_{31} (C/m^2)	-0.49	-0.6
	e_{33} (C/m^2)	0.73	1.46
Si-activation energy	(meV)	15	250
Hydrostatic deformation potential (c-axis)	a_z (eV)	-4.9	-3.4
Hydrostatic deformation potential (transverse)	a_t (eV)	-11.3	-11.8

CHAPTER 6

POLARIZATION ENGINEERED ELECTRON BLOCKING LAYER-FREE ALGAN DEEP ULTRAVIOLET LIGHT-EMITTING DIODES

Presented in Chapters 4 and 5, severe electron leakage from the active region is one of the critical challenges in AlGaN deep ultraviolet (UV) light-emitting diodes (LEDs). In this regard, *p*-type AlGaN electron blocking layer (EBL) has been utilized to mitigate the electron leakage. However, it has an impact on hole injection because of the formation of positive polarization sheet charges at the hetero-interface of the EBL and last quantum barrier (QB). This problem has been addressed in this chapter by engineering the formation of polarization charges with the integration of graded QBs instead of regular QBs in AlGaN deep UV LED without the requirement of any *p*-AlGaN EBL.

6.1 Device Structure and Parameters

Three LED device structures were designed, and their performances were evaluated in this study. A conventional AlGaN deep UV LED structure (LED 1) with an emission wavelength of 284 nm is used as a reference structure. As shown in Figure 6.1(a), LED 1 has a 3 μm n-$Al_{0.6}Ga_{0.4}N$ (Si: $5\times10^{-18}cm^3/s$) template layer, an active region made up of five intrinsic 3 nm $Al_{0.4}Ga_{0.6}N$ quantum wells (QWs) sandwiched between six intrinsic 12-nm-thick $Al_{0.5}Ga_{0.5}N$ QBs, a 20 nm p-$Al_{0.65}Ga_{0.35}N$ (Mg: $2\times10^{-19}cm^3/s$) EBL, a 50 nm p-$Al_{0.5}Ga_{0.5}N$ (Mg: $2\times10^{-19}cm^3/s$) hole injection layer, and a 120 nm p-GaN (Mg: $1\times10^{-20}cm^3/s$) contact layer. In addition, the Al composition (%) profile information for LED 1 is displayed in Figure 6.1(b). LED 2 was then built from LED 1 by removing the EBL and replacing it with QBs with a greater Al content. The Al content in each QB is 51%, 54%, 57%, 60%, and 75%, respectively, as shown

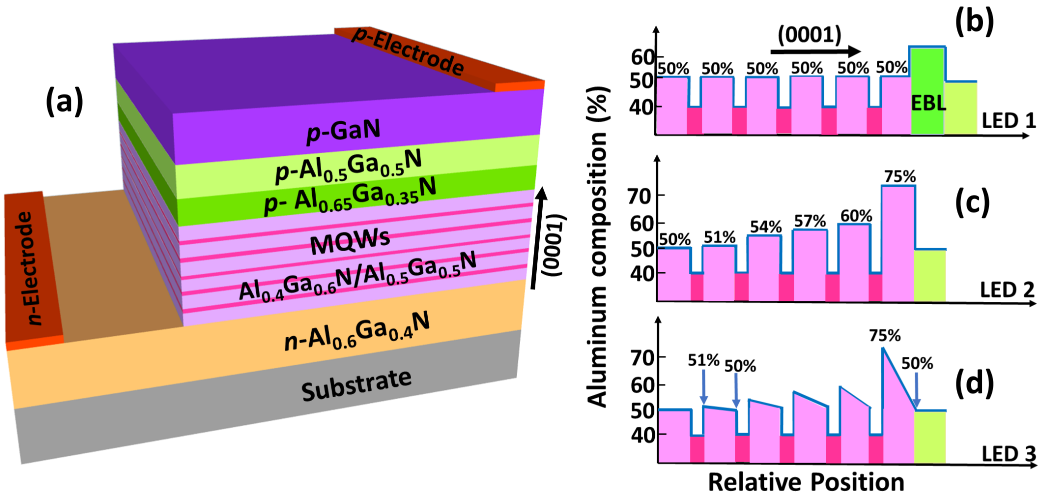

Figure 6.1 (a) Schematic diagram of LED 1, Al composition (%) profile related to the conduction band of (b) LED 1, (c) LED 2, and (d) LED 3.

in Figure 6.1(c). Finally, the proposed structure (LED 3) illustrated in Figure 6.1(d) is similar to LED 2 with the exception of the QBs, which were linearly graded from 51%, 54%, 57%, 60%, and 75% to 50%. The chip area of all LEDs is 400 × 400 μm^2. The information related to the device model and parameters can be found in Chapters 4 and 5.

6.2 Results and Discussion

As shown in Figure 6.2, the energy-band diagrams at an injection current of 60 mA are estimated in order to comprehend the performance of the three deep UV LED designs. First, the effective conduction band barrier heights (CBBHs), which are the maximum difference between the conduction band energy level and its quasi-Fermi level, are indicated as ϕ_{en} and ϕ_{EBL}, respectively. The estimated values are presented in Table 6.1 based on the energy-band diagrams. 235 meV is the ϕ_{EBL} required to inhibit the electron overflow in a conventional LED. This value is quite low compared to the QB heights (ϕ_{e6}) of LED 2 and LED 3 without EBL. Due to the steady rise in Al-compositions of QBs, the ϕ_{en} values of both LED 2 and LED 3 increase with each

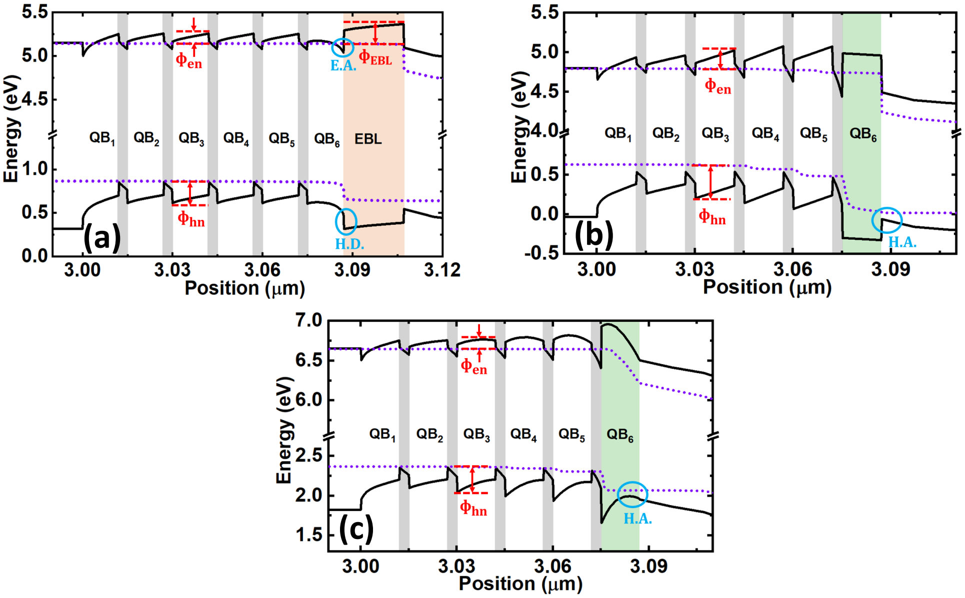

Figure 6.2 Estimated energy-band diagrams of (a) LED 1, (b) LED 2, and (c) LED 3 at an injection current of 60 mA. E.A. is the electron accumulation region in the conduction band, H.D. is the hole depletion region, and H. A. is the hole accumulation region in the valence band.

QB, effectively preventing the electrons from jumping out of the QWs. In addition, as compared to LED 3, the ϕ_{en} values of LED 2 are considerably high because of the constant barrier compositions. It should assist in improving electron confinement in the active region in general. But in LED 2, a very big lattice mismatch between the QBs and QWs causes higher electric fields in the active region. This affects the carrier confinement held in place and is explained in more detail. Further, ϕ_{e6} of LED 3 is higher than ϕ_{EBL} of LED 1 and ϕ_{e6} of LED 2. Consequently, it is anticipated that LED 3 will significantly reduce electron leakage from the active region.

Second, it's important to note, as shown in Figure 6.2(a), that positive polarization sheet charges cause a sharp bend in the conduction band at the point where the EBL and the last QB of LED 1 meet. This area accumulates a significant amount of electrons, 3.66×10^{16} cm^{-3}, which ultimately leads to nonradiative recombination [147]. As observed in Figure 6.2(a), the same positive polarization sheet charges in the valence band of LED 1 also cause the formation of a hole

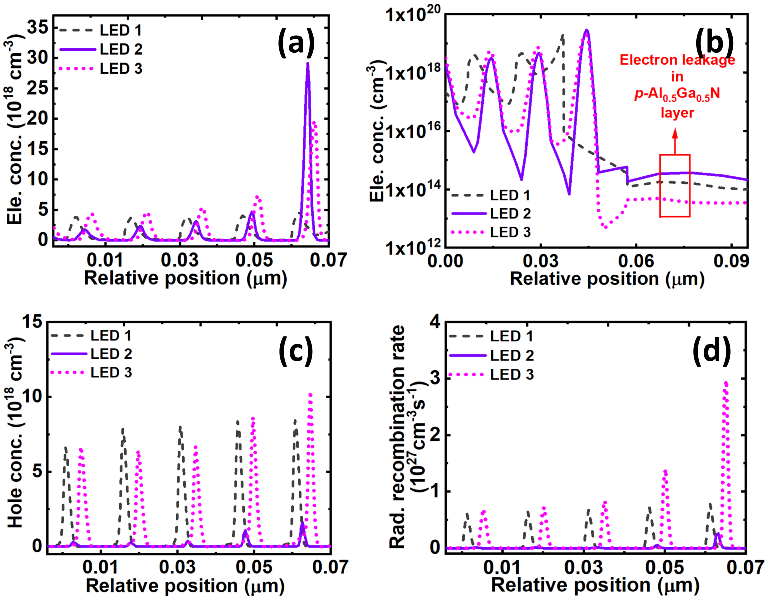

Figure 6.3 Calculated (a) Electron concentration, (b) Electron leakage, (c) Hole concentration, and (d) Radiative recombination of LED 1, LED 2, and LED 3.

depletion region at the hetero-interface of the EBL and the last QB. This has a significant impact on the efficiency of hole injection into the active region [46]. In the case of LED 2 and LED 3, removing the EBL eliminates the previously noted issue. In addition, as demonstrated in Figures 6.2(b) and 6.2(c), EBL-free LED designs promote the creation of negative sheet polarization charges at the interface of p-Al$_{0.5}$Ga$_{0.5}$N and the last QB, which increases the hole injection efficiency.

Last, ϕ_{hn} is the effective valence band barrier heights (VBBHs), which are defined as the highest difference between the valence band energy level and its quasi-Fermi level for holes at the corresponding QB (n). The determined equivalent values are presented in Table 6.2. The values of ϕ_{hn} are observed to be greater in LEDs 2 and 3 compared to LED 1 because of an increase in the Al content in the QBs. This contributes to enhancing the concentration and confinement of holes in the active region. Additionally, a very high ϕ_{hn} might impact the hole transport in the active region, which is the case with LED 2. LED 3 has lower ϕ_{hn} values than LED 2 owing to the graded composition of the QBs. Overall, it is predicted that the

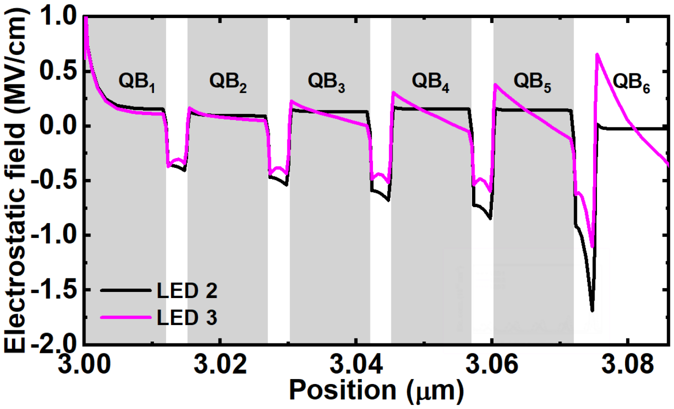

Figure 6.4 The electrostatic field in the active region of LED 2 and LED 3.

suggested structure, LED 3, would exhibit more efficient hole transport in the active region than other LEDs.

The electron concentration, electron leakage, hole concentration, and radiative recombination of the three LED configurations at an injection current of 60 mA are presented in Figure 6.3. For better viewing, the location on X-axis is slightly moved for LEDs. As predicted, in comparison with other LEDs, LED 3 demonstrates a considerably enhanced electron concentration in the active area, as shown in Figure 6.3(a). In addition, it is escalating as a result of particularly designed QBs. Due to the efficient confinement of electrons in LED 3, electron leakage into the *p*-region is drastically decreased compared to the other two LEDs, as depicted in Figure 6.3(b). Due to the inadequate confinement of electrons in the active region of LED 2, it is also noted that LED 2 has an even worse electron leakage than LED 1. This would enhance nonradiative recombination in the *p*-region of LED 2 and diminish the efficiency of hole injection. Although there is a creation of negative sheet polarization charges at the interface of p-$\mathrm{Al}_{0.5}\mathrm{Ga}_{0.5}\mathrm{N}$/last QB, hole injection efficiency into the active region is greatly impaired owing to severe electron leakage in LED 2. Because of the decreased electron leakage in LED 3, the chance of non-radiative recombination

Table 6.1 Effective Conduction Band Barrier Heights of QBs (ϕ_{en}) and EBL (ϕ_{EBL}) for LED 1, LED 2, and LED 3

CBBH	LED 1 (meV)	LED 2 (meV)	LED 3 (meV)
ϕ_{e1}	107.5	142.9	107.2
ϕ_{e2}	114.3	167.3	109.9
ϕ_{e3}	113.8	232.6	120
ϕ_{e4}	112.6	300.6	149.2
ϕ_{e5}	110.1	330.1	175.2
ϕ_{e6}	31.2	242.2	314.7
ϕ_{EBL}	235	-	-

Table 6.2 Effective Valence Band Barrier Heights of QBs (ϕ_{hn}) for LED 1, LED 2 and LED 3

VBBH	LED 1 (meV)	LED 2 (meV)	LED 3 (meV)
ϕ_{h2}	251.9	367.1	270.8
ϕ_{h3}	250.3	427.1	321.7
ϕ_{h4}	249.3	471.4	367.2
ϕ_{h5}	248.1	502.1	405.9

of the overflowed electrons with the arriving holes would be lowered in the *p*-region. This would increase the efficiency of hole injection into the active region in LED 3. As a consequence, LED 3 has a higher hole concentration, and LED 2 has the lowest hole concentration in the active region compared to other LEDs, as shown in Figure 6.3(c). As a result of LED 3's better electron and hole concentrations, radiative recombination was considerably boosted, as shown in Figure 6.3(d). Though the last QB of LED 2 can tolerate more electrons due to strong band bending, but it failed to confine the holes; as a consequence, it shows insufficient radiative recombination.

To further comprehend the physical mechanism behind the increased carrier confinement in this proposed graded QB structure, the net polarization charge density and electrostatic field in the active region are calculated. The electrostatic field in the active region can be estimated using the following Equations (6.1) - (6.3) [148]

$$E_{\mathrm{QB}} \approx \frac{l_{\mathrm{QW}} \cdot \Delta P(z)}{l_{\mathrm{QW}} \cdot \varepsilon_{\mathrm{QB}} + l_{\mathrm{QB}} \cdot \varepsilon_{\mathrm{QW}}} \tag{6.1}$$

$$E_{\mathrm{QB}} \cdot l_{\mathrm{QB}} = E_{\mathrm{QW}} \cdot l_{\mathrm{QW}} \tag{6.2}$$

$$\Delta P(z) = \sigma_{\mathrm{S}}^{\mathrm{pol}} - \rho_{\mathrm{B}}^{\mathrm{pol}} \cdot z \tag{6.3}$$

Where E_{QB} and E_{QW} represent the electrostatic field in the QB and QW respectively. $\Delta P(z)$ denotes the charge density of net polarization; z is the point along the growth direction. $\varepsilon_{\mathrm{QB}}$ and $\varepsilon_{\mathrm{QW}}$ respectively reflect the dielectric constants of QB and QW. l_{QW} and l_{QB} are the QW and QB thicknesses, respectively. $\sigma_{\mathrm{S}}^{\mathrm{pol}}$ is the polarization-induced sheet charge density at the interface between QB and QW, and $\rho_{\mathrm{B}}^{\mathrm{pol}}$ is the polarization-induced bulk charge density in QB. It is preferable to have a reduced electrostatic field in the QW area in order to properly confine electrons and holes [15]. According to Equation (6.2), decreasing the value of E_{QB} may likewise decrease the value of E_{QW}. In addition, as shown by Equation (6.1), E_{QB} may be decreased by reducing the value of $\Delta P(z)$. However, $\Delta P(z)$ is connected to $\sigma_{\mathrm{S}}^{\mathrm{pol}}$ and $\rho_{\mathrm{B}}^{\mathrm{pol}}$, as shown by Equation (6.3). Therefore, these characteristics are determined as follows for LED 2 and LED 3. The polarization-induced sheet charge density in $1/\mathrm{m}^2$ at the QB/QW interface is characterized as a function of spontaneous P_{SP} and piezoelectric polarizations, P_{PP} [149], respectively.

$$\sigma_{\mathrm{S}}^{\mathrm{pol}} = \{P_{\mathrm{SP}}(\mathrm{QB}) - [P_{\mathrm{SP}}(\mathrm{QW}) + P_{\mathrm{PP}}(\mathrm{QW})]\} \times 6.242 \times 10^{18}, \tag{6.4}$$

The P_{SP} and P_{PP} in $\mathrm{C/m}^2$ can be written as [139]

$$P_{\mathrm{SP}}\left(\mathrm{Al_xGa_{1-x}N}\right) = -0.09x - 0.034(1-x) + 0.019x(1-x), \tag{6.5}$$

Table 6.3 Calculated $\sigma_{\mathrm{S}}^{\mathrm{pol}}$ at the QB/QW Interface, (1/m^2) and $\sigma_{\mathrm{B}}^{\mathrm{pol}}$ in the QBs, (1/m^3) of LED 2 and LED 3

	$\sigma_{\mathrm{S}}^{\mathrm{pol}}$ QB2/QW2	$\sigma_{\mathrm{B}}^{\mathrm{pol}}$ QB2	$\sigma_{\mathrm{S}}^{\mathrm{pol}}$ QB3/QW3	$\sigma_{\mathrm{B}}^{\mathrm{pol}}$ QB3	$\sigma_{\mathrm{S}}^{\mathrm{pol}}$ QB4/QW4	$\sigma_{\mathrm{B}}^{\mathrm{pol}}$ QB4	$\sigma_{\mathrm{S}}^{\mathrm{pol}}$ QB5/QW5	$\sigma_{\mathrm{B}}^{\mathrm{pol}}$ QB5
LED2	2.948×10^{16}	0	3.783×10^{16}	0	4.631×10^{16}	0	5.493×10^{16}	0
LED3	2.672×10^{16}	2.348×10^{23}	2.672×10^{16}	9.468×10^{23}	2.672×10^{16}	1.67×10^{24}	2.672×10^{16}	2.404×10^{24}

$$P_{\mathrm{PP}}\left(\mathrm{Al_xGa_{1-x}N}\right) = x \cdot P_{\mathrm{PP}}(\mathrm{AlN}) \cdot s + (1-x) \cdot P_{PP}(\mathrm{GaN}) \cdot s \tag{6.6}$$

where,

$$P_{\mathrm{PP}}(\mathrm{AlN}) = -1.808 \cdot s + 5.624 \cdot s^2 \text{ for } s < 0,$$

$$P_{\mathrm{PP}}(\mathrm{AlN}) = -1.808 \cdot s + 7.888 \cdot s^2 \text{ for } s > 0,$$

$$P_{\mathrm{PP}}(\mathrm{GaN}) = -0.918 \cdot s + 9.541 \cdot s^2,$$

$$\text{Basal strain } (s) = \frac{\mathrm{QB}_{\text{lattice constant}} - \mathrm{QW}_{\text{lattice constant}}}{\mathrm{QW}_{\text{lattice constant}}}$$

The values of the lattice constant can be found elsewhere [149]. Also, the polarization-induced bulk charge density(1/m^2) in the QB can be derived as [150].

$$\rho_{\mathrm{B}}^{\mathrm{pol}} = \frac{\left[P_{\mathrm{sp}}\left(\mathrm{Al}_y\mathrm{Ga}_{1-y}\ \mathrm{N}\right) + P_{\mathrm{pp}}\left(\mathrm{Al}_y\mathrm{Ga}_{1-y}\ \mathrm{N}\right)\right] - P_{\mathrm{sp}}\left(\mathrm{Al}_x\mathrm{Ga}_{1-\mathrm{x}}\mathrm{N}\right)}{z(y) - z(x)} \times 6.242 \times 10^{18} \tag{6.7}$$

Here, the QB is graded from $\mathrm{Al}_x\mathrm{Ga}_{1-x}\mathrm{N}$ to $\mathrm{Al}_y\mathrm{Ga}_{1-y}\mathrm{N}$, and $(z(y) - z(x))$ is the grading distance. Finally, the calculated values of $\sigma_{\mathrm{S}}^{\mathrm{pol}}$ and $\rho_{\mathrm{B}}^{\mathrm{pol}}$ for LED 2 and LED 3 are listed in Table 6.3.

Due to the decreased lattice mismatch at the interfaces, the $\sigma_{\mathrm{S}}^{\mathrm{pol}}$ values for LED 3 are much lower than those for LED 2. Moreover, the $\rho_{\mathrm{B}}^{\mathrm{pol}}$ values of the QBs in LED 3 are raised owing to a compositionally graded Al profile. In compared to LED 2, the $\Delta P(z)$ values of LED 3's graded QBs are lowered overall. This results in a decreased

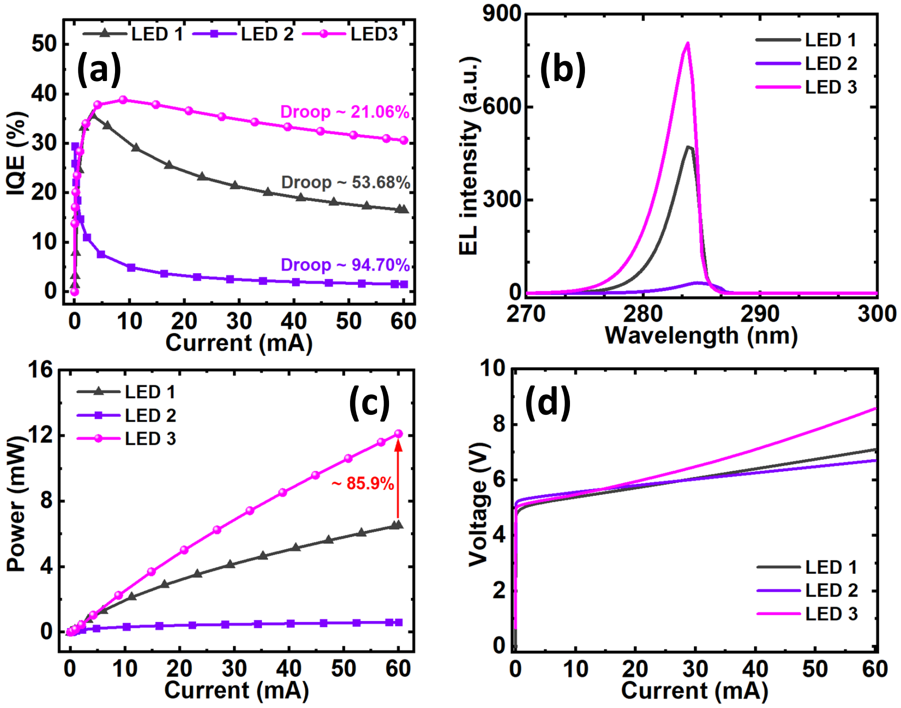

Figure 6.5 Calculated (a) IQE, (b) EL intensity, (c) L-I, and (d) I-V characteristics of LED 1, LED 2, and LED 3.

electrostatic field (E_{QB}) in all QBs. Consequently, it is anticipated that the QWs of LED 3 will exhibit a decreased electrostatic field (E_{QW}). Figure 6.4 depicts the electrostatic field in the active region of LEDs 2 and 3. As expected, multiple QWs of LED 3 display lower electrostatic fields than LED 2, resulting in enhanced carrier confinement.

The IQE, EL intensity, and L-I-V properties of all LEDs are depicted in Figure 6.5. As shown in Figure 6.5(a), the highest computed IQEs for LED 1, LED 2, and LED 3 are 35.69%, 29.45%, and 38.84%, respectively. Under 0-60 mA current injection, the IQE drop is 94.7% owing to an increase in electron leakage in LED 2. LED 3 has a relatively high IQE with an efficiency drop of just 21.06 percent, but LED 1 has an efficiency drop of 53.68%. Such gains in LED 3 are a consequence of the proposed structure's enhanced radiative recombination and decreased electron leakage. Consequently, as shown in Figure 6.5(b), LED 3 has

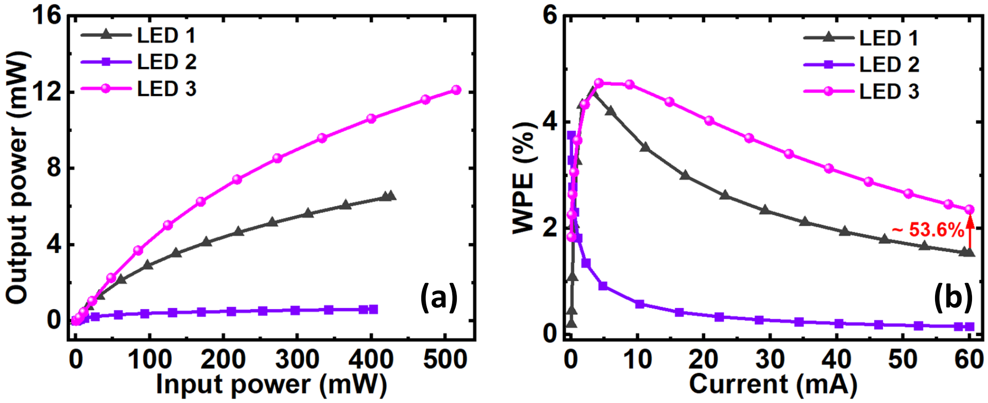

Figure 6.6 Estimated (a) Output power as a function of input power, (b) WPE as a function of current injection of LED 1, LED 2, and LED 3.

Table 6.4 Comparison of IQE and Output Power of LED 1, LED 2, and LED 3

	LED 1	**LED 2**	**LED 3**
Max. IQE (%)	35.69 at 3.26 mA	29.45 at 0.04 mA	38.84 at 8.82 mA
IQE (%) at 60 mA	16.53	1.56	30.66
IQE (%) droop	53.68	94.7	21.06
Power at 60 mA (mW)	6.52	0.61	12.12

the highest electroluminescence (EL) intensity compared to LED 1 and LED 2 at the emission wavelength of 284 nm. As a result, as seen in Figure 6.5(c), LED 3 exhibits a noteworthy increase in output power of 12.12 mW at 60 mA current injection, which is an improvement of 85.9% over the reference structure. Table 6.4 provides a comparison of the different computed IQE and output power parameters for the three LED configurations. As shown in Figure 6.5(d), the turn-on voltage of all three LEDs is nearly same. Due to the presence of graded QBs, LED 3 exhibited a slightly higher operational bias voltage at 60 mA current injection than the other LEDs.

As shown in Figure 6.6(a), the output power of LED 3 is greatly boosted with the same current injection level from the input power source. LEDs may also have varying values for their maximum operational input power supply. This is mostly attributable to the various operating biases, as indicated in Figure 6.5(d). Figure 6.6(b) presents the wall-plug efficiency (WPE) as a function of current injection for all three LEDs. The enhanced output power contributes to the greater WPE of the proposed structure, regardless of the higher operating bias voltage levels. In addition, the WPE of LED 3 is 2.35% at 60 mA, which is an improvement of 53.6% over the reference structure, LED 1.

6.3 Conclusion

In this chapter, *p*-EBL free AlGaN deep UV LEDs with linearly graded QBs emitting at 284 nm wavelength are deeply investigated. Due to the specially engineered polarization in the proposed AlGaN deep UV LED active region, the findings indicate that integrated the proposed QBs is helpful for generating higher output optical power and WPE. The elimination of the growing p-heavily doped high Al composition AlGaN layers such as EBLs for deep UV LEDs, which reduces the device resistance, is an additional key advantage of EBL-free structures from an epitaxial growth standpoint. Therefore, the reported structure is highly capable of producing UV LEDs with good performance for practical applications.

CHAPTER 7

HIGH PERFORMANCE INGAN BLUE LIGHT-EMITTING DIODES WITH CONTROLLED POSITIVE SHEET POLARIZATION

Light-emitting diodes (LEDs) made from III-nitride material have been found in several applications, such as energy-efficient solid-state lighting, backlight in liquid crystal displays, micro-displays, food processing, and many more. Even though InGaN/GaN-based blue LEDs are more efficient than LEDs with longer emission wavelengths, they are still suffered from a severe efficiency drop at high injection current. The primary causes may be a large number of electrons overflowing out of the active region and inefficient hole injection to the active region. In this context, an electron-blocking layer (EBL), the *p*-type AlGaN layer has been integrated right after the active region to stop electrons from leaking out. Further, the EBL has been redesigned for more efficient electron blocking and improved hole injection using the graded AlGaN, single side graded AlGaN/GaN superlattice, double side AlGaN/GaN superlattice, lattice-matched AlInN and many others.

It has been found that the EBL can not only stop electrons from leaking out, but also reduce the hole injection into the active region. This is because positive sheet polarization charges form at the last quantum barrier (QB)/EBL interface, which makes it harder for holes to get into the active region. Moreover, it has been known that the majority carrier is likely to be confined and radiatively recombine notably in the last quantum well (QW) which is just before the last QB of III-nitride-based multiple QW LEDs. So, it's important to fix the problems with the last QB/EBL interface, since it has a direct effect on the way the carrier confinement and radiative recombination happen in the entire LED structure. In this regard, the last QB has been made with different structures, such as *p*-GaN [19], *p*-InGaN/GaN SL, and AlGaN/InGaN SL. Further, EBL-free InGaN/GaN LEDs have been reported. However, these complex structures may be challenging for the epitaxial growth of such LED structures.

In this chapter, a novel LED structure with an AlGaN last QB, lattice-matched to the EBL, has been proposed instead of conventional GaN last QB. Because there is a lattice match at the last QB/EBL interface, the proposed LED stops positive sheet charges from being form there. Substantially, this structure supports high effective conduction band (CB) heights for electrons at last QB and EBL; low effective valence band (VB) height for holes at EBL leads to having better electron blocking capability and hole injection, respectively.

7.1 Device Structure Parameters

The conventional InGaN/GaN blue LED, experimentally reported by Kuo et al. as a reference structure, has been used to evaluate the simulation model in this investigation. Further, the conventional structure, LED-I, grown on a c-plane sapphire substrate, followed by a 4.5 μm n-GaN (Si doping: 5×10^{-18} cm^{-3}) layer, an active region consisting of five $In_{0.21}Ga_{0.79}N$ (2 nm) QWs are sandwiched by six GaN (10 nm) QBs, a 20 nm p-$Al_{0.15}Ga_{0.85}N$ (Mg doing: 1.2×10^{18} cm^{-3}) EBL, a 150 nm p-GaN (Mg doing: 3×10^{18} cm^{-3}) layer, and a 20 nm p^{+}-GaN (Mg doing: 1×10^{19} cm^{-3}) contact layer. The proposed structure, LED-II, has a similar structure to LED-I, with the exception of the last QB (QB6), which has $Al_{0.15}Ga_{0.85}N$ instead of GaN. The schematic schematics of the two LEDs are shown in Figure 7.1.

In this study, the device area of 300 × 300 μm^2 is taken into account for both LEDs. In our model, the internal loss is set to 500 m^{-1} and the light extraction efficiency assumed to be 0.78 [23]. The band offset of III-nitride materials systems is taken to into the model as 0.7/0.3 [24]. The operating temperature is considered as 300 K throughout the study. The spontaneous and piezoelectric polarization fields

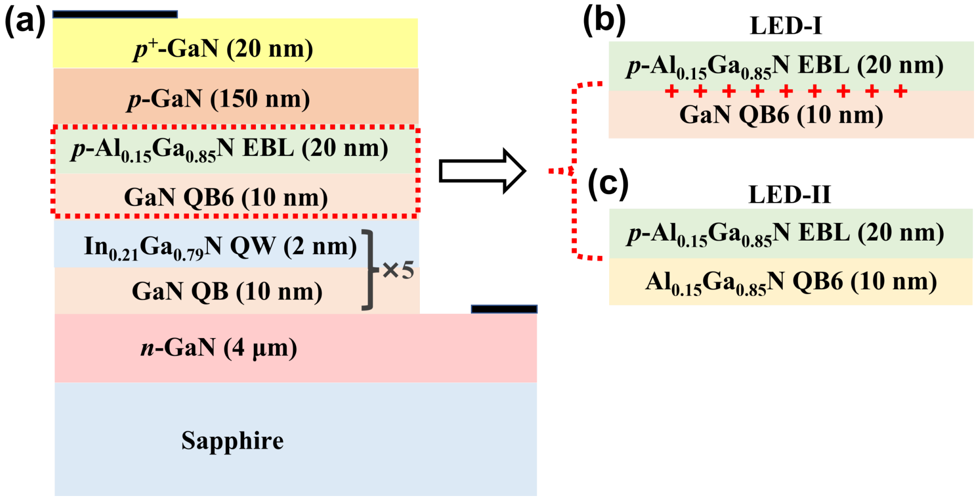

Figure 7.1 Schematic diagram of (a) LED-I, last QB/p-EBL structures of (b) LED-I, and (c) LED-II.

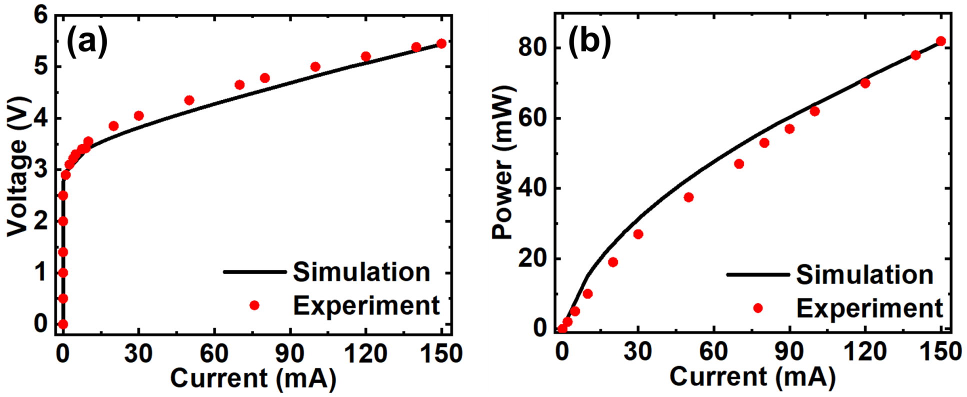

Figure 7.2 Calculated and measured (a) I-V and (b) L-I characteristics of conventional InGaN/GaN blue structure reported in Ref. 23.

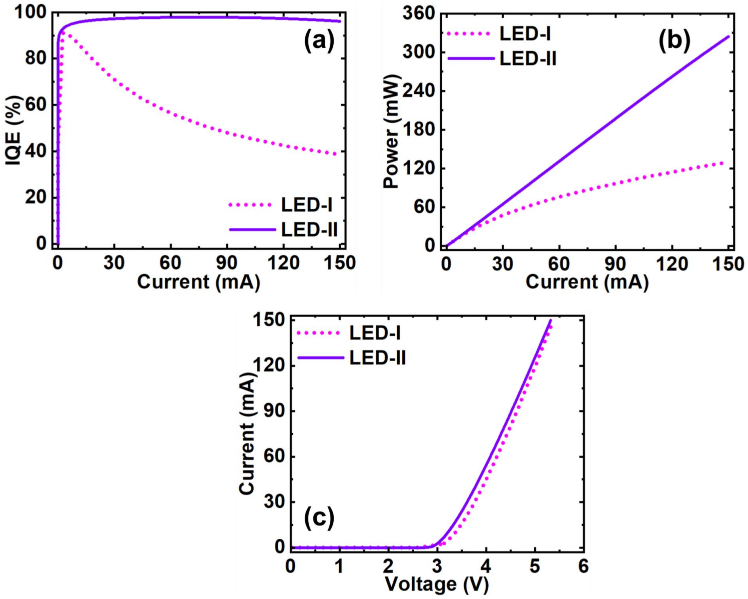

Figure 7.3 Calculated (a) IQE, (b) L-I, and (c) I-V characteristics of LED-I, and LED-II.

are estimated using the methods reported by Fiorentini et al. [25]. The energy-band diagrams of all LED structures are calculated using the 6×6 $k \cdot p$ model [26]. Other material/band parameters of the III-nitride semiconductors used in the simulation model can be found in [27]. First, our device model is validated by simulating the reference structure reported by Kuo et al. [23].The simulated and measured [23] current-voltage (I-V), light output power-current (L-I) characteristics of the reference InGaN/GaN LED structure are presented in Figure 7.2. It's clear to see that the simulated I-V and L-I characteristics are very close to the ones that were measured experimentally. This verifies the correctness of utilized device model and the parameters used in this study.

7.2 Results and Discussion

The precisely modelled IQE, L-I, and I-V properties of LED-I and LED-II are depicted in Figure 7.3. It demonstrates that LED-II has a higher IQE with negligible droop, more output power, and lower turn-on voltage than LED-I. LED-I has an apex IQE

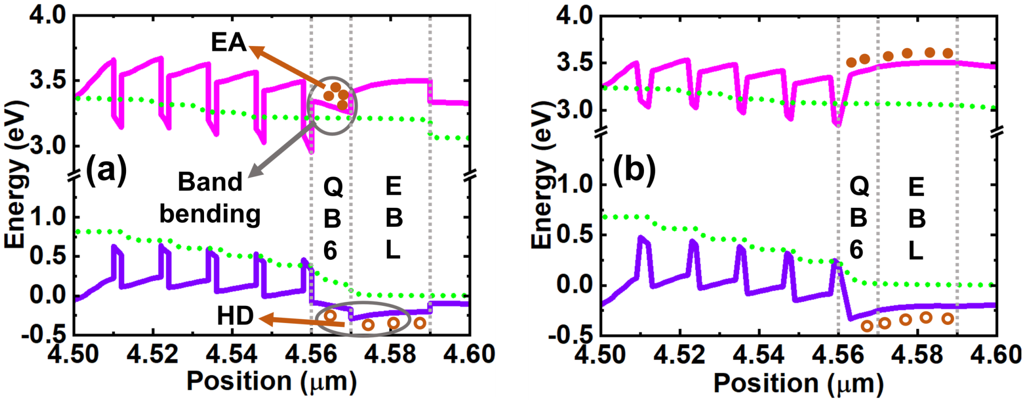

Figure 7.4 Calculated energy-band diagrams of (a) LED-I, and (b) LED-II at 150 mA current injection. Here, solid circles represent the electrons in CB and hollow circles indicate the holes in VB. The electron accumulation region is represented by EA and the hole depletion region is denoted by HD at the QB6/EBL interface of LED-I.

of 91.1% at 3.5 mA, while LED-II reports 95.81% at the same injection current, as shown Figure 7.3(a). However, the IQE of LED-II continues to rise until it reaches a maximum of 97.87% at 73.2 mA. In addition, LED-II has an IQE of 96.11% at 150 mA current injection, which is approximately 2.49 times more than LED-I. Significantly, the IQE drop at an injection current of 150 mA, as defined by (IQE_{max} - $IQE_{150\ mA}$)/IQE_{max} is just 1.79 percent in LED-II, whereas it is calculated to be 57.65 percent in LED-I. It is worthwhile to note that the proposed LED i.e., LED-II exhibits not only a higher IQE but also no obvious IQE droop up to a current injection of 120 mA. This significant improvement of the IQE and negligible IQE droop is achieved due to the integration of $Al_{0.15}Ga_{0.85}N$ last QB which is lattice-matched with the EBL, instead of regular GaN QB6, where the sheet polarization density is 3.03×10^{16} m^{-2} at the QB6/EBL interface in LED-I. As a result, the output power of LED-II was significantly enhanced throughout the entire current injection, as shown Figure 7.3(b). This is estimated as 324.38 mW at 150 mA current injection, which is 2.51 times that of LED-I. In addition, it is important to note that the turn-on voltage of LED-II is

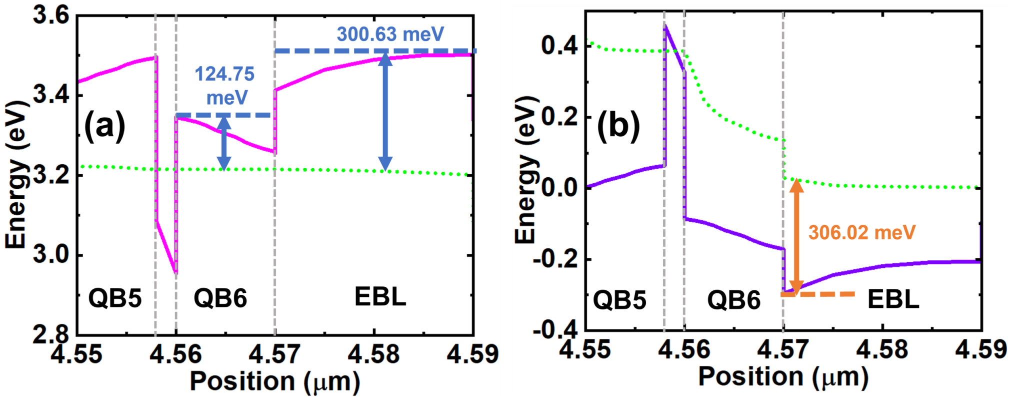

Figure 7.5 Calculated (a) conduction band profile and (b) valence band profile of QB6 and EBL in LED-I at 150 mA current injection.

somewhat lower than that of LED-I, demonstrating the increased carrier injection into the active region of this LED, as seen in Figure 7.3(c). This is due to the negligible positive sheet polarization charges at the last QB/EBL interface.

The E-B diagrams are investigated further to comprehend LED-II performance enhancement processes. Figure 7.4 depicts the predicted E-B diagrams for both LEDs. In the conduction band (CB) of LED-I, the creation of a steep downward band-bending is mostly attributable to the generated positive polarization sheet charges at the QB6/EBL interface. The development of sheet charges at this interface is mostly caused by the higher Al concentration in EBL. Consequently, a high number of electrons accumulate and a hole depletion region forms at the heterointerface, as seen in Figure 7.4(a), which leads to non-radiative recombination and electron overflow [28]. As demonstrated in Figure 7.4(b), the formation of positive sheet charges may be minimized by substituting QB6 with $Al_{0.15}Ga_{0.85}N$ in LED-II.

The enlarged E-B diagrams of QB6 and EBL in LED-I and LED-II are depicted in Figures 7.5 and 7.6, respectively. Due to substantial band-bending, as shown in Figures 7.5(a), the effective potential height for electrons in the CB of QB6 in LED-I is 124.75 meV, which is significantly lower than that of LED-II (390.12 meV,

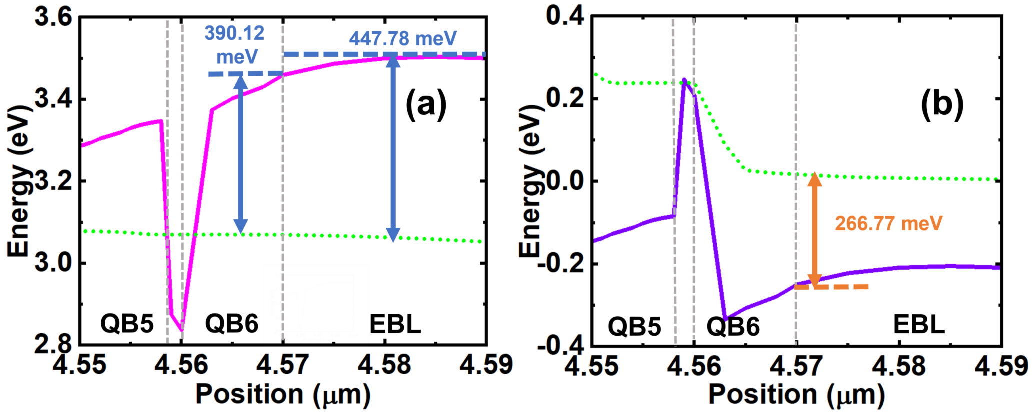

Figure 7.6 Calculated (a) conduction band profile and (b) valence band profile of QB6 and EBL in LED-II at 150 mA current injection.

see from Figure 7.6(a)). The effective potential height for electrons in the CB the maximum difference between the conduction band energy level and its quasi-Fermi level for electrons at the corresponding QB/EBL. These values for EBLs in LED-I and LED-II are 300.63 meV and 447.78 meV respectively. compared to LED-I, the higher values in LED-II have better electron confinement capabilities in the active region due to the requirement of higher energies to overflow the electrons to the *p*-type region in the case of LED-II. Effective potential height for holes in the VB is the maximum difference between the VB energy level and the quasi-Fermi level for holes in the corresponding QB. As shown in Figures 7.5(b) and 7.6(b), the effective potential height for holes in the VB of EBL in LED-II (266.77 meV) is lower than in LED-I (306.02 meV) due to the regulated positive sheet polarization charges effect in the QB6/EBL interface, which promotes smooth hole transport. Therefore, it is anticipated that LED-II would have a larger hole injection capability.

To further validate the superior performance of the proposed LED, we computed the carrier concentration in both LEDs. The overall carrier concentrations in the active regions of both LED designs are depicted in Figure 7.7. As demonstrated in

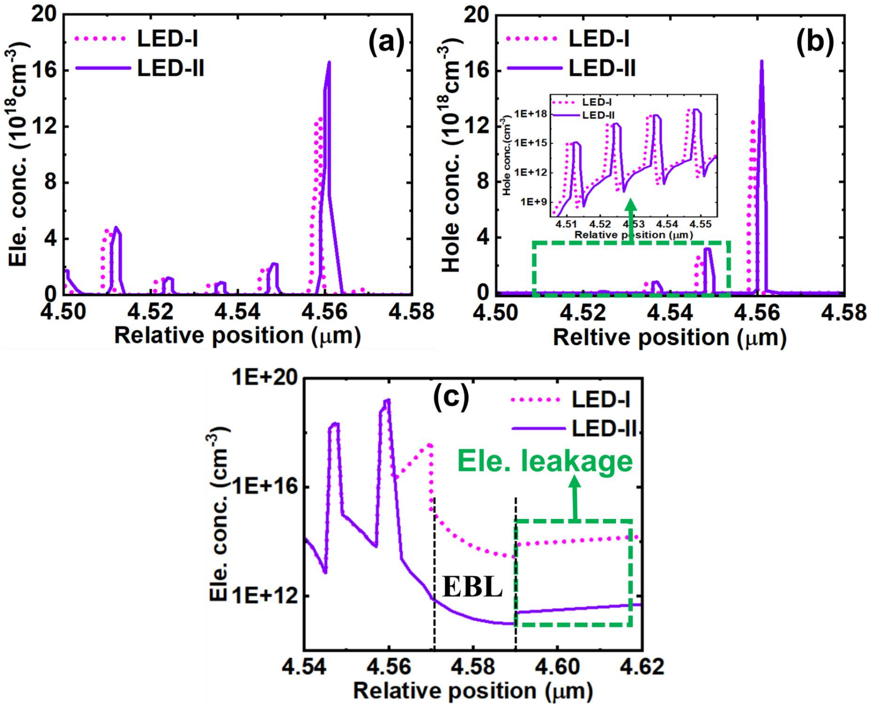

Figure 7.7 Calculated (a) electron concentration in the active region, (b) hole concentration in the active region (inset figure: Enlarged drawings of hole concentration in first 4 QWs) and (c) Electron leakage profile of LED-I, and LED-II.

Figures 7.7(a) and 7.7(b), the electron and hole concentrations in QW6 of LED-II improved greatly owing to the reduced band-bending and polarization control.The enhanced electron-hole concentrations and their confinement inside the active region of the LED-II structure result in an increase in radiative recombination, which in turn improves IQE and output power. Additionally, the higher effective potential height for electrons in the CB of QB6 and EBL in LED-II results in enhanced electron confinement and overflow prevention capabilities. As a result, as seen in Figures 7.7(c), LED-II displays much decreased electron overflow into the *p*-region. Therefore, this would decrease the possibility of nonradiative recombination between overflowing electrons and incoming holes in the *p*-type region. Overall, the reduction of severe band-bending caused by the locally produced strong electrostatic fields at the QB6/EBL interface facilitated the electron confinement and improved hole injection in LED-II and paved the way for achieving high IQE and output power.

7.3 Conclusion

In conclusion, the proposed InGaN blue LEDs with lattice-matched AlGaN last QB reported a high IQE of 97.87% at a current injection of 150mA, which is 2.49 times higher than the traditional LED. Importantly, this work demonstrates that the last QB has a significant effect on the polarization fields, effective potential barrier heights for carrier transport, IQE, and output power of InGaN multiple QW LEDs. Our numerical analysis revealed that the incorporation of the AlGaN layer as the last QB reduced the generation of significant positive sheet polarization charges at the last QB/EBL interface. Consequently, the proposed LED greatly reduce electron leakage while maintaining hole injection.

CHAPTER 8

RESISTIVE RANDOM ACCESS MEMORY DEVICES

8.1 Background

Nearly every aspect of modern life has a presence of an electronic memory device. The majority of modern electronic devices have a built-in or externally connected memory. Over the past two decades, personal electronics such as laptops, computers, digital cameras, smartphones, tablets, and other entertainment devices have resulted in a huge increase in the demand for memory devices. The usage of these devices in data centers and cloud computing platforms in recent times has added to the demand. It is the constant need of consumers for better and less expensive memory that has prompted researchers to continue innovating in the field of memory technology. The ideal memory device should exhibit

- a high data storage density so that it can store an enormous amount of data in a given die. It can be achieved by overcoming the device scaling problem or device architectural advancements.
- as low as possible power consumption.
- long retention period, where retention specifies how long data can be held inside memory devices without being accidentally lost.
- high endurance or long-lasting capabilities and endurance of a device specify how many cycles it can withstand during write and erase operations.
- a rapid programming and access speeds so that the time spent reading data from and writing data into the memory is minimal.

However, it is challenging to fabricate a memory device that has all the above-mentioned merits.

Memory devices can be divided into two types depending on their operating behavior [151], as seen in Figure 8.1. The first is a volatile memory, which must be

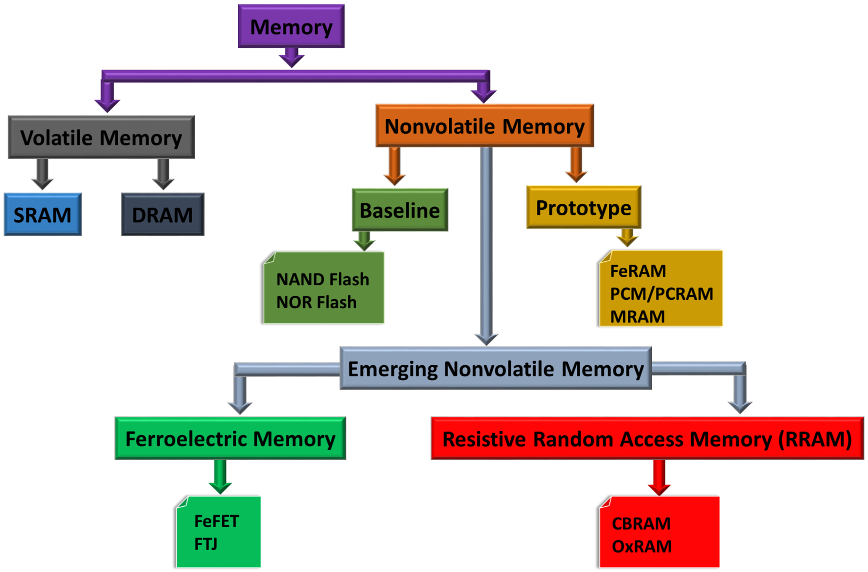

Figure 8.1 Schematic diagram of classification of memory devices.

powered on for the full operating duration. Once the power is switched off, it will lose all stored information. whereas the second is a non-volatile memory (NVM), which does not require power to sustain information, the most common commercial NVM technology is NAND flash. NAND Flash technology, on the other hand, has various drawbacks, including device scalability (< 25 nm), durability (10^6 write/erase cycles), poor operational speed writing (0.1-1 ms)/reading (0.01 ms), and requires a high write voltage (>10 V) [152, 153].

In the last several decades, many types of non-volatile random-access (RAM) memory systems, such as phase change RAM (PCRAM), magnetoresistive RAM (MRAM), ferroelectric RAM (FeRAM), and resistive RAM (RRAM), have been extensively researched to discover alternatives to Flash technology. RRAM-based non-volatile resistive switching devices have gotten a lot of interest because of their scalability, reduced power consumption, higher switching rates, longer retention durations, and simpler device construction [154].

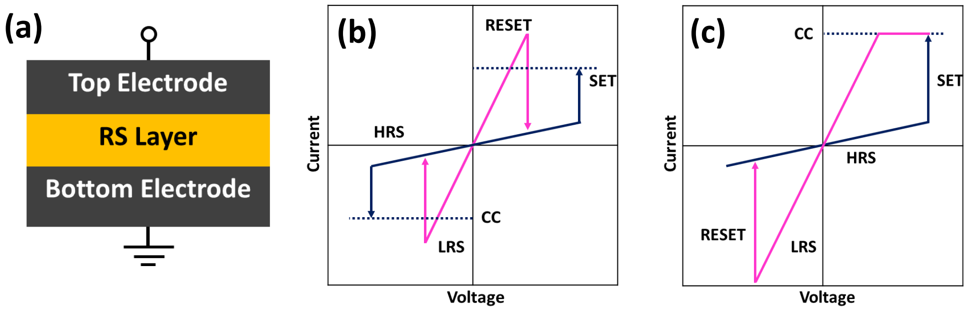

Figure 8.2 (a) Schematic diagram of RRAM structure, and schematic illustration of RRAM devices's I-V curves showing (b) Unipolar, and (c) Bipolar.

8.2 History of RRAM

The resistive switching (RS) was initially observed in various oxides such Al_2O_3, NiO, SiO_2, Ta_2O_5, ZrO_2, TiO_2, and Nb_2O_5 in the early 1960s [155–158]. However, research on the RS phenomenon in a dielectric material did not point to an obvious use at the time since, until the early 2000s, the major storage technology was either magnetic (tapes, hard drives, etc.) or optical (disc drives, etc). (CD, DVD, etc.) based technology. Following the discovery of RS behavior in binary oxide (NiO) by Samsung Electronics [159] in 2004, research has focused on binary oxides such as AlO_x [160], CuO_x [161], HfO_x [162], NiO_x [163], TiO_x [164], ZrO_x [165], ZnO_x [166], TaO_x [167], and others. Since then, both industry and academia are interested in RRAM because of the predicted advantages, which practically cover all of the benefits of an ideal memory, such as high endurance, extended retention, quick access speed, low power, and, most crucially, high density.

After 2005, extensive research and development took place on RRAM devices. The first NiO_x RRAM with promising device characteristics and reliability [159], the first integrated conductive bridge RAM (CBRAM) [168], the first HfO_2/Ti device with fully conventional fab materials [162], the first 3-D vertical RRAM [169], the first 10 nm × 10 nm RRAM devices integrated into 12-in wafer [170], the first 16-GB

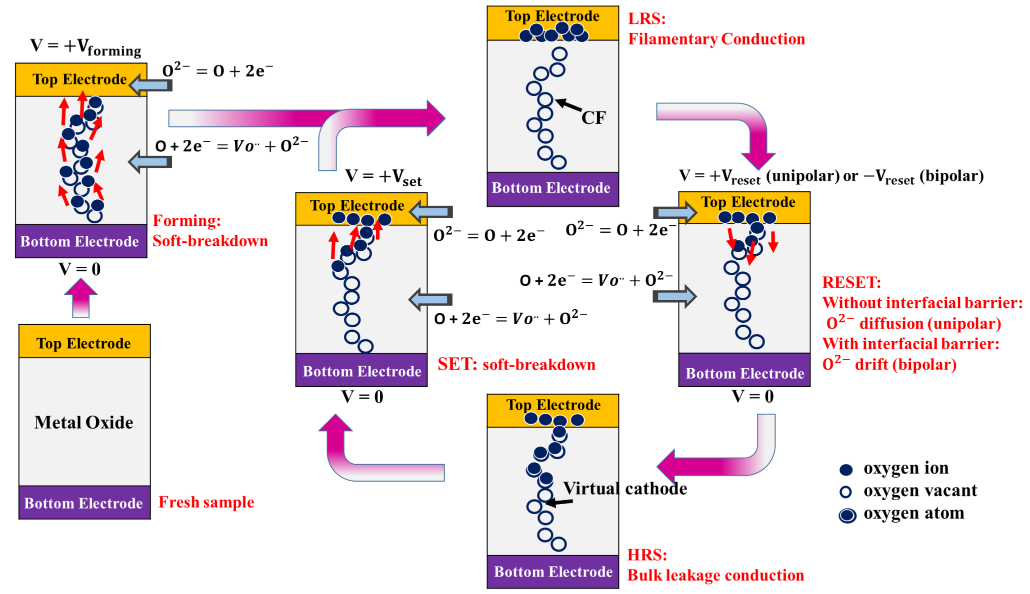

Figure 8.3 Schematic illustrations of working principal of OxRAM device. *Source:* [203].

CBRAM integrated chip [171], the first 40-nm node-embedded RRAM product [172] and many others have been reported.

8.3 RRAM-Structure, Operation

As illustrated in Figure 8.2(a), the standard RRAM device configuration includes a RS layer sandwiched between the top electrode (TE) and bottom electrode (BE). Additionally, interfacial layers also integrated between BE or TE and RS layer to improve the RRAM performance. Apart from the binary oxides, the RS has been observed in variety in large amount of materials including organic materials [173], ferromagnetic oxides [174], perovskite oxides [175], and chalcogenides [176]. The detailed list is provided in Table 8.1. However, binary metal oxide-based RRAM are of special interest because to their simple structure, thermal stability, outstanding switching capabilities, and compatibility with conventional complementary metal-oxide-semiconductor (CMOS) techniques [177].

Table 8.1 Types of RS Materials

No.	**Class of materials**	**RS layer**
1	Binary oxides	CuO [178], CoO_x [179], FeO_x [180], Gd_2O_3 [181], HfO_2 [182], MnO_x [183], NbO_x [184], NiO [185], SnO_2 [186], ZnO [187]
2	Nitride	AlN [188], BN [189], NbN [190], NiN [191], SiN_x [192]
3	Ternary perovskites	$SrTiO_3$ [193] and $SrZrO_3$ [194]
4	Organic materials	rotaxane [195], anthracene [196], tetracene [197], copper tetra(butylphenyl)porphyrin [198], polymethacrylate derivatives, phenylene ethynylenes [199]
5	Solid-state electrolytes	rotaxane [195], anthracene [196], GeS [200], GeSe [201] Cu_2S [202]

RRAMs are categorized into two types depending on their operation principle and device physics. One of them is metal ion-based electrochemical metallization (ECM) RRAM, which is also referred as conductive bridge random access memory (CBRAM). The memory switching mechanism in these devices is based on metal ion migration and subsequent reduction/oxidation processes [204,205]. The CBRAM structure consists of an oxidizable TE (anode) such as Ag, Cu, or Ni, a relatively inert BE (cathode) like W or Pt, and a sandwiched metal oxide RS layer between the two electrodes. In such memory cells, filament formation happens as a result of the dissolution of the active metal electrodes (for instance: Ag or Cu), the transit of cations (Cu+ or Ag+), and their subsequent deposition or reduction to the inert BE [206]. As a result, the formation and dissolution of metal filaments dominates the RS characteristic of this kind of RRAM. The second type is oxygen vacancy based

RRAM or OxRAM, where oxygen anion plays a vital role than metal cations thus generates oxygen vacancies and can be used as a conducting path. In this dissertation, the main focus is on OxRAM devices.

The RRAM devices operate by changing the resistance across the RS layer by the application of external voltage. Generally, the pristine RRAM devices exhibit a high resistance state (HRS). The working principle of OxRAM devices is briefly presented in Figure 8.4. Upon applying the voltage to the TE, oxygen ions get migrated through the dielectric layer where electric field, current density and local temperature are maximized within the device area. A string of oxide vacancies forms a conductive filament (CF) along with the oxide layer and switches the RRAM from HRS to a low resistance state (LRS), also called a SET process. It is known that the forming voltage, which is required to switch from HRS to LRS for pristine devices and it is much higher than the regular SET voltage during the Forming process.

The switching modes in OxRAM devices are widely categorized into two types unipolar and bipolar switching modes. A sketch of the I-V characteristics for these switching modes is shown in Figures 8.2(b) and (c). Unipolar switching indicates that the switching direction is determined by the amplitude of the applied voltage but not by its polarity. As a result, SET/RESET can occur at the same polarity i.e., at both positive and negative voltages. On the other hand, the switching direction in bipolar switching is determined by the polarity of the applied voltage, therefore, SET and RESET can happen only opposite polarities. Hence, in bipolar devices, subsequently applying the opposite voltage polarity to the TE causes the oxygen ions or defects to migrate back to the RS layer that ruptures the CF, and eventually RRAM switches back to HRS, also known as the RESET process. Further, to avoid a permanent breakdown in the FORMING/SET/RESET process, it is required to limit the current flow in the circuit called compliance current (CC).

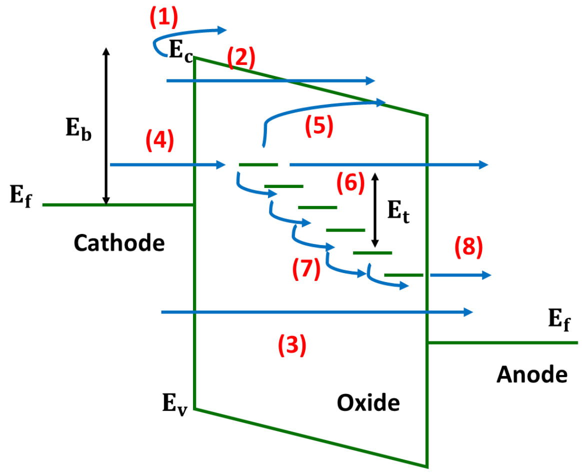

Figure 8.4 Schematic representation of possible electron conduction mechanisms in oxygen vacancy based RRAM.

The exact and detailed physical mechanisms for RS phenomenon in RRAM is still debatable and it's an active research area to further investigate. However, in general, the possible electron transport mechanisms from cathode (BE) to anode (TE) during the SET process are shown in Figure 8.4 [207]. It includes thermally activated electrons injected over the barrier into the conduction band, which is Schottky emission (1); at high electric field, electron can tunnel to the conduction band of RS layer from the cathode (2), which is called Fowler-Nordheim (F-N) tunneling; electron can tunnel directly from the cathode to the anode when the presence thin oxide, called direct tunneling (3); (4) electrons can tunnel from cathode to traps; emission from trap to conduction band, which is essentially the Poole-Frenkel emission (5); tunnel from trap to conduction band like F-N tunneling (6); trap to trap hopping or tunneling (7); and finally electrons tunneling from traps to anode (8).

8.4 Current Issues of RRAM Devices

Even though RRAM technology offers greatly improved performance in device scalability and multi bit storage capabilities, there are still several challenges hindering

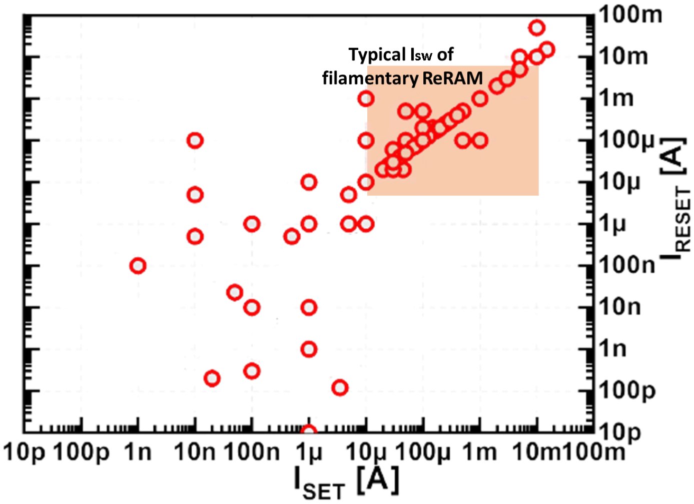

Figure 8.5 Summary of SET and RESET currents in RRAM devices. *Source:* [209].

the real application. A major problem is the uniformity and reliability of the cell-level RS from cycle to cycle operations [151, 208, 209]. The fundamental cause of variations in RRAM devices performance is the random nature of the CF. For actual memory applications, the performance variations are not acceptable. Despite the fact that numerous ideas exist on the development of conduction filaments, the conduction mechanism remains unclear and this is complicated from cycle to cycle operations [208]. Furthermore, when devices are operated at lower operating currents, because of the generation of a very weak CF that diffuses spontaneously from cycle to cycle, the randomness in the CF formation grows significantly and device performance declines noticeably, resulting in serious reliability issues [208]. Overall, RRAM cannot match with NAND/NOR flash in terms of device reliability, which limits RRAM from the commercialization [209].

The summary of SET vs. RESET current trend for RRAM devices are shown in Figure 8.5. It has been noted that the majority of the devices report the SET/RESET currents more than 10 μA. Few of the devices reported that operating currents are sub-10 μA. However, when the switching current scaling in filamentary switching, retention, uniformity, and endurance degrade greatly. This could be one of the reasons that most of the reported RRAM devices switching above 10 μA. At sub-10 μA, due to presence of more self-rectify feature that built in these area switching cells, the SET and RESET currents are usually asymmetric. In this regard, further chapters will focus on realization of highly reliable RRAM devices operating at low/ultra-low currents with the help of band-engineering. Following that, another parameter, the switching voltage on various RRAM devices varies widely. The actual switching voltage mainly depends ion mobility, RS layer thickness, parasitic resistance in the RRAM, and other factors. Altogether variations in operating currents and switching voltages from cycle to cycle leads to diminish its endurance, retention, uniformity and difficult to identify the SET and RESET states.

CHAPTER 9

MULTILEVEL RESISTIVE SWITCHING $\beta - Ga_2O_3$ RRAM DEVICES FOR LOW-POWER APPLICATIONS

Data storage is extremely important in computer systems, electronic devices, data centers, and cloud service platforms. The demand for reliable data storage is quickly expanding, with current industry expectations indicating an exponential increase. The memory sector alone is predicted to account for 27% (175 billion USD) of the total semiconductor industry (650 billion USD) by 2025 [210]. The market for NAND flash memory (non-volatile memory, NVM) is rapidly expanding, and it may soon outnumber dynamic random-access memory (DRAM) after 2025 [210]. NAND flash technology, on the other hand, has various drawbacks, including device scalability, durability (10^6 write/erase cycles), poor operational speed writing (0.1-1 ms)/reading (0.01 ms), and requires a high write voltage (>10 V) [152]. Resistive switching (RS) resistive random-access memory (RRAM) devices have recently been identified as one of the most promising developing memory technologies. They provide competitive solutions to current memory technology difficulties because to their simple structure, outstanding scalability, nanosecond operating speed, and great compatibility with existing complementary metal-oxide-semiconductor (CMOS) technology [154, 208, 211]. The RS has been discovered in organic materials [173], ferromagnetic oxides [174], perovskite oxides [175], and chalcogenides [176]. RS has also been explored in simple binary transition metal oxide materials such as ZnO [212], HfO_2 [213, 214], TiO_2 [215], and Al_2O_3 [216], where oxygen vacancies play an important role in carrier movement, as discussed in Chapter 8.

9.1 Emerging $\beta - Ga_2O_3$ as a RS Layer and Other Applications

Novel and emerging material, gallium oxide (Ga_2O_3) material holds key properties such as conductivity sensitive to the oxygen content [217, 218], and a wide band-gap of 4.4-4.9 eV [31, 219, 220]. It also allows for a high intrinsic resistance state due to the limited carrier mobility caused by the effective mass of 0.342 $m_\circ$ (where mo is free electron mass) [31]. Importantly, Ga_2O_3 has strong thermal and chemical stability [32], which can help to reduce performance deterioration in RRAM devices in the low resistance state (LRS) and high resistance state (HRS). As a result, Ga_2O_3 may become a potential choice for the RS layer in RRAM; nevertheless, just a few investigations on these sorts of RRAM devices have been documented. Because of its inherent high resistance and exceptionally sensitive conductivity to oxygen, amorphous Ga_2O_3 is thought to be a suitable material for RS devices [32, 221]. Gao et al. studied the effect of various top electrodes on the RS behavior during early experiments on Ga_2O_3 RRAM devices, revealing that the mobility of oxygen vacancies in the vicinity of the electrode region is critical in the RS process [222]. Furthermore, bipolar RS properties in Ga_2O_3 RRAM devices have been reported [222–225].

Furthermore, due to the wide band-gap, well-controlled doping, availability of large-size uniform substrates, high breakdown electric field of 8 MV cm^{-1} [226], low electron Hall mobility of 200 cm^2 V^{-1} s^{-1} [227], formation of 2-dimensional electron gas of 10^{12} cm^{-2} [4], and a relative dielectric constant of 10-16 [4, 228], several studies have shown emerging interests in Ga_2O_3 semiconductor material for power electronics [4], sensors [229], and photodetectors [230]. Moreover, it is easy to fabricate at room temperature [4]. As a result, demonstrating high-performance Ga_2O_3-based RRAM is critical not only for consumer electronics and enterprise storage solutions, but also for power electronic and photonic circuit applications. In this regard, the multi-layer Ti/TiN(bottom electrode, BE)/Ga_2O_3/Ti/Pt(top electrode, TE) thin-film RRAM devices are carefully designed, fabricated and results are reported in this chapter.

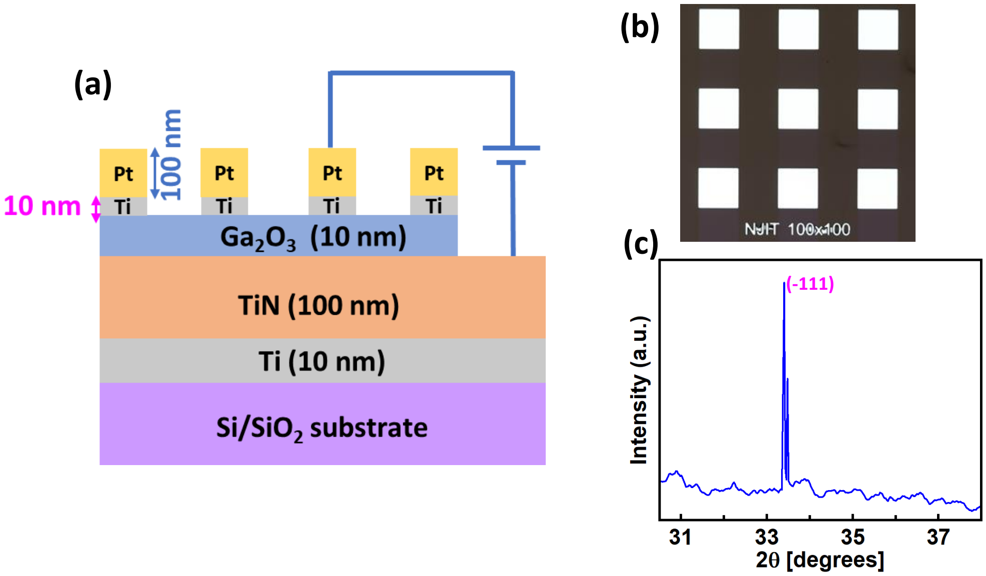

Figure 9.1 (a) Schematic diagram of Ga_2O_3 RRAM devices, (b) Optical image of the fabricated RRAM devices (device area: $100 \times 100\,\mu m^2$), and (c) XRD pattern of Ga_2O_3 thin-film deposited on BE.

The efficient bipolar RS behavior in $\beta - Ga_2O_3$ RRAM devices with high Roff/Ron ratio has been reported. Further, multi-bit storage capability of these devices are investigated.

9.2 Device Fabrication and Structural Characterization

To study RS behavior, Ti/TiN/Ga_2O_3/Ti/Pt devices are fabricated with a device size of $100 \times 100\,\mu m^2$ on SiO_2/Si substrates . The schematic diagram of the $\beta - Ga_2O_3$ based RRAM device is shown in Figure 9.1(a). The fabrication started with a 2-inch silicon wafer covered by a 270 nm thermally grown SiO_2 layer, which was used as the device substrate. First, the organic contamination was removed from wafer by cleaning it using acetone and IPA and were blown off in nitrogen. Using the AJA sputter tool, the BE includes Ti and TiN were deposited. During this deposition process, the first Ar cleaning was done at a flow of 40 sccm and pressure of 16 mTorr for 60 sec. A 10 nm Ti layer was then deposited at a pressure of 3 mTorr, power of

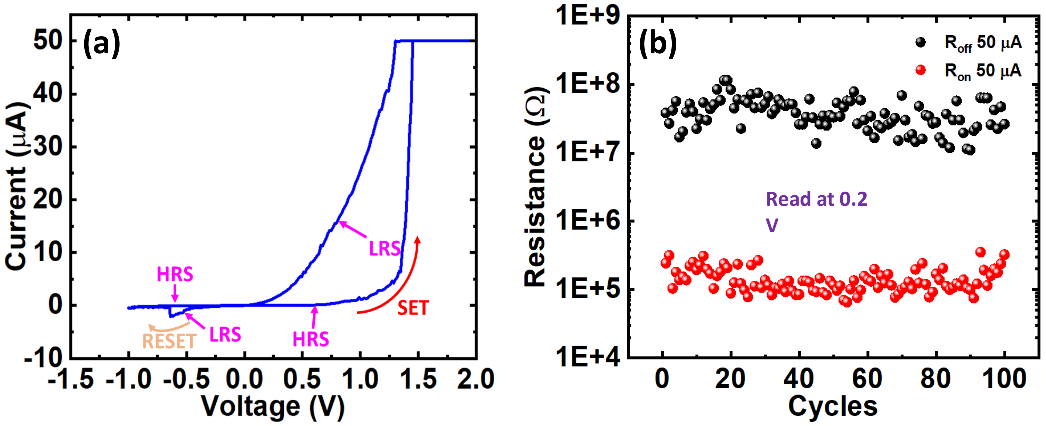

Figure 9.2 (a) Current-voltage characteristics of Ti/TiN/Ga_2O_3/Ti/Pt RRAM device. (b) Endurance characteristics of RRAM devices at a read voltage of 0.2 V.

400 W and Ar flow of 30 sccm. A 100 nm TiN layer was reactive sputtered on Ti layer at a pressure of 3 mTorr, power of 400 W, Ar and N2 flow of 15 sccm.

Subsequently, the BE on the substrate was vacuum pre-annealed at 625 °C for 35 min, facilitating the creation of a smooth gallium oxide surface [231]. Next, a seed layer of Ga_2O_3 was deposited to control the impact of lattice mismatch between the BE and the Ga_2O_3 thin film. Further, an appropriate template for the efficient epitaxial growth of a $\beta-Ga_2O_3$ film is created by post-annealing at 625 °C for 35 min. Next, the 10 nm Ga_2O_3 RS layer was deposited at 100 W RF power and pressure of 3mTorr while the ratio of Ar:O_2 gas flow was kept at 1:1. The as-grown Ga_2O_3 film's structural characteristics were determined using the Empyrean X-ray diffraction tool and are shown in Figure 9.1(c). The XRD pattern shows a clear common diffraction peak at 33.4° of 2θ which corresponds to the (-111) of the $\beta - Ga_2O_3$ phase (JCPDS 00-041-1103), respectively. This confirms the presence of a pure $\beta - Ga_2O_3$ RS layer in the fabricated RRAM devices.

The Ga_2O_3 layer was patterned in the following steps. First, liquid priming was used in the priming procedure. The HMDS solution (usually 10%-20% HMDS in

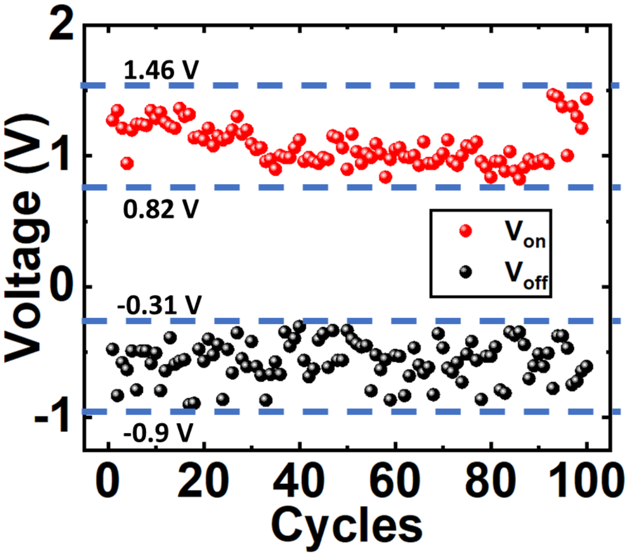

Figure 9.3 Statistical distribution of SET and RESET voltages of Ti/TiN/Ga_2O_3/Ti/Pt RRAM device for 100 cycles.

PGMEA) was applied to the static wafer for this purpose. The solution was left on the surface for 10 seconds before being spun off at a rate of 3000 rounds per minute (rpm) for 60 seconds to dry the wafer. The PGMEA displaces the bulk of the water on the surface of a bare wafer and HMDS, then displaces and binds to maintain the surface dehydrated. HMDS, in essence, enhances photoresist (PR) adherence to the wafer surface. Following the primer, the S1813 positive PR was applied and spun off at 3000 rpm for 60 seconds, followed by a one-minute soft bake at 115°C. PR was exposed using an ABM contact aligner after soft baking. MIF 726 PR developer was then used to develop the exposed PR. The wafer was finally put into the e-beam evaporator chamber for top metal deposition. A 10 nm Ti layer was evaporated during the evaporation process, followed by a 100 nm Pt layer that acts as the top electrode. Figure 9.1(b) depicts the optical picture of the manufactured devices.

Table 9.1 Comparison of RS Characteristics of Various Ga_2O_3 RRAM Structures

RRAM structure	**V_{on}**	**Non-overlapping window**	**R_{off}/R_{on}**	**CC**	**Multi-bit storage**
ITO/NiO_x/GaO_x/Ti/Au	(3-4) V	-	10	0.1 mA	No
Pt/$GaO_{1.3}$/Pt	1.5 V	-	2	10 mA	No
IGZO/Ga_2O_3/IGZO	1.5 V	-	14	150 μA	No
ITO/Cu_2O/Ga_2O_3/Ti/Au	3.25 V	3.1 V	10^2	5 mA	No
Ti/Pt/Ga_2O_3/Pt	3 V	-	25	1 mA	No
Pt/Ga_2O_3/Ta	(0.6-0.75) V	-	50	5 mA	No
Pt/SiC/GaO_x/Pt	(0.82-1.92) V	1.2 V	10^3	80 mA	No
Ti/TiN/Ga_2O_3/Ti/Pt (this work)	(0.82-1.46) V	1.1 V	10^3	80 μA	yes

9.3 Results and Discussion

The fabricated devices were electrically characterized using the Keysight B1500A semiconductor device parameter analyzer. Figure 9.2(a) depicts the current-voltage characteristics of the Ti/TiN/Ga_2O_3/Ti/Pt device's bipolar switching. To avoid strong breakdown of the dielectric layer, a sweep voltage of $0 \to 2 \to 0 \to -1 \to 0$ with a compliance current (I_{cc}) of 50 μA is provided to the top electrode. The pristine memory device, as shown in Figure 9.4(a), is initially in a high-resistance state, HRS (RESET state). When a positive voltage is applied to the top electrode from $0 \to 2$, as illustrated in Figure 9.4(b), oxygen ions are attracted to the top electrode, leaving the oxygen vacancies behind.

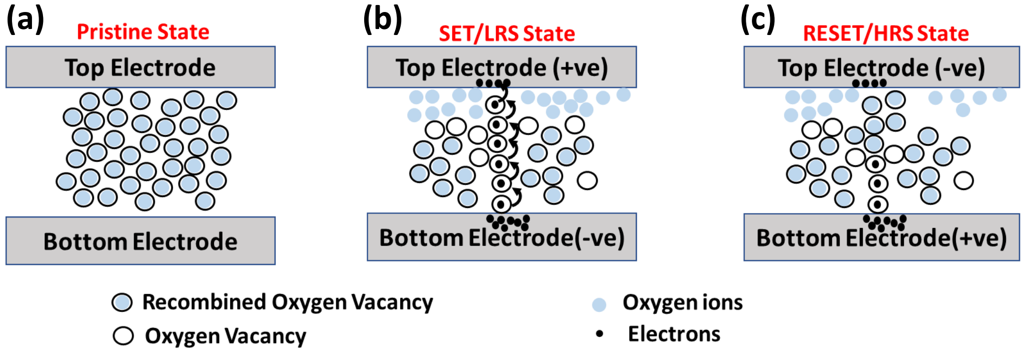

Figure 9.4 Schematic illustrations of working principal of RRAM device including three primary states: (a) pristine state, (b) SET/LRS state, and (c) RESET/HRS state.

At a particular positive voltage of ∼1V, there are enough oxygen vacancies in the oxide layer for electrons from the BE to hop through and reach the other end of the electrode. As a result, current flows through the device, and it enters a low-resistance state, or LRS (SET state). During the LRS state, the I_{cc} regulates the amount of current that passes through the device. A negative voltage is given to the top electrode during the RESET procedure in Figure 9.4(c). Due to the combined effects of Joule heating and the presence of an electric field, the oxygen ions start diffusing back from the top electrode into the oxide layer and recombining with the oxygen vacancies. As a result, the available oxygen vacancies are diminished, and the conductive path for the electron flow is disrupted. As a result, the device is switched back to HRS from LRS. The Figure 9.3 demonstrates the statistical distribution of SET and RESET voltages of a Ga_2O_3 RRAM device over 100 cycles. The SET voltage ranges from 0.82 V to 1.46 V, whereas the RESET value ranges from -0.31V to -0.9 V. The non-overlapping window between these SET and RESET voltages is 1.1 V, which is required for the RRAM application [32].

The results of the endurance test for 100 cycles at a read voltage of 0.2 V are shown in Figure 9.2(b), with the average R_{off}/R_{on} ratio value being about 300 and

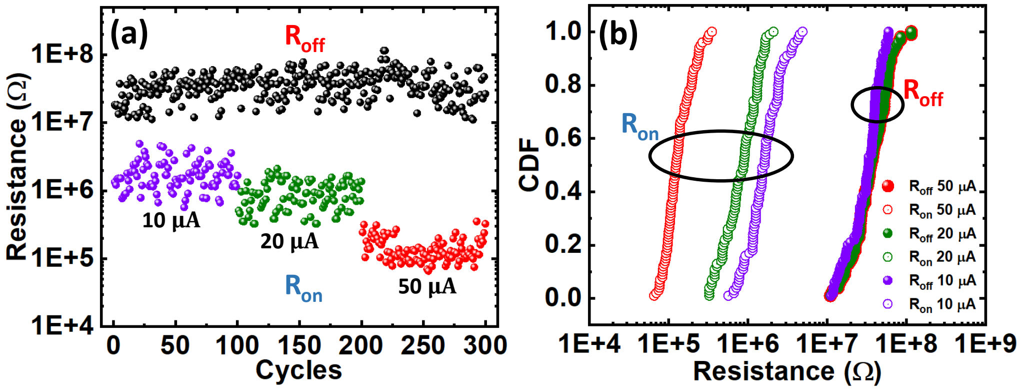

Figure 9.5 (a) Endurance characteristics of Ti/TiN/Ga_2O_3/Ti/Pt RRAM devices over 300 operating cycles with varying compliance currents (10 μA, 20 μA, and 50 μA), and (b) Cumulative distribution characteristics of these RRAM devices for varying compliance currents (10 μA, 20 μA, and 50 μA).

the maximum value being $\sim 10^3$ times. Because the RRAM device's SET voltage is 0.82 V to 1.46 V and the RESET voltage is -0.31 V to -0.9 V, the read voltage is chosen so that it has no effect on the RRAM device's state. During the forward positive cycle (0 V to 2 V) before it reaches the set voltage, the device is in HRS. So, Roff is calculated with the current value obtained at a read voltage of 0.2 V. Similarly, the device is in a SET state as long as the filament is present throughout the forward negative cycle (0 V to -1 V) until it reaches the reset voltage. So, Ron is determined using the current value at a read voltage of -0.2 V. Table 9.1 compares the RS properties of these RRAM devices to those of other Ga_2O_3 RRAM devices.

Further, the multilevel switching capability of Ga_2O_3-based RRAM devices as a function of increasing I_{cc} were investigated and is shown in Figure 9.5. To the best knowledge, this is the first experimental report on the multilayer switching capabilities of Ga_2O_3-based RRAM devices. When illustrated in Figure 9.5(a), the LRS (R_{on}) clearly exhibits a pattern that leads to three different LRS states as I_{cc} increases from 10 μA to 50 μA. The HRS, on the other hand, is essentially constant for all compliance

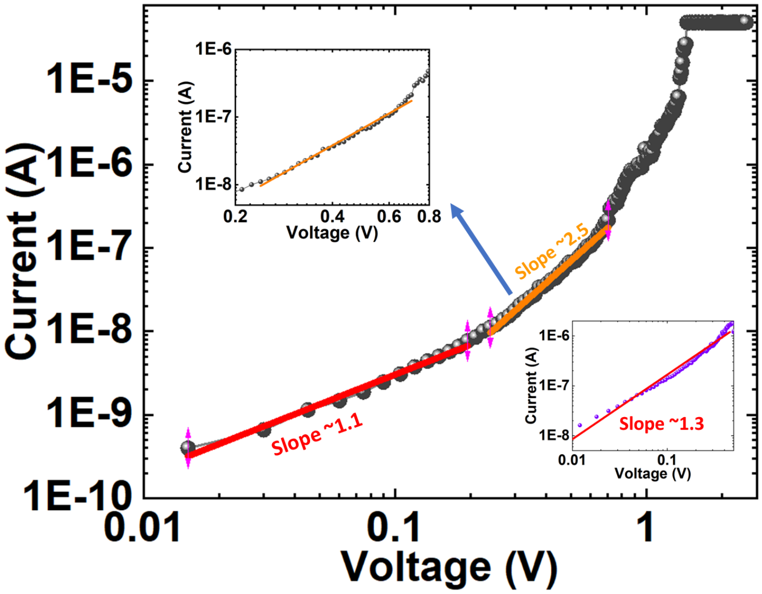

Figure 9.6 Typical I-V characteristics of Ti/TiN/Ga_2O_3/Ti/Pt RRAM devices plotted on double logarithmic scales under positive bias (HRS), (left-top inset) zoom-in of higher bias voltage (0.2 V-0.7 V) characteristics, (right-bottom) I-V characteristics under negative bias (LRS).

currents. The four distinct resistance levels produced by the three separate LRS states and one HRS state can increase storage density up to two times that of a single-state cell with the same die area [232]. The mechanism behind multilevel switching by controlling the I_{cc} can be attributed to the formation and subsequent lateral widening of the conducting filament with increasing I_{cc} [208, 232]. With the wider diameter of the conducting filament, the resistance becomes smaller and resulting in multiple LRS states. Figure 9.4(b) also shows the endurance characteristics of the RRAM device at various I_{cc} values. The temporal (cycle-to-cycle) variation in HRS can be attributed to the stochastic nature of the conductive filament inside the switching matrix [208, 232]. Because low-power operation of memory devices necessitates lower programming currents, the I_{cc} values used in this investigation were relatively low. However, reliable and distinct multiple resistive states were achieved.

The typical I-V characteristics are redrawn on a double logarithmic scale to better comprehend the RS process. The conduction processes for the HRS are more intricate, as seen in Figure 9.6 (major graph), and are ascribed to the space-charge restricted current (SCLC). At the lower region i.e., 0 to 0.2 V, the current is proportional to the voltage and follows Ohm's law with a slope of 1.1. Electrons are injected from BE into traps/vacancies in the Ga_2O_3 RS layer during this area, and ohmic conduction is prominent. Because there are more thermally produced carriers than injected carriers, the observed current is mostly attributable to the free thermal carrier inside the RS layer. The traps inside the RS layer are gradually filled by injected carriers when the bias voltage is increased from 0.2 V to 0.7 V. As a result, a large number of free carriers contribute to current conduction in the presence of a strong electric field, resulting in a steep current-voltage slope of 2.5 [233]. There is also a noticeable shift of the Fermi level upwards and over the electron trapping level can be observed [234].

When a voltage greater than 0.7 V is applied, the Fermi level rises higher and can be extremely close to the bottom of the RS layer's conduction band. This promotes free electron mobility, even as the RS and slope of the I-V curve rapidly rise. The current in the LRS does not vary linearly on the applied voltage, as illustrated in the right-bottom inset figure, with a slope of unit ~ 1.3. Furthermore, direct tunneling is believed to be prevalent in the low voltage domain of LRS in oxygen vacancy-based RRAM devices [235], introducing non-linear ohmic properties. This may be solved by raising the thin film thickness of the RS layer, which reduces direct tunneling at low voltage regimes.

9.4 Conclusion

In conclusion, the efficient bipolar RS property was demonstrated in Ti/TiN/Ga_2O_3/Ti/Pt based RRAM devices and bipolar RS behavior was systematically studied. The reported devices exhibited excellent RS properties, including low set voltages (0.82 V-1.46 V) with a better non-overlapping window of 1.1 V, and a high R_{off}/R_{on}

ratio (up to 10^3) at a lower compliance current. Importantly, the described RRAM devices can perform multi-bit resistive switching even at low compliance currents. The distinct and lower switching voltages, as well as the outstanding repeatability, of novel-emerging Ga_2O_3-based RRAM devices make them an ideal match and viable choice for practical storage applications.

However, it is critical to investigate the degree of amorphization and major crystalline defects in the RS layer, oxidation states, structural properties at the oxide (RS) layer and metal electrode interface, and RS layer surface profile using advanced structural characterization tools to better understand the formation of conducting filament. Such research is currently underway and will undoubtedly aid in our understanding of actual RS mechanisms in Ga_2O_3 RRAM devices.

CHAPTER 10

HIGHLY UNIFORM ULTRALOW POWER RESISTIVE SWITCHING IN SIO_2/SIN_x RRAM DEVICES

RRAM, as one of the emerging memory technologies, has piqued the interest of researchers due to a number of benefits such as its simple structure, fast switching speed, high endurance, extended retention, and strong scaling capabilities [236, 237]. RRAM is projected to be employed for high-density non-volatile memory as well as neuromorphic computing applications due to the benefits outlined above [238]. Operating voltages are often decreased by optimizing the switching layer materials and thicknesses.

However, reducing the programming current is difficult due to the development of a very weak conducting filament that diffuses spontaneously from cycle to cycle [239]. Simultaneously, low current programming capable RRAMs are necessary for successful RRAM device commercialization in order to minimize power consumption, alleviate series line resistance, and lower the current density required for programming circuitry and potential selector device integration [240]. At the same time, it is critical that RRAM demonstrate a continuous, uniform, and consistent change in conductivity. To the best knowledge, highly reliable SiO_2 RRAM devices have been reported, but at a high operating current [241, 242]. In this chapter, the improved uniformity of resistive switching (RS) characteristics is demonstrated for $Ti/TiN/SiO_2/Ti/Pt$ RRAM devices by incorporating a SiN_x layer before the top electrode at a reduced programming current of 10 nA which also offers multi-level bit storage capability.

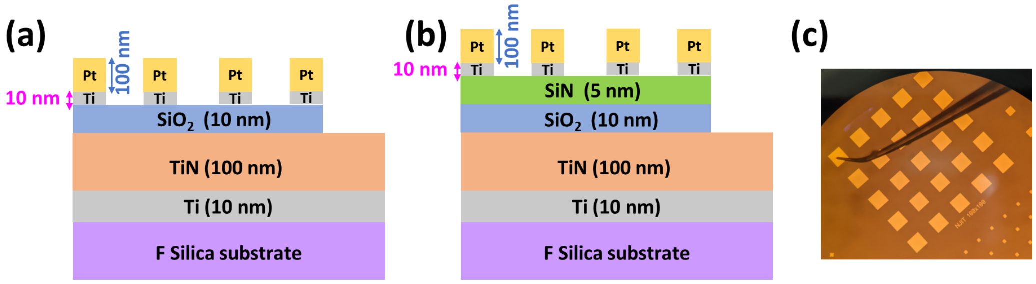

Figure 10.1 Schematic diagram of (a) R1 device design (with only SiO_2 RS layer), (b) R2 device design (SiN_x/SiO_2 RS bilayer), and (c) Optical image of the R2 device.

10.1 Device Fabrication

The RS performance is investigated in conventional single RS layer (SiO_2) and bi RS layers (SiN_x/SiO_2) RRAM devices. The single RS layer structured RRAM (R1) devices have Ti (10 nm)/TiN (100 nm)/SiO_2 (10 nm)/Ti (10 nm)/Pt (100 nm) and are fabricated with a device size of 100 × 100 μm^2 on Fused silica substrate. The R2 device is bi RS layer consists of Ti (10 nm)/TiN (100 nm)/SiO_2 (10 nm)/SiN_x (5 nm)/Ti (10 nm)/Pt (100 nm). The schematic diagrams of the R1 and R2 devices are shown in Figures 10.1 (a) and (b). In this study, Fused Silica was used as the device substrate. First, the wafer was cleaned using acetone and IPA to remove organic contamination. The cleaned wafers were blown off in nitrogen. The bottom electrode (BE) that includes Ti and TiN were then sputter-deposited using the AJA sputtering system. During the deposition process, the first Ar cleaning was done at a flow of 40 sccm and pressure of 16 mTorr for 60 sec. A 10 nm Ti layer was then deposited at a pressure of 3mTorr, power of 400W and Ar flow of 30 sccm. A 100 nm TiN layer was reactive sputtered on Ti layer at a pressure of 3 mTorr, power of 400 W, Ar and N_2 flow of 15 sccm. Next, SiO_2 film on R1 and SiO_2 and SiN_x films on R2 were deposited respectively using the Oxford ALD FlexAL.

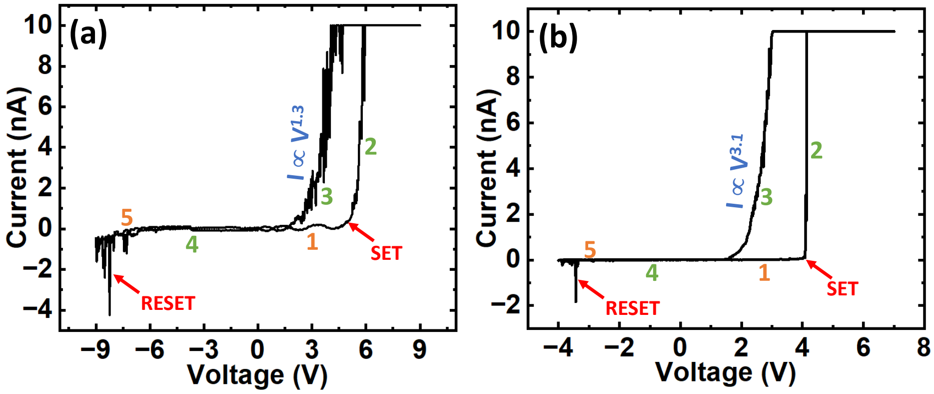

Figure 10.2 Current-voltage characteristics of (a) R1device, and (b) R2 device.

Tris(Dimethylamino)Silane (3DMAS) was used as the metal precursor for the deposition. During the growth process, the substrate temperature was maintined at 300°C, and 350°C, RF power was maintained at 300 W and 290 W, chamber pressure was held at 15 mtorr and 10 mtorr for SiO_2 and SiN_x, respectively. The flow rates of Ar/O_2 and Ar/N_2 are 20/40 sccm and 20/40 sccm while depositing SiO_2 and SiN_x, respectively. Finally, the wafer was loaded into the e-beam evaporator chamber for the top metal deposition. During the evaporation, a 10 nm Ti layer was evaporated, followed by a 100 nm Pt layer which serves as the TE. The optical image of the fabricated devices is shown in Figure 10.1 (c). The electrical characterization of the RRAM devices was performed using the Keysight B1500A semiconductor device parameter analyzer. Here, the voltage bias is always applied on the top electrode (TE) and the BE is grounded.

10.2 Device Characterization and Discussion

Figures 10.2(a) and (b) show typical I-V characteristics of the R1 (SiO_2 RS layer) and R2 (SiN_x/SiO_2) devices. When a positive voltage is provided to the TE, the RRAM device switches from its high resistance state (HRS) to its low resistance

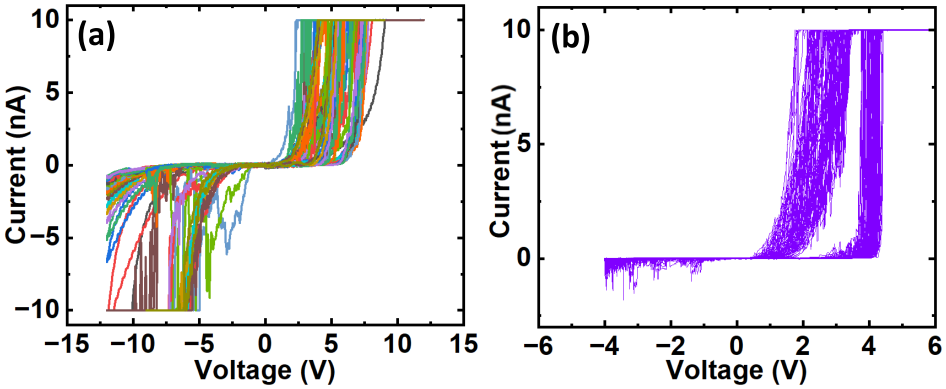

Figure 10.3 Current-voltage characteristics of (a) R1 device of 50 cycles, and (b) R2 device of 200 cycles.

state (LRS), and this is referred as the SET process. The RRAM device returns to the HRS from the LRS by supplying a negative voltage to TE; this is known as the RESET procedure. Bipolar RS can be seen in both R1 and R2 devices, which report SET voltages (V_{SET}) of 5 V and 4 V, respectively. The RESET voltages (V_{RESET}) of these devices are ∼ -7 V and ∼ -3.5 V respectively. Further, the current conduction mechanisms of R1 and R2 devices are investigated. As shown in Figure 10.2, during the LRS (denoted as 3 in the figure), the current conduction of the R1 device is dominated by the Ohmic conduction. Therefore, a continuous filament is formed between TE and BE of R1 device after the SET process which is conductive and exhibits Ohmic conduction behavior in LRS [243].

On the other hand, from Figure 10.2(b), the current conduction in the LRS of the bilayer R2 device is supported by the space-charge limited current (SCLC) conduction mechanism which supports the filament formation with a strong base [240, 244, 245]. Overall, the compliance current (I_{cc} = 10 nA) controls the amount of current that flows through the device during the LRS state. Although the RS was seen in R1 even at 10 nA lower I_{cc}, the poor uniformity in I-V characteristics from cycle to cycle is also reported in Figure 10.3(a). This is mainly due to the formation

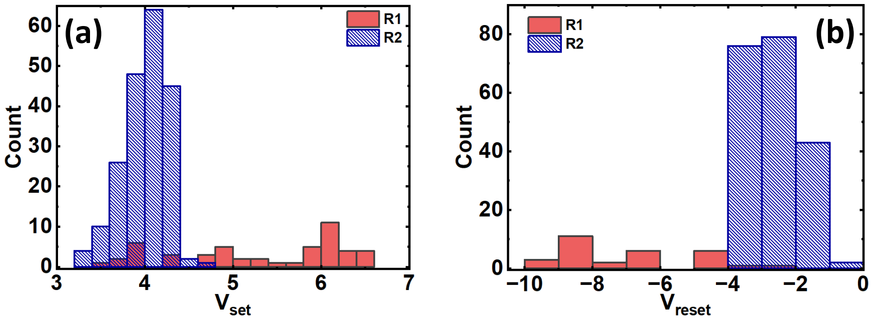

Figure 10.4 (a) The statistical distribution of SET voltages of R1 and R2 devices, and (b) The statistical distribution of RESET voltages of R1 and R2 devices.

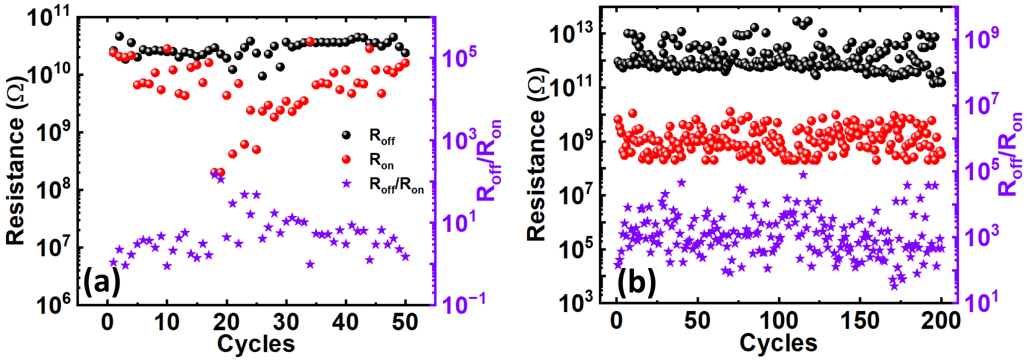

Figure 10.5 Distributions of HRS ((R_{off})), LRS ((R_{on})), and (R_{off})/(R_{on}) of (a) R1 device, and (b) R2 device.

of weaker conducting filament at low Icc, which is highly unstable and fluctuates over time in the R1 device [246, 247]. From Figures 10.4(a) and (b), the non-overlapping window between these V_{SET} and V_{RESET} in the R1 device is 5V between the two resistance states of LRS and HRS, which is essential for the RRAM applications [32]. However, the V_{SET} is seen to vary in a wide range i.e., ∼3 V to 7 V and V_{RESET} in the range of -2 V to -10 V which is not desirable.

Overall, the memory cell in R1 is inconsistent and unstable from cycle to cycle, which is one of the major challenges restricting production on a larger scale, particularly for low-power applications. Furthermore, the cycle to cycle variability in R1 is shown to be mostly reliant on the quantity of oxygen vacancies that occur during the formation of conductive filament (CF) [248]. Because of the random nature of CF creation, it is exceedingly difficult to regulate and modify the CF. This unpredictability worsens when the compliance limit is reduced (i.e., nA range). The introduction of SiN_x in bilayer RRAM (R2) offers uniform resistive switching even at 10 nA I_{cc} due to the possibility of filament formation with a stronger base and corresponding I-V characteristics can be seen in Figure 10.3(b). As a result, the V_{SET} and V_{RESET} distributions of R2 device are 3.3 V − 4.7 V, (-0.5 V) − (-3.5 V) which are more concentrative than R1.

Figures 10.5(a) and (b) show the resistance states profiles of R1 and R2 devices for HRS (R_{off}) and LRS (R_{on}). As predicted, the R1 device displayed nonuniform and unstable resistance values during HRS and LRS due to the formation of a weak conduction filament, which has a higher tendency to vary from cycle to cycle. Subsequently, the average R_{off}/R_{on} value for R1 is ∼12. Cumulative distributions of resistance states for both R1 and R2 are presented in Figure 10.6(a). In R1 memory cell, occasionally leaky LRS have been found (bottom circle in Figure 10.6(a)), it is necessary to reduce LRS current for better RESET. In addition, HRS and LRS may not be clearly distinguished (top circle in Figure 10.6(a) during some of the cycle operations) due to an inefficient way of filament formation which remains keeps R1 in HRS. When compared to the R1 device's resistance state profile, those of the R2 device display a more stable and uniform distribution, owing to the steady resistance transition during SET and RESET operations. Furthermore, the much increased performance in R2 can be attributed to the filament formation with a stronger base, which regulates the R_{off} and R_{on} via the SiN_x layer integration. As a consequence, consistent R_{off} and R_{on} values are recorded, and it is worth noting that the R_{off}/R_{on}

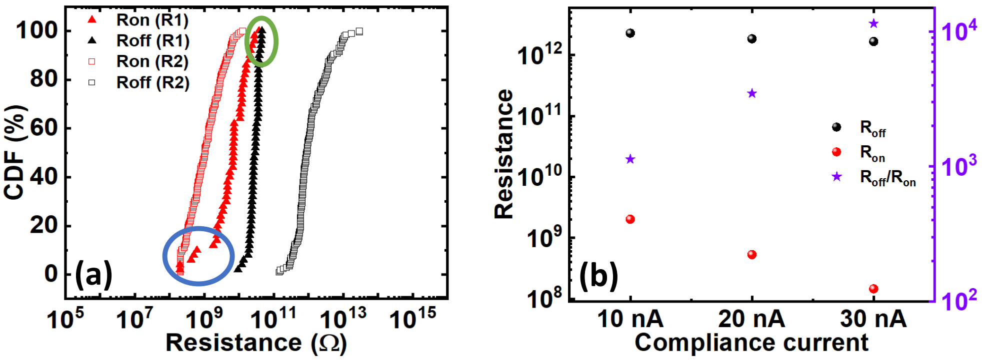

Figure 10.6 (a) Cumulative distributions of resistance of R1 and R2 devices measured at 2 V, and (b) R_{off}, R_{on}, and R_{off}/R_{on} values at 10 nA, 20 nA, and 30 nA respectively.

of the R2 device is likewise well maintained, with an average value of 3500 when compared to the R1, as shown in Figure 10.5(b).

Further, the greatly improved performance can be understood from the cumulative distribution profile of R2 from Figure 10.6(a). Next, the multilevel switching possibility of the proposed R2 device is examined. The average R_{on}, R_{off} and R_{off}/R_{on} ratios for 25 cycles of different I_{cc} (10 nA, 20 nA, and 30 nA) are shown in Figure 10.6(b). With the increase in I_{cc} from 10 nA to 30 nA, Ron clearly shows a trend that leads to three different LRS states whereas the R_{off} remains almost constant for all I_{cc}. As a result, with the increase of I_{cc} the R_{off}/R_{on} ratio is increased, which validates the multi-level switching properties of the proposed structure. As the multilevel switching behavior is observed for very low currents in nA, these devices are suitable for low-power applications.

The schematic schematics of RS processes in R1 and R2 devices are shown in Figures 10.7(a)-(c) and Figures 10.7(d)-(e), respectively. As seen in Figures 10.7(a) and (b), both pristine memory devices are initially in a RESET condition. When a positive voltage is applied to the TE, oxygen ions are drawn toward the TE, leaving

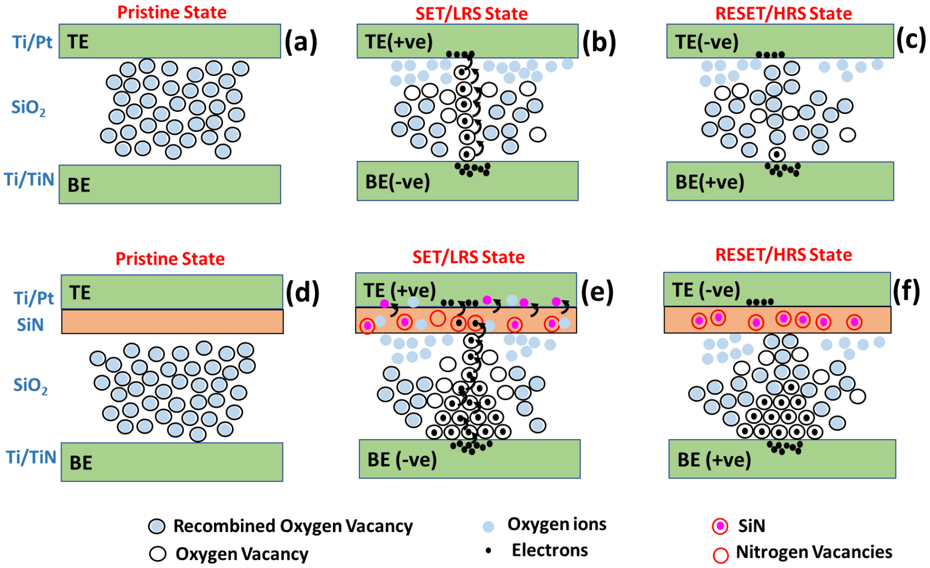

Figure 10.7 Models for (a), (d) pristine (b), (e) LRS, and (c), (f) HRS of R1 and R2 devices, respectively.

oxygen vacancies behind. When there are enough oxygen vacancies in the switching layer for electrons to jump through and reach the TE, current flows through the device and it changes to a SET state. This is the most common scenario in the R1 device (Figure 10.7(b)). In addition to the above-mentioned mechanism, two more additional mechanisms are involved in the case of the R2 device to generate excess vacancies. First, during the pristine state of R2, a part of Ti exists as metal Ti, the other part reacts with N and forms silicon dangling bonds (Si DBs) at the Ti/SiN$_x$ interface. During the SET process, Si-N bonds can be broken, N ions get attracted to the TE and leave behind the nitrogen vacancies. The process could be described by the following expression [249],

$$\mathrm{Si-N+Ti\rightarrow=Si+Ti-N}$$

where Si − N; Ti; =Si; and Ti − N are the bonded silicon, Ti metal, Si DBs, and Ti nitride, respectively.

Secondly, in addition to Si DBs at $\mathrm{SiN_x}$/TE interface, the existence of Si dangling bonds (DBs) at the interface of $\mathrm{SiN_x/SiO_2}$ helps attract relatively higher number of oxygen ions compared to R1 towards it and leaves oxygen vacancies behind. Some of those attracted oxygen ions will be captured by the Si DBs, while the remaining uncaptured oxygen ions would continue migrating to the top electrode and generate $\mathrm{TiO_2}$ at the interface of $\mathrm{Ti/SiN_x}$, for Ti is known as an excellent oxygen reservoir [250].

$$\mathrm{O''} + = \mathrm{Si} \rightarrow \mathrm{Si} - \mathrm{O} + \mathrm{O} \cdot\cdot$$

$$\mathrm{O''} + \mathrm{Ti} \rightarrow \mathrm{Ti} - \mathrm{O} + \mathrm{O} \cdot\cdot$$

Where $\mathrm{O''}$, $=\mathrm{Si}$, $\mathrm{Si} - \mathrm{O}$, $\mathrm{O} \cdot\cdot$, Ti and $\mathrm{Ti} - \mathrm{O}$ are the oxygen ion, Si-DBs, Si oxide, oxygen vacancy, Ti metal and Ti nitride, respectively. As a result, a higher number of oxygen vacancies will be generated in the proposed structure, and it is expected to form a conductive filament with a stronger base [245] with a weak tip on the another side, as shown in Figure 10.7(e). During the RESET process in R1 (Figure 10.7(c)), spontaneous diffusion of filament takes place due to the weaker filament and which is responsible for the unstable RS characteristics. Where as in R2 (Figure 10.7(e)), probably conduction filament is breaking only around weak tip which offer uniform and stable RS characteristics.

10.3 Conclusion

RS properties have been observed in oxygen vacancy-based RRAM devices. However, reported results have poor uniformity and unstable current-voltage characteristics from a cycle-to-cycle operation for ultra-low operating currents (nA) due to the formation of weaker conducting filament. To overcome these limitations, highly uniform and stable RS, ultralow operating current (10 nA) of $\mathrm{SiO_2/SiN_x}$ RRAM devices have been demonstrated in this chapter. Importantly, the reported devices exhibited the improved statistical distribution of device parameters along with a high R_{off}/R_{on} ratio ($> 10^3$). Also, the reported RRAM devices report the capability of multi-bit resistive switching phenomena even at ultralow compliance currents.

CHAPTER 11

CONCLUSION AND FUTURE WORK

In summary, several novel designs and structures are presented in this dissertation for the improved the device performance of photonic and electronic devices, particularly light-emitting diodes (LEDs) and resistive random-access memory (RRAM) devices. To begin with, the first axial AlInN core-shell nanowire ultraviolet (UV) LED with high crystalline quality is successfully demonstrated with an internal quantum efficiency (IQE) of 52%. Even though the AlInN semiconductor has several potential uses in UV and visible light-emitting devices, it has not been extensively researched since the epitaxial growth is challenging. Light extraction efficiency for various nanowire photonic crystal arrangements is also explored. According to the results obtained, the optimized hexagonal photonic crystal array can emit 63% of the light, and the primary direction of light emission is from the top surface of nanowires. As a result of this work, AlInN can be used as an alternate III-nitride material for light-emitting applications while the efficiency of AlGaN-based UV LEDs is largely in the single-digit percentage range.

Next, one of the critical problems in AlGaN deep UV LEDs i.e., electron leakage is addressed in this dissertation by band-engineering various epilayers of the LED structure without using any electron blocking layer (EBL) layer, thereby demonstrating the improvement in the device performance. Among the several structures, in the first structure, an optimized thin undoped AlGaN strip layer is introduced in the middle of the last quantum barrier (QB) which generated sufficient conduction band barrier height and effectively reduced the electron leakage into the p-GaN region. This resulted in improved IQE and output power of the proposed LED structure. In the next structure, an optimized-composition thin intrinsic AlxGa(1-x)N strip is introduced in the middle of each quantum barrier. Through this structure, it is demonstrated that with the progressively increased conduction band barrier height values constructively confine the electrons in the active region, and electron leakage into the p-region is effectively controlled. With this EBL-free proposed structure, the maximum IQE is improved by 72% and IQE droop is reduced by 333% as compared to the conventional AlGaN EBL LED structure. In the third structure, linearly graded polarization-controlled QBs are introduced instead of conventional QBs in the AlGaN UV LED structure. Due to the decreased lattice mismatch between the quantum well (QW) and the QB, this design resulted in a reduction of the electrostatic field in the QW area. Additionally, the suggested structure enhances carrier confinement in the active region and decreases electron leakage to the *p*-region due to a gradual increase in the effective conduction band barrier heights. Compared to the traditional EBL, the theoretical analysis showed that carrier transportation of the EBL-free deep UV LEDs was greatly improved due to higher radiative recombination, quantum efficiency, and output power. Overall, these studies provide crucial knowledge for creating new, high-performance deep UV LEDs for real-world applications.

This dissertation also shows how InGaN blue LED with a lattice-matched AlGaN last QB can outperform conventional LED in terms of IQE. This study demonstrates that polarization fields, effective potential barrier heights for carrier transportation, IQE, and the output power of InGaN multiple QW LEDs are significantly affected by the last QB. According to the numerical analysis, the integration of lattice-matched AlGaN layer as the last QB prevented the development of strong positive sheet polarization charges at the last QB/EBL interface. As a result, the suggested LED can support hole injection while considerably suppressing electron leakage. This innovative LED design may pave the way for the next wave of powerful light sources.

Next in the dissertation, the use of wide bandgap material-based RRAM is demonstrated for non-volatile memory applications. Systematic research has been done on multilevel switching in Ti/TiN/Ga_2O_3/Ti/Pt RRAM devices. For the first time, it is experimentally demonstrated that these RRAM devices, which have a reasonably high R_{off}/R_{on} ratio, can store multiple bits of data at lower compliance currents of 10 μA, 20 μA, and 50 μA. Additionally, an approach to control the formation of conducting filament is proposed, by integrating a thin SiN_x layer in the conventional SiO_2 RRAM device. At a very low compliance current of 10 nA, the proposed SiO_2/SiN_x RRAM device exhibited outstanding resistive switching (RS) properties, uniform current-voltage characteristics with concentrated SET and RESET voltages, exceptional stability, and a high R_{off}/R_{on} ($>10^3$). Additionally, the suggested RRAM exhibits multi-bit resistive switching behavior at extremely low operating currents, paving the path for low-power and high-density data storage applications.

11.1 Suggested Future Work

11.1.1 High Performance EBL Free AlGaN Nanowire UV LEDs

AlGaN Nanowire LEDs exhibit superior device performance due to several advantages in the nanowire structures, including effective strain relaxation in the lateral dimension, drastically reduced dislocations and polarization fields, and notably improved light extraction efficiency [85, 113, 251, 252]. However, nanowire LEDs still contain several challenges that may include electron overflow from the active region and poor hole injection that cause efficiency droop, and the efficiency droop is severe with a shorter emission wavelength in the UV regime [73, 79]. In this context, the aim is to address the electron leakage problem and provide efficient solutions for the same. Our research has proposed high performance EBL-free AlGaN UV LED structures in Chapters 4, 5, and 6, which can prevent electron leakage. Taking the advantage of the molecular beam epitaxy (MBE) system, and the team's expertise, epitaxial growth and device fabrication of high performance EBL-free AlGaN nanowire UV LEDs will be achievable. Integration of tunnel junction to supply holes into the active region will be additional benefit to improve IQE and output power further in these nanowire UV LEDs. The required wavelengths in the entire UV regime can be attained by accurately optimizing the III-nitride nanowires growth in terms of growth conditions, shape, size, arrangement, and elemental composition.

11.1.2 Improved RS Capabilities of RRAM Devices

Optimization of Top Electrode and Thickness of RS Layer: The barrier heights between conduction band (CB)/valence band (VB) and metal work function plays vital role in the carrier transportation of the device. With the wrong selection of TE, switching may not occur though the switching layer holds RS capability due to poor efficiency and flowing of very low currents (<1 pA) regardless of electrons or holes are being injected from top electrode (TE). RRAM devices (which are reported in Chapters 9 and 10) with different TE materials (Pt, Ag, Ti, Ru, Ni and Al) need be studied to reduce the forming voltage and improve R_{off}/R_{on} ratio. Next, it is also possible that forming voltages can be increased with the RS layer thickness. As the RS layer thickness is increased, a larger voltage needs to be applied to form the conduction paths. Therefore, it leads to have higher formation voltage in pristine devices, higher SET/RESET voltages thereafter. The RS layer thickness should be optimized to demonstrate desired SET/RESET voltages without compromising higher R_{off}/R_{on} ratios.

Incorporation of Quantum Dots to Improve RRAM Performance: It is important that RRAM should exhibit a continuous, uniform, and reliable change in its conductivity. Random and unstable RS behavior from cycle-to-cycle operation is one of the major problems that current RRAM devices are facing as it leads to a series of reliability problems. Mainly progressive RESET and abrupt RESET are observed in RRAM. The progressive RESET exhibit good uniformity but small switching window, while the abrupt RESET shows a large switching window but poor stability and high-power consumption. These challenges can be overcome by controlling the formation of conduction filament during the RRAM device operation. In recent years, researchers have shown great interest in embedding semiconductor quantum dots (QDs) into traditional electronic and photoelectric devices to obtain devices with better performance, low cost, and large-scale manufacture due to the breakthroughs in quantum effects (such as surface effects and quantum confined effects) [253]. The incorporation of zero-dimensional materials like quantum dots could be a potential solution to overcome this problem as quantum dots demonstrate tremendous application potential due to uniform size (distribution) and tunable bandgap [254]. The insertion of QDs between RS layer and electrodes would expands the switching window along with excellent readability and improve the uniformity and reliability, which demonstrates significant potential for nonvolatile memory application. Meanwhile, the design viewpoint of combining functional layers with quantum dots provides an excellent strategy for enhancing RRAM performance in the future. The above-mentioned proposed approaches would successfully mitigate the challenges such as non-uniformity from cycle-to-cycle operation, high current operations and high-power consumption, reliability issues in terms of endurance and retention in RRAM devices and provide a path to achieve highly uniform, stable, and ultra-lower power RRAM devices which can be utilized for real-world emerging applications.

REFERENCES

[1] J. Yan, J. Wang, Y. Zhang, P. Cong, L. Sun, Y. Tian, C. Zhao, and J. Li, "Algan-based deep-ultraviolet light-emitting diodes grown on high-quality aln template using movpe," *Journal of Crystal Growth*, vol. 414, pp. 254–257, 2015.

[2] J. Tsao, S. Chowdhury, M. Hollis, D. Jena, N. Johnson, K. Jones, R. Kaplar, S. Rajan, C. Van de Walle, E. Bellotti, *et al.*, "Ultrawide-bandgap semiconductors: research opportunities and challenges," *Advanced Electronic Materials*, vol. 4, no. 1, p. 1600501, 2018.

[3] F. Chen, X. Ji, and S. P. Lau, "Recent progress in group iii-nitride nanostructures: From materials to applications," *Materials Science and Engineering: R: Reports*, vol. 142, p. 100578, 2020.

[4] R. Singh, T. Lenka, D. Panda, R. Velpula, B. Jain, H. Bui, and H. Nguyen, "The dawn of Ga_2O_3 hemts for high power electronics-a review," *Materials Science in Semiconductor Processing*, vol. 119, p. 105216, 2020.

[5] W. Jeon, "Recent advances in the understanding of high-k dielectric materials deposited by atomic layer deposition for dynamic random-access memory capacitor applications," *Journal of Materials Research*, vol. 35, no. 7, pp. 775–794, 2020.

[6] I. Vurgaftman and J. n. Meyer, "Band parameters for nitrogen-containing semiconductors," *Journal of Applied Physics*, vol. 94, no. 6, pp. 3675–3696, 2003.

[7] I. Vurgaftman, J. á. Meyer, and L. á. Ram-Mohan, "Band parameters for iii–v compound semiconductors and their alloys," *Journal of Applied Physics*, vol. 89, no. 11, pp. 5815–5875, 2001.

[8] S. Strite and H. Morkoç, "Gan, aln, and inn: a review," *Journal of Vacuum Science and Technology B: Microelectronics and Nanometer Structures Processing, Measurement, and Phenomena*, vol. 10, no. 4, pp. 1237–1266, 1992.

[9] J. Wu, "When group-iii nitrides go infrared: New properties and perspectives," *Journal of Applied Physics*, vol. 106, no. 1, p. 5, 2009.

[10] J. Ibanez, R. Oliva, F. Manjón, A. Segura, T. Yamaguchi, Y. Nanishi, R. Cuscó, and L. Artús, "High-pressure lattice dynamics in wurtzite and rocksalt indium nitride investigated by means of raman spectroscopy," *Physical Review B*, vol. 88, no. 11, p. 115202, 2013.

[11] H. Xia, Q. Xia, and A. L. Ruoff, "High-pressure structure of gallium nitride: Wurtzite-to-rocksalt phase transition," *Physical Review B*, vol. 47, no. 19, p. 12925, 1993.

[12] T. Zhu and R. A. Oliver, “Unintentional doping in gan,” *Physical Chemistry Chemical Physics*, vol. 14, no. 27, pp. 9558–9573, 2012.

[13] J. Piprek, *Nitride semiconductor devices: principles and simulation.* Weinheim, Germany: John Wiley and Sons, 2007.

[14] P. T. Barletta, E. Acar Berkman, B. F. Moody, N. A. El-Masry, A. M. Emara, M. J. Reed, and S. Bedair, “Development of green, yellow, and amber light emitting diodes using ingan multiple quantum well structures,” *Applied Physics Letters*, vol. 90, no. 15, p. 151109, 2007.

[15] Y.-L. Chang, J. Wang, F. Li, and Z. Mi, “High efficiency green, yellow, and amber emission from ingan/gan dot-in-a-wire heterostructures on si (111),” *Applied Physics Letters*, vol. 96, no. 1, p. 013106, 2010.

[16] M. Kneissl, T. Kolbe, C. Chua, V. Kueller, N. Lobo, J. Stellmach, A. Knauer, H. Rodriguez, S. Einfeldt, Z. Yang, *et al.*, “Advances in group iii-nitride-based deep uv light-emitting diode technology,” *Semiconductor Science and Technology*, vol. 26, no. 1, p. 014036, 2010.

[17] S. Nakamura, M. Senoh, S.-i. Nagahama, N. Iwasa, T. Yamada, T. Matsushita, H. Kiyoku, Y. Sugimoto, T. Kozaki, H. Umemoto, *et al.*, “Ingan/gan/algan-based laser diodes with modulation-doped strained-layer superlattices grown on an epitaxially laterally overgrown gan substrate,” *Applied Physics Letters*, vol. 72, no. 2, pp. 211–213, 1998.

[18] S. Nakamura, M. Senoh, S.-i. Nagahama, N. Iwasa, T. Yamada, T. Matsushita, Y. Sugimoto, and H. Kiyoku, “Room-temperature continuous-wave operation of ingan multi-quantum-well structure laser diodes with a lifetime of 27 hours,” *Applied Physics Letters*, vol. 70, no. 11, pp. 1417–1419, 1997.

[19] O. Jani, I. Ferguson, C. Honsberg, and S. Kurtz, “Design and characterization of ga n/ in ga n solar cells,” *Applied Physics Letters*, vol. 91, no. 13, p. 132117, 2007.

[20] C. J. Neufeld, N. G. Toledo, S. C. Cruz, M. Iza, S. P. DenBaars, and U. K. Mishra, “High quantum efficiency ingan/gan solar cells with 2.95 ev band gap,” *Applied Physics Letters*, vol. 93, no. 14, p. 143502, 2008.

[21] E. Miyazaki, S. Itami, and T. Araki, “Using a light-emitting diode as a high-speed, wavelength selective photodetector,” *Review of Scientific Instruments*, vol. 69, no. 11, pp. 3751–3754, 1998.

[22] F. Binet, J. Duboz, E. Rosencher, F. Scholz, and V. Härle, “Mechanisms of recombination in gan photodetectors,” *Applied Physics Letters*, vol. 69, no. 9, pp. 1202–1204, 1996.

[23] R. Gaska, J. Yang, A. Osinsky, Q. Chen, M. A. Khan, A. Orlov, G. Snider, and M. Shur, “Electron transport in algan–gan heterostructures grown on 6h–sic substrates,” *Applied Physics Letters*, vol. 72, no. 6, pp. 707–709, 1998.

[24] S. Karmalkar and U. K. Mishra, “Enhancement of breakdown voltage in algan/gan high electron mobility transistors using a field plate,” *IEEE Transactions on Electron Devices*, vol. 48, no. 8, pp. 1515–1521, 2001.

[25] Y. Duan, H. Gao, J. Guo, M. Yang, Z. Yu, X. Shen, S. Wu, Y. Sun, X. Ma, and Y. Yang, “Effect of nitrogen capture ability of quantum dots on resistive switching characteristics of aln-based rram,” *Applied Physics Letters*, vol. 118, no. 1, p. 013501, 2021.

[26] H. J. Yun and B. J. Choi, “Effects of moisture and electrode material on aln-based resistive random access memory,” *Ceramics International*, vol. 45, no. 13, pp. 16311–16316, 2019.

[27] D. Manova, V. Dimitrova, W. Fukarek, and D. Karpuzov, “Investigation of dc-reactive magnetron-sputtered aln thin films by electron microprobe analysis, x-ray photoelectron spectroscopy and polarised infra-red reflection,” *Surface and Coatings Technology*, vol. 106, no. 2-3, pp. 205–208, 1998.

[28] Z.-L. Tseng, L.-C. Chen, W.-Y. Li, and S.-Y. Chu, “Resistive switching characteristics of sputtered aln thin films,” *Ceramics International*, vol. 42, no. 8, pp. 9496–9503, 2016.

[29] R. J. Aidam, O. Ambacher, E. Diwo, B.-J. Godejohann, L. Kirste, T. Lim, R. Quay, and P. Waltereit, “Mbe of iii-nitride semiconductors for electronic devices,” *Molecular Beam Epitaxy: Materials and Applications for Electronics and Optoelectronics*, p. 109, 2019.

[30] L. K. Ping, D. D. Berhanuddin, A. K. Mondal, P. S. Menon, and M. A. Mohamed, “Properties and perspectives of ultrawide bandgap ga2o3 in optoelectronic applications,” *Chinese Journal of Physics*, vol. 73, pp. 195–212, 2021.

[31] H. He, R. Orlando, M. A. Blanco, R. Pandey, E. Amzallag, I. Baraille, and M. Rérat, “First-principles study of the structural, electronic, and optical properties of Ga_2O_3 in its monoclinic and hexagonal phases,” *Physical Review B*, vol. 74, no. 19, p. 195123, 2006.

[32] D. Guo, Z. Wu, Y. An, P. Li, P. Wang, X. Chu, X. Guo, Y. Zhi, M. Lei, L. Li, *et al.*, “Unipolar resistive switching behavior of amorphous gallium oxide thin films for nonvolatile memory applications,” *Applied Physics Letters*, vol. 106, no. 4, p. 042105, 2015.

[33] V. Dubrovskii and N. Sibirev, “Growth thermodynamics of nanowires and its application to polytypism of zinc blende iii-v nanowires,” *Physical Review B*, vol. 77, no. 3, p. 035414, 2008.

[34] Z. Mi and C. Jagadish, *III-Nitride Semiconductor Optoelectronics.* London, UK: Academic Press, 2017.

[35] J. Li, D. Wang, and R. R. LaPierre, *Advances in III-V semiconductor nanowires and nanodevices.* Nijmegen, Netherlands: Bentham Science Publishers, 2011.

[36] W. Guo, M. Zhang, P. Bhattacharya, and J. Heo, "Auger recombination in iii-nitride nanowires and its effect on nanowire light-emitting diode characteristics," *Nano Letters*, vol. 11, no. 4, pp. 1434–1438, 2011.

[37] C. Wood and D. Jena, *Polarization effects in semiconductors: from ab initio theory to device applications.* New York, USA: Springer, 2007.

[38] C.-C. Pan, S. Tanaka, F. Wu, Y. Zhao, J. S. Speck, S. Nakamura, S. P. DenBaars, and D. Feezell, "High-power, low-efficiency-droop semipolar (2021) single-quantum-well blue light-emitting diodes," *Applied Physics Express*, vol. 5, no. 6, p. 062103, 2012.

[39] G. Li, W. Wang, W. Yang, Y. Lin, H. Wang, Z. Lin, and S. Zhou, "Gan-based light-emitting diodes on various substrates: a critical review," *Reports on Progress in Physics*, vol. 79, no. 5, p. 056501, 2016.

[40] J. Piprek, R. Farrell, S. DenBaars, and S. Nakamura, "Effects of built-in polarization on ingan-gan vertical-cavity surface-emitting lasers," *IEEE Photonics Technology Letters*, vol. 18, no. 1, pp. 7–9, 2005.

[41] J. Piprek, "Efficiency droop in nitride-based light-emitting diodes," *Physica Status Solidi (a)*, vol. 207, no. 10, pp. 2217–2225, 2010.

[42] H. P. T. Nguyen, K. Cui, S. Zhang, M. Djavid, A. Korinek, G. A. Botton, and Z. Mi, "Controlling electron overflow in phosphor-free ingan/gan nanowire white light-emitting diodes," *Nano Letters*, vol. 12, no. 3, pp. 1317–1323, 2012.

[43] J. Liu, J.-H. Ryou, R. Dupuis, J. Han, G. Shen, and H. Wang, "Barrier effect on hole transport and carrier distribution in in ga n/ ga n multiple quantum well visible light-emitting diodes," *Applied Physics Letters*, vol. 93, no. 2, p. 021102, 2008.

[44] K. Nam, M. Nakarmi, J. Li, J. Lin, and H. Jiang, "Mg acceptor level in aln probed by deep ultraviolet photoluminescence," *Applied Physics Letters*, vol. 83, no. 5, pp. 878–880, 2003.

[45] C. Chu, K. Tian, J. Che, H. Shao, J. Kou, Y. Zhang, Y. Li, M. Wang, Y. Zhu, and Z.-H. Zhang, "On the origin of enhanced hole injection for algan-based deep ultraviolet light-emitting diodes with aln insertion layer in p-electron blocking layer," *Optics Express*, vol. 27, no. 12, pp. A620–A628, 2019.

[46] R. T. Velpula, B. Jain, H. Q. T. Bui, F. M. Shakiba, J. Jude, M. Tumuna, H.-D. Nguyen, T. R. Lenka, and H. P. T. Nguyen, "Improving carrier transport in algan deep-ultraviolet light-emitting diodes using a strip-in-a-barrier structure," *Applied Optics*, vol. 59, no. 17, pp. 5276–5281, 2020.

[47] M. Yamada, T. Mitani, Y. Narukawa, S. Shioji, I. Niki, S. Sonobe, K. Deguchi, M. Sano, and T. Mukai, "Ingan-based near-ultraviolet and blue-light-emitting diodes with high external quantum efficiency using a patterned sapphire substrate and a mesh electrode," *Japanese Journal of Applied Physics*, vol. 41, no. 12B, p. L1431, 2002.

[48] T. Kolbe, A. Knauer, C. Chua, Z. Yang, S. Einfeldt, P. Vogt, N. M. Johnson, M. Weyers, and M. Kneissl, "Optical polarization characteristics of ultraviolet (in)(al) gan multiple quantum well light emitting diodes," *Applied Physics Letters*, vol. 97, no. 17, p. 171105, 2010.

[49] J. Shakya, K. Knabe, K. Kim, J. Li, J. Lin, and H. Jiang, "Polarization of iii-nitride blue and ultraviolet light-emitting diodes," *Applied Physics Letters*, vol. 86, no. 9, p. 091107, 2005.

[50] B. Jain, R. T. Velpula, M. Tumuna, H. Q. T. Bui, J. Jude, T. T. Pham, A. V. Hoang, R. Wang, H. P. T. Nguyen, *et al.*, "Enhancing the light extraction efficiency of alinn nanowire ultraviolet light-emitting diodes with photonic crystal structures," *Optics Express*, vol. 28, no. 15, pp. 22908–22918, 2020.

[51] M. Patel, B. Jain, R. T. Velpula, and H. P. T. Nguyen, "Effect of hfo2 passivation layer on light extraction efficiency of alinn nanowire ultraviolet light-emitting diodes," *ECS Transactions*, vol. 102, no. 3, p. 35, 2021.

[52] D. Li, K. Jiang, X. Sun, and C. Guo, "Algan photonics: recent advances in materials and ultraviolet devices," *Advances in Optics and Photonics*, vol. 10, no. 1, pp. 43–110, 2018.

[53] M. Kneissl, T.-Y. Seong, J. Han, and H. Amano, "The emergence and prospects of deep-ultraviolet light-emitting diode technologies," *Nature Photonics*, vol. 13, no. 4, pp. 233–244, 2019.

[54] M. A. Banas, M. H. Crawford, D. S. Ruby, M. P. Ross, J. S. Nelson, A. A. Allerman, and R. Boucher, "Final ldrd report: ultraviolet water purification systems for rural environments and mobile applications.," tech. rep., Sandia National Laboratories (SNL), Albuquerque, NM, and Livermore, CA, 2005.

[55] M. Würtele, T. Kolbe, M. Lipsz, A. Külberg, M. Weyers, M. Kneissl, and M. Jekel, "Application of gan-based ultraviolet-c light emitting diodes–uv leds–for water disinfection," *Water Research*, vol. 45, no. 3, pp. 1481–1489, 2011.

[56] V. Landry, P. Blanchet, G. Boivin, J.-F. Bouffard, and M. Vlad, "Uv-led curing efficiency of wood coatings," *Coatings*, vol. 5, no. 4, pp. 1019–1033, 2015.

[57] M. Oelgemoeller, "Highlights of photochemical reactions in microflow reactors," *Chemical Engineering and Technology*, vol. 35, no. 7, pp. 1144–1152, 2012.

[58] K. C. Smith, "Laser (and led) therapy is phototherapy," *Photomedicine and Laser Therapy*, vol. 23, no. 1, pp. 78–80, 2005.

[59] F. Mehnke, M. Guttmann, J. Enslin, C. Kuhn, C. Reich, J. Jordan, S. Kapanke, A. Knauer, M. Lapeyrade, U. Zeimer, *et al.*, “Gas sensing of nitrogen oxide utilizing spectrally pure deep uv leds,” *IEEE Journal of Selected Topics in Quantum Electronics*, vol. 23, no. 2, pp. 29–36, 2016.

[60] P. M. Lytvyn, A. V. Kuchuk, Y. I. Mazur, C. Li, M. E. Ware, Z. M. Wang, V. P. Kladko, A. E. Belyaev, and G. J. Salamo, “Polarization effects in graded algan nanolayers revealed by current-sensing and kelvin probe microscopy,” *ACS Applied Materials and Interfaces*, vol. 10, no. 7, pp. 6755–6763, 2018.

[61] A. N. Alimova, A. Katz, V. Sriramoju, Y. Budansky, A. A. Bykov, R. Zelikovitch, and R. R. Alfano, “Hybrid phosphorescence and fluorescence native spectroscopy for breast cancer detection,” *Journal of Biomedical Optics*, vol. 12, no. 1, p. 014004, 2007.

[62] Y. Muramoto, M. Kimura, and S. Nouda, “Development and future of ultraviolet light-emitting diodes: Uv-led will replace the uv lamp,” *Semiconductor Science and Technology*, vol. 29, no. 8, p. 084004, 2014.

[63] H. Hirayama, Y. Tsukada, T. Maeda, and N. Kamata, “Marked enhancement in the efficiency of deep-ultraviolet algan light-emitting diodes by using a multiquantum-barrier electron blocking layer,” *Applied Physics Express*, vol. 3, no. 3, p. 031002, 2010.

[64] M. Z. Baten, S. Alam, B. Sikder, and A. Aziz, “Iii-nitride light-emitting devices,” in *Photonics*, vol. 8, p. 430, MDPI, 2021.

[65] T. F. Kent, S. D. Carnevale, A. Sarwar, P. J. Phillips, R. F. Klie, and R. C. Myers, “Deep ultraviolet emitting polarization induced nanowire light emitting diodes with alxga1- xn active regions,” *Nanotechnology*, vol. 25, no. 45, p. 455201, 2014.

[66] S. Zhao, M. Djavid, and Z. Mi, “Surface emitting, high efficiency near-vacuum ultraviolet light source with aluminum nitride nanowires monolithically grown on silicon,” *Nano Letters*, vol. 15, no. 10, pp. 7006–7009, 2015.

[67] A. G. Sarwar, B. J. May, M. F. Chisholm, G. J. Duscher, and R. C. Myers, “Ultrathin gan quantum disk nanowire leds with sub-250 nm electroluminescence,” *Nanoscale*, vol. 8, no. 15, pp. 8024–8032, 2016.

[68] D. Liu, S. J. Cho, J. Park, J. Gong, J.-H. Seo, R. Dalmau, D. Zhao, K. Kim, M. Kim, A. R. Kalapala, *et al.*, “226 nm algan/aln uv leds using p-type si for hole injection and uv reflection,” *Applied Physics Letters*, vol. 113, no. 1, p. 011111, 2018.

[69] D. Liu, S. J. Cho, J. Park, J.-H. Seo, R. Dalmau, D. Zhao, K. Kim, J. Gong, M. Kim, I.-K. Lee, *et al.*, “229 nm uv leds on aluminum nitride single crystal substrates using p-type silicon for increased hole injection,” *Applied Physics Letters*, vol. 112, no. 8, p. 081101, 2018.

[70] S. Zhao, S. Sadaf, S. Vanka, Y. Wang, R. Rashid, and Z. Mi, "Sub-milliwatt algan nanowire tunnel junction deep ultraviolet light emitting diodes on silicon operating at 242 nm," *Applied Physics Letters*, vol. 109, no. 20, p. 201106, 2016.

[71] Y. Zhang, S. Krishnamoorthy, F. Akyol, J. M. Johnson, A. A. Allerman, M. W. Moseley, A. M. Armstrong, J. Hwang, and S. Rajan, "Reflective metal/semiconductor tunnel junctions for hole injection in algan uv leds," *Applied Physics Letters*, vol. 111, no. 5, p. 051104, 2017.

[72] Y. Zhang, Z. Jamal-Eddine, F. Akyol, S. Bajaj, J. M. Johnson, G. Calderon, A. A. Allerman, M. W. Moseley, A. M. Armstrong, J. Hwang, *et al.*, "Tunnel-injected sub 290 nm ultra-violet light emitting diodes with 2.8% external quantum efficiency," *Applied Physics Letters*, vol. 112, no. 7, p. 071107, 2018.

[73] S. Zhao, S. Woo, S. Sadaf, Y. Wu, A. Pofelski, D. Laleyan, R. Rashid, Y. Wang, G. Botton, and Z. Mi, "Molecular beam epitaxy growth of al-rich algan nanowires for deep ultraviolet optoelectronics," *Apl Materials*, vol. 4, no. 8, p. 086115, 2016.

[74] D. A. Miller, D. Chemla, T. Damen, A. Gossard, W. Wiegmann, T. Wood, and C. Burrus, "Band-edge electroabsorption in quantum well structures: The quantum-confined stark effect," *Physical Review Letters*, vol. 53, no. 22, p. 2173, 1984.

[75] J. S. Im, H. Kollmer, J. Off, A. Sohmer, F. Scholz, and A. Hangleiter, "Reduction of oscillator strength due to piezoelectric fields in g a n/a l x ga 1- x n quantum wells," *Physical Review B*, vol. 57, no. 16, p. R9435, 1998.

[76] Q. Wang, H. Nguyen, K. Cui, and Z. Mi, "High efficiency ultraviolet emission from alxga1- xn core-shell nanowire heterostructures grown on si (111) by molecular beam epitaxy," *Applied Physics Letters*, vol. 101, no. 4, p. 043115, 2012.

[77] Q. Wang, A. Connie, H. Nguyen, M. Kibria, S. Zhao, S. Sharif, I. Shih, and Z. Mi, "Highly efficient, spectrally pure 340 nm ultraviolet emission from alxga1-xn nanowire based light emitting diodes," *Nanotechnology*, vol. 24, no. 34, p. 345201, 2013.

[78] P. Dong, J. Yan, Y. Zhang, J. Wang, C. Geng, H. Zheng, X. Wei, Q. Yan, and J. Li, "Optical properties of nanopillar algan/gan mqws for ultraviolet light-emitting diodes," *Optics Express*, vol. 22, no. 102, pp. A320–A327, 2014.

[79] X. Hai, R. Rashid, S. Sadaf, Z. Mi, and S. Zhao, "Effect of low hole mobility on the efficiency droop of algan nanowire deep ultraviolet light emitting diodes," *Applied Physics Letters*, vol. 114, no. 10, p. 101104, 2019.

[80] S.-H. Han, D.-Y. Lee, S.-J. Lee, C.-Y. Cho, M.-K. Kwon, S. Lee, D. Noh, D.-J. Kim, Y. C. Kim, and S.-J. Park, "Effect of electron blocking layer on efficiency droop

in ingan/gan multiple quantum well light-emitting diodes," *Applied Physics Letters*, vol. 94, no. 23, p. 231123, 2009.

[81] S. Choi, H. J. Kim, S.-S. Kim, J. Liu, J. Kim, J.-H. Ryou, R. D. Dupuis, A. M. Fischer, and F. A. Ponce, "Improvement of peak quantum efficiency and efficiency droop in iii-nitride visible light-emitting diodes with an inaln electron-blocking layer," *Applied Physics Letters*, vol. 96, no. 22, p. 221105, 2010.

[82] C. Wang, C. Ke, C. Lee, S. Chang, W. Chang, J. Li, Z. Li, H. Yang, H.-C. Kuo, T. Lu, *et al.*, "Hole injection and efficiency droop improvement in ingan/gan light-emitting diodes by band-engineered electron blocking layer," *Applied Physics Letters*, vol. 97, no. 26, p. 261103, 2010.

[83] N. Wang, Y. A. Yin, B. Zhao, and T. Mei, "Performance analysis of gan-based light-emitting diodes with lattice-matched ingan/alinn/ingan quantum-well barriers," *Journal of Display Technology*, vol. 11, no. 12, pp. 1056–1060, 2015.

[84] S. Choi, M.-H. Ji, J. Kim, H. Jin Kim, M. M. Satter, P. Yoder, J.-H. Ryou, R. D. Dupuis, A. M. Fischer, and F. A. Ponce, "Efficiency droop due to electron spill-over and limited hole injection in iii-nitride visible light-emitting diodes employing lattice-matched inaln electron blocking layers," *Applied Physics Letters*, vol. 101, no. 16, p. 161110, 2012.

[85] S. Zhao, A. Connie, M. Dastjerdi, X. Kong, Q. Wang, M. Djavid, S. Sadaf, X. Liu, I. Shih, H. Guo, *et al.*, "Aluminum nitride nanowire light emitting diodes: Breaking the fundamental bottleneck of deep ultraviolet light sources," *Scientific Reports*, vol. 5, no. 1, pp. 1–5, 2015.

[86] N. Khan, N. Nepal, A. Sedhain, J. Lin, and H. Jiang, "Mg acceptor level in inn epilayers probed by photoluminescence," *Applied Physics Letters*, vol. 91, no. 1, p. 012101, 2007.

[87] M. Nakarmi, N. Nepal, J. Lin, and H. Jiang, "Photoluminescence studies of impurity transitions in mg-doped algan alloys," *Applied Physics Letters*, vol. 94, no. 9, p. 091903, 2009.

[88] J.-F. Carlin and M. Ilegems, "High-quality alinn for high index contrast bragg mirrors lattice matched to gan," *Applied Physics Letters*, vol. 83, no. 4, pp. 668–670, 2003.

[89] K. Lorenz, N. Franco, E. Alves, I. Watson, R. Martin, and K. O'donnell, "Anomalous ion channeling in alinn/gan bilayers: determination of the strain state," *Physical Review Letters*, vol. 97, no. 8, p. 085501, 2006.

[90] C.-K. Tan, W. Sun, D. Borovac, and N. Tansu, "Large optical gain alinn-delta-gan quantum well for deep ultraviolet emitters," *Scientific Reports*, vol. 6, no. 1, pp. 1–7, 2016.

[91] C. Durand, C. Bougerol, J.-F. Carlin, G. Rossbach, F. Godel, J. Eymery, P.-H. Jouneau, A. Mukhtarova, R. Butté, and N. Grandjean, "M-plane gan/inaln multiple quantum wells in core–shell wire structure for uv emission," *ACS Photonics*, vol. 1, no. 1, pp. 38–46, 2014.

[92] D. Fu, R. Zhang, B. Liu, Z. Xie, X. Xiu, H. Lu, Y. Zheng, and G. Edwards, "Exploring optimal uv emission windows for algan and alinn alloys grown on different templates," *Physica Status Solidi (b)*, vol. 248, no. 12, pp. 2816–2820, 2011.

[93] S. Nicolay, J.-F. Carlin, E. Feltin, R. Butté, M. Mosca, N. Grandjean, M. Ilegems, M. Tchernycheva, L. Nevou, and F. Julien, "Midinfrared intersubband absorption in lattice-matched al in n/ ga n multiple quantum wells," *Applied Physics Letters*, vol. 87, no. 11, p. 111106, 2005.

[94] J. Dorsaz, J.-F. Carlin, S. Gradecak, and M. Ilegems, "Progress in alinn–gan bragg reflectors: application to a microcavity light emitting diode," *Journal of Applied Physics*, vol. 97, no. 8, p. 084505, 2005.

[95] E. Feltin, G. Christmann, J. Dorsaz, A. Castiglia, J.-F. Carlin, R. Butté, N. Grandjean, S. Christopoulos, G. B. H. von Högersthal, A. Grundy, *et al.*, "Blue lasing at room temperature in an optically pumped lattice-matched alinn/gan vcsel structure," *Electronics Letters*, vol. 43, no. 17, pp. 924–926, 2007.

[96] M. Gonschorek, J.-F. Carlin, E. Feltin, M. Py, and N. Grandjean, "High electron mobility lattice-matched al in n/ ga n field-effect transistor heterostructures," *Applied Physics Letters*, vol. 89, no. 6, p. 062106, 2006.

[97] S. Chuang and C. Chang, "k · p method for strained wurtzite semiconductors," *Physical Review B*, vol. 54, no. 4, p. 2491, 1996.

[98] H. P. T. Nguyen, M. Djavid, S. Y. Woo, X. Liu, A. T. Connie, S. Sadaf, Q. Wang, G. A. Botton, I. Shih, and Z. Mi, "Engineering the carrier dynamics of ingan nanowire white light-emitting diodes by distributed p-algan electron blocking layers," *Scientific Reports*, vol. 5, no. 1, pp. 1–7, 2015.

[99] M. M. Satter, H.-J. Kim, Z. Lochner, J.-H. Ryou, S.-C. Shen, R. D. Dupuis, and P. D. Yoder, "Design and analysis of 250-nm alinn laser diodes on aln substrates using tapered electron blocking layers," *IEEE Journal of Quantum Electronics*, vol. 48, no. 5, pp. 703–711, 2012.

[100] Y.-K. Kuo and Y.-A. Chang, "Effects of electronic current overflow and inhomogeneous carrier distribution on ingan quantum-well laser performance," *IEEE Journal of Quantum Electronics*, vol. 40, no. 5, pp. 437–444, 2004.

[101] J.-Y. Chang and Y.-K. Kuo, "Simulation of blue ingan quantum-well lasers," *Journal of Applied Physics*, vol. 93, no. 9, pp. 4992–4998, 2003.

[102] X. Chen, C. Ji, Y. Xiang, X. Kang, B. Shen, and T. Yu, “Angular distribution of polarized light and its effect on light extraction efficiency in algan deep-ultraviolet light-emitting diodes,” *Optics Express*, vol. 24, no. 10, pp. A935–A942, 2016.

[103] T. Zywietz, J. Neugebauer, and M. Scheffler, “Adatom diffusion at gan (0001) and (0001) surfaces,” *Applied Physics Letters*, vol. 73, no. 4, pp. 487–489, 1998.

[104] S. Choi, F. Wu, R. Shivaraman, E. C. Young, and J. S. Speck, “Observation of columnar microstructure in lattice-matched inaln/gan grown by plasma assisted molecular beam epitaxy,” *Applied Physics Letters*, vol. 100, no. 23, p. 232102, 2012.

[105] L. Zhou, D. J. Smith, M. R. McCartney, D. Katzer, and D. Storm, “Observation of vertical honeycomb structure in inaln/ gan heterostructures due to lateral phase separation,” *Applied Physics Letters*, vol. 90, no. 8, p. 081917, 2007.

[106] R. Butté, J. Carlin, E. Feltin, M. Gonschorek, S. Nicolay, G. Christmann, D. Simeonov, A. Castiglia, J. Dorsaz, H. Buehlmann, *et al.*, “Current status of alinn layers lattice-matched to gan for photonics and electronics,” *Journal of Physics D: Applied Physics*, vol. 40, no. 20, p. 6328, 2007.

[107] S. W. Kaun, E. Ahmadi, B. Mazumder, F. Wu, E. C. Kyle, P. G. Burke, U. K. Mishra, and J. S. Speck, “Gan-based high-electron-mobility transistor structures with homogeneous lattice-matched inaln barriers grown by plasma-assisted molecular beam epitaxy,” *Semiconductor Science and Technology*, vol. 29, no. 4, p. 045011, 2014.

[108] E. C. Kyle, S. W. Kaun, F. Wu, B. Bonef, and J. S. Speck, “High indium content homogenous inaln layers grown by plasma-assisted molecular beam epitaxy,” *Journal of Crystal Growth*, vol. 454, pp. 164–172, 2016.

[109] W. Guo, M. Zhang, A. Banerjee, and P. Bhattacharya, “Catalyst-free ingan/gan nanowire light emitting diodes grown on (001) silicon by molecular beam epitaxy,” *Nano Letters*, vol. 10, no. 9, pp. 3355–3359, 2010.

[110] S. Zhao, H. P. Nguyen, M. G. Kibria, and Z. Mi, “Iii-nitride nanowire optoelectronics,” *Progress in Quantum Electronics*, vol. 44, pp. 14–68, 2015.

[111] C. Hahn, Z. Zhang, A. Fu, C. H. Wu, Y. J. Hwang, D. J. Gargas, and P. Yang, “Epitaxial growth of ingan nanowire arrays for light emitting diodes,” *ACS Nano*, vol. 5, no. 5, pp. 3970–3976, 2011.

[112] S. Zhao, S. Fathololoumi, K. Bevan, D. Liu, M. Kibria, Q. Li, G. Wang, H. Guo, and Z. Mi, “Tuning the surface charge properties of epitaxial inn nanowires,” *Nano Letters*, vol. 12, no. 6, pp. 2877–2882, 2012.

[113] M. Djavid and Z. Mi, "Enhancing the light extraction efficiency of algan deep ultraviolet light emitting diodes by using nanowire structures," *Applied Physics Letters*, vol. 108, no. 5, p. 051102, 2016.

[114] Y.-H. Ra, R. T. Rashid, X. Liu, J. Lee, and Z. Mi, "Scalable nanowire photonic crystals: Molding the light emission of ingan," *Advanced Functional Materials*, vol. 27, no. 38, p. 1702364, 2017.

[115] P. Du, L. Rao, Y. Liu, Z. Cheng, *et al.*, "Enhancing the light extraction efficiency of algan led with nanowire photonic crystal and graphene transparent electrode," *Superlattices and Microstructures*, vol. 133, p. 106216, 2019.

[116] M. Djavid, *High efficiency nanowire-based phosphor-free white and deep ultraviolet light sources.* Ph.D. Dissertation, McGill University, Montreal, Quebec, Canada, 2016.

[117] H. P. T. Nguyen, S. Zhang, K. Cui, X. Han, S. Fathololoumi, M. Couillard, G. Botton, and Z. Mi, "p-type modulation doped ingan/gan dot-in-a-wire white-light-emitting diodes monolithically grown on si (111)," *Nano Letters*, vol. 11, no. 5, pp. 1919–1924, 2011.

[118] H. P. T. Nguyen, S. Zhang, A. T. Connie, M. G. Kibria, Q. Wang, I. Shih, and Z. Mi, "Breaking the carrier injection bottleneck of phosphor-free nanowire white light-emitting diodes," *Nano Letters*, vol. 13, no. 11, pp. 5437–5442, 2013.

[119] K. Li, X. Liu, Q. Wang, S. Zhao, and Z. Mi, "Ultralow-threshold electrically injected algan nanowire ultraviolet lasers on si operating at low temperature," *Nature Nanotechnology*, vol. 10, no. 2, pp. 140–144, 2015.

[120] M. A. Khan, N. Maeda, M. Jo, Y. Akamatsu, R. Tanabe, Y. Yamada, and H. Hirayama, "13 mw operation of a 295–310 nm algan uv-b led with a p-algan transparent contact layer for real world applications," *Journal of Materials Chemistry C*, vol. 7, no. 1, pp. 143–152, 2019.

[121] D. Priante, B. Janjua, A. Prabaswara, R. C. Subedi, R. T. Elafandy, S. Lopatin, D. H. Anjum, C. Zhao, T. K. Ng, and B. S. Ooi, "Highly uniform ultraviolet-a quantum-confined algan nanowire leds on metal/silicon with a tan interlayer," *Optical Materials Express*, vol. 7, no. 12, pp. 4214–4224, 2017.

[122] S. Sadaf, S. Zhao, Y. Wu, Y.-H. Ra, X. Liu, S. Vanka, and Z. Mi, "An algan core–shell tunnel junction nanowire light-emitting diode operating in the ultraviolet-c band," *Nano Letters*, vol. 17, no. 2, pp. 1212–1218, 2017.

[123] T. A. Growden, W. Zhang, E. R. Brown, D. F. Storm, D. J. Meyer, and P. R. Berger, "Near-uv electroluminescence in unipolar-doped, bipolar-tunneling gan/aln heterostructures," *Light: Science and Applications*, vol. 7, no. 2, pp. 17150–17150, 2018.

[124] H.-Y. Ryu, I.-G. Choi, H.-S. Choi, and J.-I. Shim, "Investigation of light extraction efficiency in algan deep-ultraviolet light-emitting diodes," *Applied Physics Express*, vol. 6, no. 6, p. 062101, 2013.

[125] K. H. Lee, H. J. Park, S. H. Kim, M. Asadirad, Y.-T. Moon, J. S. Kwak, and J.-H. Ryou, "Light-extraction efficiency control in algan-based deep-ultraviolet flip-chip light-emitting diodes: a comparison to ingan-based visible flip-chip light-emitting diodes," *Optics Express*, vol. 23, no. 16, pp. 20340–20349, 2015.

[126] P. Zhao, L. Han, M. R. McGoogan, and H. Zhao, "Analysis of tm mode light extraction efficiency enhancement for deep ultraviolet algan quantum wells light-emitting diodes with iii-nitride micro-domes," *Optical Materials Express*, vol. 2, no. 10, pp. 1397–1406, 2012.

[127] A. David, *High-efficiency GaN-based light-emitting diodes: light extraction by photonic crystals and microcavities.* PhD thesis, Ecole Polytechnique X, Palaiseau, France, 2006.

[128] J. Cho, E. F. Schubert, and J. K. Kim, "Efficiency droop in light-emitting diodes: Challenges and countermeasures," *Laser and Photonics Reviews*, vol. 7, no. 3, pp. 408–421, 2013.

[129] H. Hirayama, S. Fujikawa, N. Noguchi, J. Norimatsu, T. Takano, K. Tsubaki, and N. Kamata, "222–282 nm algan and inalgan-based deep-uv leds fabricated on high-quality aln on sapphire," *Physica Status Solidi (a)*, vol. 206, no. 6, pp. 1176–1182, 2009.

[130] Z.-H. Zhang, S.-W. Huang Chen, Y. Zhang, L. Li, S.-W. Wang, K. Tian, C. Chu, M. Fang, H.-C. Kuo, and W. Bi, "Hole transport manipulation to improve the hole injection for deep ultraviolet light-emitting diodes," *A Photonics*, vol. 4, no. 7, pp. 1846–1850, 2017.

[131] Z.-H. Zhang, J. Kou, S.-W. H. Chen, H. Shao, J. Che, C. Chu, K. Tian, Y. Zhang, W. Bi, and H.-C. Kuo, "Increasing the hole energy by grading the alloy composition of the p-type electron blocking layer for very high-performance deep ultraviolet light-emitting diodes," *Photonics Research*, vol. 7, no. 4, pp. B1–B6, 2019.

[132] X. Fan, H. Sun, X. Li, H. Sun, C. Zhang, Z. Zhang, and Z. Guo, "Efficiency improvements in algan-based deep ultraviolet light-emitting diodes using inverted-v-shaped graded al composition electron blocking layer," *Superlattices and Microstructures*, vol. 88, pp. 467–473, 2015.

[133] J.-Y. Chang, H.-T. Chang, Y.-H. Shih, F.-M. Chen, M.-F. Huang, and Y.-K. Kuo, "Efficient carrier confinement in deep-ultraviolet light-emitting diodes with composition-graded configuration," *IEEE Transactions on Electron Devices*, vol. 64, no. 12, pp. 4980–4984, 2017.

[134] Z.-H. Zhang, S.-W. Huang Chen, C. Chu, K. Tian, M. Fang, Y. Zhang, W. Bi, and H.-C. Kuo, “Nearly efficiency-droop-free algan-based ultraviolet light-emitting diodes with a specifically designed superlattice p-type electron blocking layer for high mg doping efficiency,” *Nanoscale Research Letters*, vol. 13, no. 1, pp. 1–7, 2018.

[135] T. Al Tahtamouni, J. Lin, and H. Jiang, “Effects of mg-doped aln/algan superlattices on properties of p-gan contact layer and performance of deep ultraviolet light emitting diodes,” *AIP Advances*, vol. 4, no. 4, p. 047122, 2014.

[136] B. So, J. Kim, T. Kwak, T. Kim, J. Lee, U. Choi, and O. Nam, “Improved carrier injection of algan-based deep ultraviolet light emitting diodes with graded superlattice electron blocking layers,” *RSC Advances*, vol. 8, no. 62, pp. 35528–35533, 2018.

[137] B. Jain, R. T. Velpula, S. Velpula, H.-D. Nguyen, and H. P. T. Nguyen, “Enhanced hole transport in algan deep ultraviolet light-emitting diodes using a double-sided step graded superlattice electron blocking layer,” *Journal of the Optical Society of America B*, vol. 37, no. 9, pp. 2564–2569, 2020.

[138] J. Piprek and Z. Simon Li, “Sensitivity analysis of electron leakage in iii-nitride light-emitting diodes,” *Applied Physics Letters*, vol. 102, no. 13, p. 131103, 2013.

[139] V. Fiorentini, F. Bernardini, and O. Ambacher, “Evidence for nonlinear macroscopic polarization in iii–v nitride alloy heterostructures,” *Applied Physics Letters*, vol. 80, no. 7, pp. 1204–1206, 2002.

[140] C. Weisbuch, M. Piccardo, L. Martinelli, J. Iveland, J. Peretti, and J. S. Speck, “The efficiency challenge of nitride light-emitting diodes for lighting,” *Physica Status Solidi (a)*, vol. 212, no. 5, pp. 899–913, 2015.

[141] C. Coughlan, S. Schulz, M. A. Caro, and E. P. O’Reilly, “Band gap bowing and optical polarization switching in al ga n alloys,” *Physica Status Solidi (b)*, vol. 252, no. 5, pp. 879–884, 2015.

[142] J. Yun, J.-I. Shim, and H. Hirayama, “Analysis of efficiency droop in 280-nm algan multiple-quantum-well light-emitting diodes based on carrier rate equation,” *Applied Physics Express*, vol. 8, no. 2, p. 022104, 2015.

[143] Y. P. Varshni, “Temperature dependence of the energy gap in semiconductors,” *Physica*, vol. 34, no. 1, pp. 149–154, 1967.

[144] D. M. Caughey and R. Thomas, “Carrier mobilities in silicon empirically related to doping and field,” *Proceedings of the IEEE*, vol. 55, no. 12, pp. 2192–2193, 1967.

[145] Y. A. Yin, N. Wang, G. Fan, and Y. Zhang, “Investigation of algan-based deep-ultraviolet light-emitting diodes with composition-varying algan multilayer barriers,” *Superlattices and Microstructures*, vol. 76, pp. 149–155, 2014.

[146] B. Jain, R. T. Velpula, H. Q. T. Bui, H.-D. Nguyen, T. R. Lenka, T. K. Nguyen, and H. P. T. Nguyen, “High performance electron blocking layer-free ingan/gan nanowire white-light-emitting diodes,” *Optics Express*, vol. 28, no. 1, pp. 665–675, 2020.

[147] X. Ji, J. Yan, Y. Guo, L. Sun, T. Wei, Y. Zhang, J. Wang, F. Yang, and J. Li, “Tailoring of energy band in electron-blocking structure enhancing the efficiency of algan-based deep ultraviolet light-emitting diodes,” *IEEE Photonics Journal*, vol. 8, no. 3, pp. 1–7, 2016.

[148] Z.-H. Zhang, W. Liu, S. T. Tan, Z. Ju, Y. Ji, Z. Kyaw, X. Zhang, N. Hasanov, B. Zhu, S. Lu, *et al.*, “On the mechanisms of ingan electron cooler in ingan/gan light-emitting diodes,” *Optics Express*, vol. 22, no. 103, pp. A779–A789, 2014.

[149] O. Ambacher, R. Dimitrov, M. Stutzmann, B. Foutz, M. Murphy, J. Smart, J. Shealy, N. Weimann, K. Chu, M. Chumbes, *et al.*, “Role of spontaneous and piezoelectric polarization induced effects in group-iii nitride based heterostructures and devices,” *physica status solidi (b)*, vol. 216, no. 1, pp. 381–389, 1999.

[150] D. Jena, S. Heikman, D. Green, D. Buttari, R. Coffie, H. Xing, S. Keller, S. DenBaars, J. S. Speck, U. K. Mishra, *et al.*, “Realization of wide electron slabs by polarization bulk doping in graded iii–v nitride semiconductor alloys,” *Applied physics letters*, vol. 81, no. 23, pp. 4395–4397, 2002.

[151] W. Banerjee, “Challenges and applications of emerging nonvolatile memory devices,” *Electronics*, vol. 9, no. 6, p. 1029, 2020.

[152] F. Pan, S. Gao, C. Chen, C. Song, and F. Zeng, “Recent progress in resistive random access memories: Materials, switching mechanisms, and performance,” *Materials Science and Engineering: R: Reports*, vol. 83, pp. 1–59, 2014.

[153] J. A. Hutchby, R. Cavin, V. Zhirnov, J. E. Brewer, and G. Bourianoff, “Emerging nanoscale memory and logic devices: A critical assessment,” *Computer*, vol. 41, no. 5, pp. 28–32, 2008.

[154] H.-S. P. Wong, H.-Y. Lee, S. Yu, Y.-S. Chen, Y. Wu, P.-S. Chen, B. Lee, F. T. Chen, and M.-J. Tsai, “Metal–oxide rram,” *Proceedings of the IEEE*, vol. 100, no. 6, pp. 1951–1970, 2012.

[155] T. Hickmott, “Low-frequency negative resistance in thin anodic oxide films,” *Journal of Applied Physics*, vol. 33, no. 9, pp. 2669–2682, 1962.

[156] J. Gibbons and W. Beadle, “Switching properties of thin nio films,” *Solid-State Electronics*, vol. 7, no. 11, pp. 785–790, 1964.

[157] J. Kim, M. Kang, J. Jeon, and H. Shin, “Fringe capacitance modeling in nanoplate mosfet using conformal mapping,” *IEEE Transactions on Electron Devices*, vol. 66, no. 5, pp. 2446–2449, 2019.

[158] W. Hiatt and T. Hickmott, “Bistable switching in niobium oxide diodes,” *Applied Physics Letters*, vol. 6, no. 6, pp. 106–108, 1965.

[159] I. Baek, M. Lee, S. Seo, M. Lee, D. Seo, D.-S. Suh, J. Park, S. Park, H. Kim, I. Yoo, *et al.*, “Highly scalable nonvolatile resistive memory using simple binary oxide driven by asymmetric unipolar voltage pulses,” in *IEDM Technical Digest. IEEE International Electron Devices Meeting, 2004.*, pp. 587–590, IEEE, 2004.

[160] W. Kim, S. I. Park, Z. Zhang, Y. Yang-Liauw, D. Sekar, H.-S. P. Wong, and S. S. Wong, “Forming-free nitrogen-doped alo x rram with sub-μa programming current,” in *2011 Symposium on VLSI Technology-Digest of Technical Papers*, pp. 22–23, IEEE, 2011.

[161] A. Chen, S. Haddad, Y.-C. Wu, T.-N. Fang, Z. Lan, S. Avanzino, S. Pangrle, M. Buynoski, M. Rathor, W. Cai, *et al.*, “Non-volatile resistive switching for advanced memory applications,” in *IEEE InternationalElectron Devices Meeting, 2005. IEDM Technical Digest.*, pp. 746–749, IEEE, 2005.

[162] H. Lee, P. Chen, T. Wu, Y. Chen, C. Wang, P. Tzeng, C. Lin, F. Chen, C. Lien, and M.-J. Tsai, “Low power and high speed bipolar switching with a thin reactive ti buffer layer in robust hfo2 based rram,” in *2008 IEEE International Electron Devices Meeting*, pp. 1–4, IEEE, 2008.

[163] S. Seo, M. Lee, D. Seo, E. Jeoung, D.-S. Suh, Y. Joung, I. Yoo, I. Hwang, S. Kim, I. Byun, *et al.*, “Reproducible resistance switching in polycrystalline nio films,” *Applied Physics Letters*, vol. 85, no. 23, pp. 5655–5657, 2004.

[164] B. Choi, D. Jeong, S. Kim, C. Rohde, S. Choi, J. Oh, H. Kim, C. Hwang, K. Szot, R. Waser, *et al.*, “Resistive switching mechanism of tio 2 thin films grown by atomic-layer deposition,” *Journal of Applied Physics*, vol. 98, no. 3, p. 033715, 2005.

[165] C.-Y. Lin, C.-Y. Wu, C.-Y. Wu, T.-Y. Tseng, and C. Hu, “Modified resistive switching behavior of zr o 2 memory films based on the interface layer formed by using ti top electrode,” *Journal of Applied Physics*, vol. 102, no. 9, p. 094101, 2007.

[166] N. Xu, L. Liu, X. Sun, X. Liu, D. Han, Y. Wang, R. Han, J. Kang, and B. Yu, “Characteristics and mechanism of conduction/set process in ti n/ zn o/ pt resistance switching random-access memories,” *Applied Physics Letters*, vol. 92, no. 23, p. 232112, 2008.

[167] Z. Wei, Y. Kanzawa, K. Arita, Y. Katoh, K. Kawai, S. Muraoka, S. Mitani, S. Fujii, K. Katayama, M. Iijima, *et al.*, “Highly reliable taox reram and direct evidence of redox reaction mechanism,” in *2008 IEEE International Electron Devices Meeting*, pp. 1–4, IEEE, 2008.

[168] K. Aratani, K. Ohba, T. Mizuguchi, S. Yasuda, T. Shiimoto, T. Tsushima, T. Sone, K. Endo, A. Kouchiyama, S. Sasaki, *et al.*, "A novel resistance memory with high scalability and nanosecond switching," in *2007 IEEE International Electron Devices Meeting*, pp. 783–786, IEEE, 2007.

[169] H. S. Yoon, I.-G. Baek, J. Zhao, H. Sim, M. Y. Park, H. Lee, G.-H. Oh, J. C. Shin, I.-S. Yeo, and U.-I. Chung, "Vertical cross-point resistance change memory for ultra-high density non-volatile memory applications," in *2009 Symposium on VLSI Technology*, pp. 26–27, IEEE, 2009.

[170] B. Govoreanu, G. S. Kar, Y. Chen, V. Paraschiv, S. Kubicek, A. Fantini, I. Radu, L. Goux, S. Clima, R. Degraeve, *et al.*, "10× 10nm 2 hf/hfo x crossbar resistive ram with excellent performance, reliability and low-energy operation," in *2011 International Electron Devices Meeting*, pp. 31–6, IEEE, 2011.

[171] S. Sills, S. Yasuda, J. Strand, A. Calderoni, K. Aratani, A. Johnson, and N. Ramaswamy, "A copper reram cell for storage class memory applications," in *2014 Symposium on VLSI Technology (VLSI-Technology): Digest of Technical Papers*, pp. 1–2, IEEE, 2014.

[172] X. Yuan, S. Kim, J. Juyon, M. D'Urbino, T. Bullmann, Y. Chen, A. Stettler, A. Hierlemann, and U. Frey, "A microelectrode array with 8,640 electrodes enabling simultaneous full-frame readout at 6.5 kfps and 112-channel switch-matrix readout at 20 ks/s," in *2016 IEEE Symposium on VLSI Circuits (VLSI-Circuits)*, pp. 1–2, IEEE, 2016.

[173] E. J. Yoo, M. Lyu, J.-H. Yun, C. J. Kang, Y. J. Choi, and L. Wang, "Resistive switching behavior in organic-inorganic hybrid $CH_3NH_3PbI_{3-x}Cl_x$ perovskite for resistive random access memory devices," *Advanced Materials*, vol. 27, no. 40, pp. 6170–6175, 2015.

[174] S. Ren, G. Zhu, J. Xie, J. Bu, H. Qin, and J. Hu, "Resistive switching and electrical control of ferromagnetism in a $Ag/HfO_2/Nb$: $SrTiO_3/Ag$ resistive random access memory (rram) device at room temperature," *Journal of Physics: Condensed Matter*, vol. 28, no. 5, p. 056001, 2016.

[175] Y. Liu, F. Li, Z. Chen, T. Guo, C. Wu, and T. W. Kim, "Resistive switching memory based on organic/inorganic hybrid perovskite materials," *Vacuum*, vol. 130, pp. 109–112, 2016.

[176] J. Jang, F. Pan, K. Braam, and V. Subramanian, "Resistance switching characteristics of solid electrolyte chalcogenide Ag_2Se nanoparticles for flexible nonvolatile memory applications," *Advanced Materials*, vol. 24, no. 26, pp. 3573–3576, 2012.

[177] S. D. Ha and S. Ramanathan, "Adaptive oxide electronics: A review," *Journal of Applied Physics*, vol. 110, no. 7, p. 14, 2011.

[178] C. Kim, Y. Jang, H. Hwang, Z. Sun, H. Moon, and J. Cho, "Observation of bistable resistance memory switching in cuo thin films," *Applied Physics Letters*, vol. 94, no. 10, p. 102107, 2009.

[179] J. S. Kwak, Y. H. Do, Y. C. Bae, H. Im, and J. P. Hong, "Reproducible unipolar resistive switching behaviors in the metal-deficient coox thin film," *Thin Solid Films*, vol. 518, no. 22, pp. 6437–6440, 2010.

[180] J.-Y. Lee, Y.-J. Baek, Q. Hu, Y. Jin Choi, C. Jung Kang, H. H. Lee, H.-M. Kim, K.-B. Kim, and T.-S. Yoon, "Multimode threshold and bipolar resistive switching in bi-layered pt-fe2o3 core-shell and fe2o3 nanoparticle assembly," *Applied Physics Letters*, vol. 102, no. 12, p. 122111, 2013.

[181] X. Cao, X. Li, X. Gao, W. Yu, X. Liu, Y. Zhang, L. Chen, and X. Cheng, "Forming-free colossal resistive switching effect in rare-earth-oxide gd 2 o 3 films for memristor applications," *Journal of Applied Physics*, vol. 106, no. 7, p. 073723, 2009.

[182] L. Goux, P. Czarnecki, Y. Y. Chen, L. Pantisano, X. Wang, R. Degraeve, B. Govoreanu, M. Jurczak, D. Wouters, and L. Altimime, "Evidences of oxygen-mediated resistive-switching mechanism in tin/hfo$_2$/pt cells," *Applied Physics Letters*, vol. 97, no. 24, p. 243509, 2010.

[183] M. K. Yang, J.-W. Park, T. K. Ko, and J.-K. Lee, "Bipolar resistive switching behavior in ti/mno 2/pt structure for nonvolatile memory devices," *Applied Physics Letters*, vol. 95, no. 4, p. 042105, 2009.

[184] S. Kim, X. Liu, J. Park, S. Jung, W. Lee, J. Woo, J. Shin, G. Choi, C. Cho, S. Park, *et al.*, "Ultrathin (¡ 10nm) nb 2 o 5/nbo 2 hybrid memory with both memory and selector characteristics for high density 3d vertically stackable rram applications," in *2012 Symposium on VLSI Technology (VLSIT)*, pp. 155–156, IEEE, 2012.

[185] L. Goux, J. Lisoni, M. Jurczak, D. Wouters, L. Courtade, and C. Muller, "Coexistence of the bipolar and unipolar resistive-switching modes in nio cells made by thermal oxidation of ni layers," *Journal of Applied Physics*, vol. 107, no. 2, p. 024512, 2010.

[186] P. Fermo and G. Padeletti, "The use of nano-particles to produce iridescent metallic effects on ancient ceramic objects," *Journal of Nanoscience and Nanotechnology*, vol. 12, no. 11, pp. 8764–8769, 2012.

[187] W.-Y. Chang, Y.-C. Lai, T.-B. Wu, S.-F. Wang, F. Chen, and M.-J. Tsai, "Unipolar resistive switching characteristics of zno thin films for nonvolatile memory applications," *Applied Physics Letters*, vol. 92, no. 2, p. 022110, 2008.

[188] C. Chen, Y. Yang, F. Zeng, and F. Pan, "Bipolar resistive switching in cu/aln/pt nonvolatile memory device," *Applied Physics Letters*, vol. 97, no. 8, p. 083502, 2010.

[189] F. M. Puglisi, L. Larcher, C. Pan, N. Xiao, Y. Shi, F. Hui, and M. Lanza, "2d h-bn based rram devices," in *2016 IEEE International Electron Devices Meeting (IEDM)*, pp. 34–8, IEEE, 2016.

[190] H.-D. Kim, M. J. Yun, and T. G. Kim, "Self-selection bipolar resistive switching phenomena observed in nbon/nbn bilayer for cross-bar array memory applications," *Applied Physics Letters*, vol. 105, no. 21, p. 213510, 2014.

[191] H.-D. Kim, H.-M. An, and T. G. Kim, "Ultrafast resistive-switching phenomena observed in nin-based reram cells," *IEEE Transactions on Electron Devices*, vol. 59, no. 9, pp. 2302–2307, 2012.

[192] S. M. Hong, H.-D. Kim, H.-M. An, and T. G. Kim, "Effect of work function difference between top and bottom electrodes on the resistive switching properties of sin films," *IEEE Electron Device Letters*, vol. 34, no. 9, pp. 1181–1183, 2013.

[193] K. Szot, R. Dittmann, W. Speier, and R. Waser, "Nanoscale resistive switching in srtio3 thin films," *physica status solidi (RRL)–Rapid Research Letters*, vol. 1, no. 2, pp. R86–R88, 2007.

[194] C.-Y. Liu, P.-H. Wu, A. Wang, W.-Y. Jang, J.-C. Young, K.-Y. Chiu, and T.-Y. Tseng, "Bistable resistive switching of a sputter-deposited cr-doped srzro/sub 3/memory film," *IEEE Electron Device Letters*, vol. 26, no. 6, pp. 351–353, 2005.

[195] C. Collier, E. Wong, M. Belohradsky, F. Raymo, J. Stoddart, P. Kuekes, R. Williams, and J. Heath, "Electronically configurable molecular-based logic gates," *Science*, vol. 285, no. 5426, pp. 391–394, 1999.

[196] A. Elsharkawi, "Switching and memory phenomena in anthracene thin films," *Journal of Physics and Chemistry of Solids*, vol. 38, no. 1, pp. 95–96, 1977.

[197] A. Szymanski, D. Larson, and M. Labes, "A temperature-independent conducting state in tetracene thin film," *Applied Physics Letters*, vol. 14, no. 3, pp. 88–90, 1969.

[198] F. Moresco, G. Meyer, K.-H. Rieder, H. Tang, A. Gourdon, and C. Joachim, "Conformational changes of single molecules induced by scanning tunneling microscopy manipulation: A route to molecular switching," *Physical Review Letters*, vol. 86, no. 4, p. 672, 2001.

[199] J. Cornil, Y. Karzazi, and J. Bredas, "Negative differential resistance in phenylene ethynylene oligomers," *Journal of the American Chemical Society*, vol. 124, no. 14, pp. 3516–3517, 2002.

[200] J. Van Den Hurk, I. Valov, and R. Waser, "Preparation and characterization of gesx thin-films for resistive switching memories," *Thin Solid Films*, vol. 527, pp. 299–302, 2013.

[201] S. Rahaman, S. Maikap, H.-C. Chiu, C.-H. Lin, T.-Y. Wu, Y.-S. Chen, P.-J. Tzeng, F. Chen, M.-J. Kao, and M.-J. Tsai, "Bipolar resistive switching memory using cu metallic filament in ge0. 4se0. 6 solid electrolyte," *Electrochemical and Solid-State Letters*, vol. 13, no. 5, p. H159, 2010.

[202] X. Liu, M. T. Mayer, and D. Wang, "Negative differential resistance and resistive switching behaviors in cu 2 s nanowire devices," *Applied Physics Letters*, vol. 96, no. 22, p. 223103, 2010.

[203] S. Yu, *Resistive Switching Memory for Non-volatile Storage and Neuromorphic Computing*. Ph.D. Dissertation, Stanford University, Stanford, CA, 2013.

[204] M. N. Kozicki and H. J. Barnaby, "Conductive bridging random access memory—materials, devices and applications," *Semiconductor Science and Technology*, vol. 31, no. 11, p. 113001, 2016.

[205] I. Valov, R. Waser, J. R. Jameson, and M. N. Kozicki, "Electrochemical metallization memories—fundamentals, applications, prospects," *Nanotechnology*, vol. 22, no. 25, p. 254003, 2011.

[206] L. Goux and I. Valov, "Electrochemical processes and device improvement in conductive bridge ram cells," *Physica Status Solidi (a)*, vol. 213, no. 2, pp. 274–288, 2016.

[207] S. Yu, X. Guan, and H.-S. P. Wong, "Conduction mechanism of tin/hfox/pt resistive switching memory: A trap-assisted-tunneling model," *Applied Physics Letters*, vol. 99, no. 6, p. 063507, 2011.

[208] F. Zahoor, T. Z. Azni Zulkifli, and F. A. Khanday, "Resistive random access memory (rram): an overview of materials, switching mechanism, performance, multilevel cell (mlc) storage, modeling, and applications," *Nanoscale Research Letters*, vol. 15, no. 1, pp. 1–26, 2020.

[209] Y. Chen, "Reram: History, status, and future," *IEEE Transactions on Electron Devices*, vol. 67, no. 4, pp. 1420–1433, 2020.

[210] "Semiconductor industry market." `https://www.semi.org/en/semiconductor-industry-2015-2025`. Accessed: 11-17-2022.

[211] H. Akinaga and H. Shima, "Resistive random access memory (reram) based on metal oxides," *Proceedings of the IEEE*, vol. 98, no. 12, pp. 2237–2251, 2010.

[212] N. Xu, L. Liu, X. Sun, C. Chen, Y. Wang, D. Han, X. Liu, R. Han, J. Kang, and B. Yu, "Bipolar switching behavior in tin/zno/pt resistive nonvolatile memory with fast switching and long retention," *Semiconductor Science and Technology*, vol. 23, no. 7, p. 075019, 2008.

[213] K.-L. Lin, T.-H. Hou, J. Shieh, J.-H. Lin, C.-T. Chou, and Y.-J. Lee, "Electrode dependence of filament formation in HfO_2 resistive-switching memory," *Journal of Applied Physics*, vol. 109, no. 8, p. 084104, 2011.

[214] B. Jain, C.-s. Huang, D. Misra, K. Tapily, R. D. Clark, S. Consiglio, C. S. Wajda, and G. J. Leusink, "Multilevel resistive switching in hf-based rram," *ECS Transactions*, vol. 89, no. 3, p. 39, 2019.

[215] K. M. Kim, B. J. Choi, Y. C. Shin, S. Choi, and C. S. Hwang, "Anode-interface localized filamentary mechanism in resistive switching of TiO_2 thin films," *Applied Physics Letters*, vol. 91, no. 1, p. 012907, 2007.

[216] Y. Wu, B. Lee, and H.-S. P. Wong, "Al_2O_3-based rram using atomic layer deposition (ald) with 1-μa reset current," *IEEE Electron Device Letters*, vol. 31, no. 12, pp. 1449–1451, 2010.

[217] M. Bartic, M. Ogita, M. Isai, C.-L. Baban, and H. Suzuki, "Oxygen sensing properties at high temperatures of β-Ga_2O_3 thin films deposited by the chemical solution deposition method," *Journal of Applied Physics*, vol. 102, no. 2, p. 023709, 2007.

[218] M. Ogita, K. Higo, Y. Nakanishi, and Y. Hatanaka, "Ga_2O_3 thin film for oxygen sensor at high temperature," *Applied Surface Science*, vol. 175, pp. 721–725, 2001.

[219] H. Tippins, "Optical absorption and photoconductivity in the band edge of $\beta - Ga_2O_3$," *Physical Review*, vol. 140, no. 1A, p. A316, 1965.

[220] M. Orita, H. Ohta, M. Hirano, and H. Hosono, "Deep-ultraviolet transparent conductive $\beta - Ga_2O_3$ thin films," *Applied Physics Letters*, vol. 77, no. 25, pp. 4166–4168, 2000.

[221] J.-B. Yang, T.-C. Chang, J.-J. Huang, S.-C. Chen, P.-C. Yang, Y.-T. Chen, H.-C. Tseng, S. M. Sze, A.-K. Chu, and M.-J. Tsai, "Resistive switching characteristics of gallium oxide for nonvolatile memory application," *Thin Solid Films*, vol. 529, pp. 200–204, 2013.

[222] X. Gao, Y. Xia, J. Ji, H. Xu, Y. Su, H. Li, C. Yang, H. Guo, J. Yin, and Z. Liu, "Effect of top electrode materials on bipolar resistive switching behavior of gallium oxide films," *Applied Physics Letters*, vol. 97, no. 19, p. 193501, 2010.

[223] D.-Y. Lee and T.-Y. Tseng, "Forming-free resistive switching behaviors in cr-embedded Ga_2O_3 thin film memories," *Journal of Applied Physics*, vol. 110, no. 11, p. 114117, 2011.

[224] C.-W. Hsu and L.-J. Chou, "Bipolar resistive switching of single gold-in-Ga_2O_3 nanowire," *Nano Letters*, vol. 12, no. 8, pp. 4247–4253, 2012.

[225] X. Shen, L. Zhang, L. Liu, Y. An, Z. Gao, and P. Guo, “Bipolar resistive switching of Pt/Ga_2O_3/SiC/Pt thin film with ultrahigh OFF/ON resistance ratios,” *Nanotechnology*, vol. 31, no. 22, p. 225206, 2020.

[226] M. Higashiwaki, K. Sasaki, A. Kuramata, T. Masui, and S. Yamakoshi, “Gallium oxide (Ga_2O_3) metal-semiconductor field-effect transistors on single-crystal $\beta-$ Ga_2O_3 (010) substrates,” *Applied Physics Letters*, vol. 100, no. 1, p. 013504, 2012.

[227] N. Ma, N. Tanen, A. Verma, Z. Guo, T. Luo, H. Xing, and D. Jena, “Intrinsic electron mobility limits in $\beta-Ga_2O_3$,” *Applied Physics Letters*, vol. 109, no. 21, p. 212101, 2016.

[228] A. Paskaleva, D. Spassov, and P. Terziyska, “Electric, dielectric and optical properties of Ga_2O_3 grown by metal organic chemical vapour deposition,” in *Journal of Physics: Conference Series*, vol. 794, p. 012017, IOP Publishing, 2017.

[229] A. Afzal, “$\beta - Ga_2O_3$ nanowires and thin films for metal oxide semiconductor gas sensors: Sensing mechanisms and performance enhancement strategies,” *Journal of Materiomics*, vol. 5, no. 4, pp. 542–557, 2019.

[230] D. Guo, Q. Guo, Z. Chen, Z. Wu, P. Li, and W. Tang, “Review of Ga_2O_3-based optoelectronic devices,” *Materials Today Physics*, vol. 11, p. 100157, 2019.

[231] M. Boukadhaba, A. Fouzri, V. Sallet, S. Hassani, G. Amiri, A. Lusson, and M. Oumezzine, “High-temperature annealing effect of $\alpha - Al_2O_3$ (0001) substrates with nominal 0.25○ miscut toward the a-plane (1120) on zno films grown by mocvd,” *Applied Physics A*, vol. 120, no. 3, pp. 991–1000, 2015.

[232] A. Prakash and H. Hwang, “Multilevel cell storage and resistance variability in resistive random access memory,” *Physical Sciences Reviews*, vol. 1, no. 6, 2016.

[233] T. J. Yen, A. Chin, and V. Gritsenko, “High performance all nonmetal sinx resistive random access memory with strong process dependence,” *Scientific Reports*, vol. 10, no. 1, pp. 1–9, 2020.

[234] C. Di Valentin, G. Palma, and G. Pacchioni, “Ab initio study of transition levels for intrinsic defects in silicon nitride,” *The Journal of Physical Chemistry C*, vol. 115, no. 2, pp. 561–569, 2011.

[235] N. Tamanna, S. H. Misha, A. Prakash, D. Lee, J. Woo, E. Cha, B. Attarimashalkoubeh, J. Song, S. Lee, K. Moon, *et al.*, “Non-linear iv characteristics of tioy film by optimizing thickness and trap density for selector-less reram,” *ECS Solid State Letters*, vol. 3, no. 10, p. P117, 2014.

[236] R. Waser and M. Aono, “Nanoscience and technology: a collection of reviews from nature journals,” *World Science*, pp. 158–165, 2010.

[237] K.-M. Persson, M. S. Ram, O.-P. Kilpi, M. Borg, and L.-E. Wernersson, “Cross-point arrays with low-power ito-hfo2 resistive memory cells integrated on vertical iii-v nanowires,” *Advanced Electronic Materials*, vol. 6, no. 6, p. 2000154, 2020.

[238] M.-H. Kim, S. Kim, S. Bang, T.-H. Kim, D. K. Lee, S. Cho, and B.-G. Park, “Uniformity improvement of sin x-based resistive switching memory by suppressed internal overshoot current,” *IEEE Transactions on Nanotechnology*, vol. 17, no. 4, pp. 824–828, 2018.

[239] Y. Y. Chen, M. Komura, R. Degraeve, B. Govoreanu, L. Goux, A. Fantini, N. Raghavan, S. Clima, L. Zhang, A. Belmonte, *et al.*, “Improvement of data retention in hfo 2/hf 1t1r rram cell under low operating current,” in *2013 IEEE International Electron Devices Meeting*, pp. 10–1, IEEE, 2013.

[240] S. Gaba, F. Cai, J. Zhou, and W. D. Lu, “Ultralow sub-1-na operating current resistive memory with intrinsic non-linear characteristics,” *IEEE Electron Device Letters*, vol. 35, no. 12, pp. 1239–1241, 2014.

[241] H. Jiang, X. Y. Li, R. Chen, X. L. Shao, J. H. Yoon, X. Hu, C. S. Hwang, and J. Zhao, “Bias-polarity-dependent resistance switching in w/sio2/pt and w/sio2/si/pt structures,” *Scientific Reports*, vol. 6, no. 1, pp. 1–11, 2016.

[242] Y. Li, L. Yin, Z. Wu, X. Li, X. Song, X. Gao, and L. Fu, “Improved resistive switching uniformity of sio 2 electrolyte-based resistive random access memory device with cu oxidizable electrode,” *IEEE Electron Device Letters*, vol. 40, no. 10, pp. 1599–1601, 2019.

[243] J.-W. Huang, R. Zhang, T.-C. Chang, T.-M. Tsai, K.-C. Chang, J. Lou, T.-F. Young, J.-H. Chen, H.-L. Chen, Y.-C. Pan, *et al.*, “The effect of high/low permittivity in bilayer hfo2/bn resistance random access memory,” *Applied Physics Letters*, vol. 102, no. 20, p. 203507, 2013.

[244] N. Vasileiadis, P. Karakolis, P. Mandylas, V. Ioannou-Sougleridis, P. Normand, M. Perego, P. Komninou, V. Ntinas, I.-A. Fyrigos, I. Karafyllidis, *et al.*, “Understanding the role of defects in silicon nitride-based resistive switching memories through oxygen doping,” *IEEE Transactions on Nanotechnology*, vol. 20, pp. 356–364, 2021.

[245] Y. Yang, P. Gao, S. Gaba, T. Chang, X. Pan, and W. Lu, “Observation of conducting filament growth in nanoscale resistive memories,” *Nature Communications*, vol. 3, no. 1, pp. 1–8, 2012.

[246] P. Bousoulas, S. Stathopoulos, D. Tsialoukis, and D. Tsoukalas, “Low-power and highly uniform 3-b multilevel switching in forming free tio 2–x-based rram with embedded pt nanocrystals,” *IEEE Electron Device Letters*, vol. 37, no. 7, pp. 874–877, 2016.

[247] Y. Huang, Z. Shen, Y. Wu, X. Wang, S. Zhang, X. Shi, and H. Zeng, "Amorphous zno based resistive random access memory," *RSC Advances*, vol. 6, no. 22, pp. 17867–17872, 2016.

[248] G. Gonzalez-Cordero, F. Jimenez-Molinos, J. B. Roldán, M. B. González, and F. Campabadal, "In-depth study of the physics behind resistive switching in tin/ti/hfo2/w structures," *Journal of Vacuum Science and Technology B, Nanotechnology and Microelectronics: Materials, Processing, Measurement, and Phenomena*, vol. 35, no. 1, p. 01A110, 2017.

[249] J. Guo, H. Gao, P. Jiang, M. Yang, X. Jiang, Z. Zhang, X. Ma, and Y. Yang, "Influence of nitrogen adsorption of doped ta on characteristics of sinx-based resistive random access memory," *Physica Status Solidi (a)*, vol. 216, no. 22, p. 1900540, 2019.

[250] H. Jeon, J. Park, W. Jang, H. Kim, K. Lee, C. Shin, J. Lee, and H. Jeon, "Resistive switching behaviors of ti nano-layer embedded taox-based devices," *Current Applied Physics*, vol. 17, no. 2, pp. 230–234, 2017.

[251] Y.-H. Ra, S. Kang, and C.-R. Lee, "Ultraviolet light-emitting diode using nonpolar algan core–shell nanowire heterostructures," *Advanced Optical Materials*, vol. 6, no. 14, p. 1701391, 2018.

[252] S. Zhao, J. Lu, X. Hai, and X. Yin, "Algan nanowires for ultraviolet light-emitting: recent progress, challenges, and prospects," *Micromachines*, vol. 11, no. 2, p. 125, 2020.

[253] L. Mi, H. Wang, Y. Zhang, X. Yao, Y. Chang, G. Li, G. Li, and Y. Jiang, "High performance visible–near-infrared pbs-quantum-dots/indium schottky diodes for photodetectors," *Nanotechnology*, vol. 28, no. 5, p. 055202, 2016.

[254] X. Yu, K. Chang, A. Dong, Z. Gan, K. Jiang, Y. Ling, Y. Niu, D. Zheng, X. Dong, R. Wang, *et al.*, "High-performance resistive switching memory with embedded molybdenum disulfide quantum dots," *Applied Physics Letters*, vol. 118, no. 17, p. 172104, 2021.